ELECTRON ENERGY LOSS SPECTROSCOPY OF SN-DOPED INDIUM OXIDE NANOSTRUCTURES

ELECTRON ENERGY LOSS SPECTROSCOPY OF SN-DOPED INDIUM OXIDE NANOSTRUCTURES

By
VIKTOR KAPETANOVIC, B.ENG.

A Thesis Submitted to the School of Graduate Studies in Partial Fulfilment of the Requirements for the Degree Master of Applied Science

McMaster University MASTER OF APPLIED SCIENCE (2018) Hamilton, Ontario (Materials Science and Engineering)

TITLE: Electron Energy Loss Spectroscopy of Sn-Doped Indium Oxide Nanostructures

AUTHOR: Viktor Kapetanovic, B.Eng. (McMaster University)

SUPERVISOR: Professor G.A. Botton

NUMBER OF PAGES: xv, 82

To my parents, Jadranka and Miloš,
and my brother, David.

Work hard, but be smart about it

Acknowledgements

I want to first acknowledge the invaluable role that my supervisor, Gianluigi Botton, has had during my time here. You've provided me with the freedom to pursue (and to struggle with) a field rich with interesting science. Thank you for putting your faith in my abilities and for the opportunities you've enabled.

To my parents, I've appreciated the regular care packages and the effort into making sure my needs are met. All I can say is *hvala*, with as much emphasis as I can.

Additional appreciation goes out to Doris Stefanovic and Shahram Ghanad-Tavakoli at the CEDT, and all the staff at the CCEM for the training and helpful environment, enabling this research.

I've had the privilege of being part of an incredibly diverse, friendly, and determined research group. I thank you, Isobel Bicket, my amazing plasmonics guru, whose dedication and willingness to help has benefited the group so much that I would need a second thesis to express it. At the time of writing I already miss our microscope (and laser!) sessions. To Alexandre "Bro"-felski, thank you for your genuine love of teaching and ability to empower those around you. I'm so grateful to have wonderful memories of my time here with Fredy Carranco, Eric Daigle, Reza Safari, Edson Bellido, Amin Hashemi, Maureen Lagos, Shaobo Cheng, Shayan Mousavi Masouleh, and Sam Norris. Special thanks to the KG group that we shared JHE A406 with, visiting students Ramon Manzorro and Catalina Coll Benejam, and the era of Moiré Pattern FCC. A final thank you to Chiara for keeping me balanced.

Lay Abstract

The push towards smaller, faster electronic devices and sensing equipment has accelerated research into manipulating oscillating groups of electrons, or plasmons. So far, the building blocks of these next-generation systems use metals such as gold and silver; however, new materials must be explored for them to be commercially viable. Thin continuous films of transparent conductive oxides (TCOs) such as Sn-doped Indium Oxide (ITO) are already widely used in conventional silicon-based technologies, and in this work ITO nanostructures are fabricated to visualize their plasmonic response, in the hopes that they could be tailored towards plasmonic devices. The relationships between how these plasmons evolve with varying dimensions and the application of heat are explored using electron microscopy.

Abstract

This thesis presents the fabrication of Sn-doped In_2O_3 nanostructures on a 50 nm thick SiN membrane and their characterization using monochromated electron energy loss spectroscopy (EELS). Rapidly annealed triangular structures of varying thicknesses (71 nm and 32 nm) and lengths (between 400 nm and 1200 nm) unveil a structural crystallization, as well as a blue-shift and narrowing of surface (first and second order modes) and bulk plasmon peaks as the free carrier concentration increases. Bulk peak positions shift from 515$\pm$39 meV to 628$\pm$36 meV for 71 nm thick triangles. The second order surface plasmon modes exhibit a greater blue-shift after annealing ($\Delta E = 93$ meV) than the first order modes ($\Delta E = 36$ meV), consistent with the trend found in boundary element method (BEM) simulations using ellipsometry data. The Richardson-Lucy (RL) deconvolution algorithm is employed to improve the effective energy resolution and reveal these surface plasmons as well as a substrate phonon at 100$\pm$19 meV. Low-loss EELS spectra for 32 nm thick triangles potentially show a blue-shifting bulk plasmon from 751$\pm$42 meV to 912$\pm$42 meV with decreasing triangle size. STEM imaging of the triangle structure cross-sections may show a clustering of oxygen vacancies and indium atoms that could be responsible for this blue-shift. Core-loss EELS spectra between 380-550 eV using the oxygen K-edge signal provide evidence of a change in the bonding across the ITO/SiN interface, although its effect on the electrical properties requires further investigation.

Contents

1 Introduction **1**

2 Background **3**

2.1 The Field of Plasmonics 3

2.1.1 Historical Overview 3

2.1.2 Plasmon Theory 4

2.1.3 Plasmonic Materials 9

2.2 Sn-doped Indium Oxide 14

2.2.1 Crystal Structure and Growth 14

2.2.2 Defects and Carrier Transport 18

2.2.3 Energy Band Structure 23

2.3 Characterization with Electron Microscopy 26

2.3.1 Imaging 26

2.3.2 The Transmission Electron Microscope 28

2.3.3 The Low-Loss Region 30

2.3.4 The High-Loss Region 34

2.3.5 Energy Resolution 35

3 Experimental Methods and Simulations **40**

3.1 Fabrication Overview 40

3.2 EEL Simulations 44

3.3 Low-Loss EELS 45

3.4 Preparation of Cross-Section 46

3.5 Core-Loss EELS 47

4 Results and Discussion **49**

4.1 Fabricated Structures 49

4.2 The Plasmonic Response of ITO 53

4.2.1 Visualizing LSPs 53

4.2.2 Effect of Annealing 58
4.2.3 Effect of Thickness 62

Appendix **69**
A.3 Richardson-Lucy Deconvolution 69
A.4 RTA Procedure 70
A.5 Additional Images 71
A.6 X-Ray Diffraction of ITO Film 72

List of Figures

2.1 Response of electrons to an external electric field 4
2.2 Dielectric function 6
2.3 Dispersion of plasmons 7
2.4 Dispersion of coupled plasmons 9
2.5 E-k and E-N diagrams for metals and semiconductors 10
2.6 Dielectric functions of alternative plasmonic materials 11
2.7 Suitability of materials for plasmonics 13
2.8 ITO unit cell 14
2.9 Stages of thin film growth 15
2.10 RF sputtering schematic 16
2.11 Volmer-Weber nucleation mechanism 17
2.12 TEM micrographs and diffraction patterns of ITO 17
2.13 Amorphous to crystalline transformation 18
2.14 Doping mechanisms in ITO 19
2.15 Oxidation effect in EELS and XPS spectra 20
2.16 Thickness-dependent carrier transport 22
2.17 Energy band diagrams of *a*-ITO and *c*-ITO 24
2.18 Possible energy band diagram for In_2O_3 25
2.19 Comparison of bulk and surface defects in In_2O_3 26
2.20 Ray diagram for thin lens 27
2.21 Schematics for SEM and FIB instrumentation 28
2.22 Schematics for TEM and STEM configurations 29
2.23 Obtaining an EELS spectrum 30
2.24 STEM images of a plasmonic Ag triangle 31
2.25 Surface and bulk scattering in EELS 33
2.26 Example of core-loss spectra for ITO 36
2.27 The monochromator 37
2.28 Beam profile over the spectrometer CCD 37

2.29 Applying the Richardson-Lucy algorithm to EELS spectra 38

3.1 Preparing for electron beam lithography 41
3.2 Sputtering machine 42
3.3 Nanostructure process flow 43
3.4 Schematics for conductivity and ellipsometry testing 44
3.5 Generated mesh for nanostructures in MNPBEM toolbox 45
3.6 FIB preparation of 71 nm thick film 47
3.7 FIB preparation of 71 nm thick triangles 48

4.1 Imaging and diffraction of ITO nanostructures 50
4.2 Images of ITO/SiN/Si cross-sections 51
4.3 Dielectric functions obtained by ellipsometry 54
4.4 EEL simulation for a 71 nm thick triangle 55
4.5 Low-loss EELS mapping of surface and bulk plasmons 56
4.6 EEL simulation comparing *a*-ITO and *c*-ITO 58
4.7 HAADF images of 71 nm thick *a*-ITO and *c*-ITO triangles 59
4.8 Low-loss spectra probed over *a*-ITO and *c*-ITO 59
4.9 Low-loss spectra probed outside *a*-ITO and *c*-ITO 61
4.10 Experimental dispersion of surface plasmon modes 61
4.11 Low-loss spectra of 32 nm thick triangles 64
4.12 Core-loss spectra for 32 nm thick triangle cross-section 65
4.13 Core-loss spectra for 71 nm thick triangle cross-section 66
4.14 Annealing parameters 70
4.15 HAADF images of 32 nm thick triangles 71
4.16 SEM images of fabricated structures 71
4.17 XRD pattern for a thin film 72

List of Tables

3.1 Ellipsometry fitting parameters for SiN 44

4.1 Ellipsometry fitting parameters for ITO 53

List of Abbreviations

ADF Annular Dark Field.

BF Bright Field.

BFP Back Focal Plane.

BP Bulk Plasmon.

CB Conduction Band.

DOS Density Of States.

EBL Electron Beam Lithography.

FIB Focused Ion Beam.

FWHM Full Width Half Maximum.

HAADF High Angle Annular Dark Field.

ITO Indium Tin Oxide.

LSP Localized Surface Plasmon.

MFP Mean Free Path.

MNPBEM Metal Nanoparticle Boundary Element Method.

RL Richardson Lucy.

RTA Rapid Thermal Anneal.

SEM Scanning Electron Microscope.

SI Spectrum Image.

SNR Signal to Noise Ratio.

SP Surface Plasmon.

SPP Surface Plasmon Polariton.

STEM Scanning Transmission Electron Microscope.

TCO Transparent Conductive Oxide.

TEM Transmission Electron Microscope.

VASE Variable Angle Spectroscopy Ellipsometer.

VB Valence Band.

ZLP Zero Loss Peak.

Declaration of Academic Achievement

I hereby declare to be the sole author of this document. The research work presented in this thesis was mostly completed by myself, with the contribution of the following people listed below.

- Low-loss EELS spectra for sample T8 were acquired by Sorin Lazar at the FEI Company in The Netherlands.
- Low-loss EELS spectra for samples T5 and T6 were carried out with the help of Isobel Bicket.
- Diffraction imaging for sample T1 was carried out with the help of Carmen Andrei of the CCEM.
- FIB sample preparation was carried out by Travis Casagrande of the CCEM.
- Core-loss EELS spectra of cross-sections were carried out with the help of Isobel Bicket, Edson Bellido, and Shaobo Cheng.
- X-Ray Diffraction spectra and analysis of an ITO thin film were carried out by Vicky Jarvis of the MAX Diffraction Facility

Chapter 1

Introduction

The limitations in decreasing transistor size are motivating the research into alternate methods of information processing for the next generations of devices. Silicon photonics has been an emerging field that provides high-bandwidth, light-speed data transfer and modulation that electronic circuits are incapable of, however the scaling down of such components is difficult due to the diffraction limit of light. This is especially true for devices operating at infrared (IR) wavelengths. Thus, the field of plasmonics has developed to bridge the gap between photonics and electronics by offering sub-diffraction confinement with comparable speeds to photonics. Light can couple to electron oscillations at metal-dielectric interfaces and, together, propagate along the interface as a surface plasmon polariton (SPP), or when confined to dimensions smaller than λ, a localized plasmon polariton (LSP). Such confinements create strong electromagnetic fields in localized areas (at the nanometer level). The potential for integrated circuitry that takes advantage of these interactions can lead to devices with reduced power consumption, improved form factor, sensing, and detection. Nanoscale tweezers, waveguides, switches, lasers, biological rulers, and photocatalysts are some types of applications that can be enabled or improved with plasmonics.

With the vast literature on metal plasmonics, efforts into understanding and applying semiconductors in this field are growing. This push comes from the knowledge that SPP and LSP lifetimes are too short in metals to be useful for practical devices. ITO (Sn-doped In_2O_3), a material from the class of transparent conductive oxides (TCOs), is a candidate to replace, or to be integrated with, metals. Its high conductivity with optical transparency characteristics makes it suitable for flat-panel displays [1], photovoltaics [2], "smart" electrochromic windows [3], and ozone sensors [4]. The ease of modifying its low carrier density is attractive for tunable, low-loss plasmonic devices. In addition, its free electron-like properties make its macroscopic behaviour simple to

model. However, the interpretation at the micro- and nanoscopic level poses a challenge to controlling the fabrication process and visualizing, or predicting, charge carrier interactions.

This thesis begins in Chapter 2 with some historical perspective on the field of plasmonics, followed by derivations and definitions of common concepts. The chapter then proceeds to outline the metrics involved in finding suitable plasmonic materials, and introduce ITO from a material and semiconductor physics perspective. This includes an overview of its atomic structure, sensitivity to deposition conditions, and the influence of common defects on carrier transport and energy band structure. In Section 2.3, characterization by electron microscopy is introduced and tied in with the visualization of plasmons using electron energy loss spectroscopy (EELS). The experimental details of fabricating and characterizing the structure and electrical properties of ITO nanostructures are detailed in Chapter 3, with the results and their analyses presented in Chapter 4. Concluding remarks and notes on future work are mentioned in Chapter 5. Any supplementary information is provided in the Appendix.

Chapter 2

Background

2.1 The Field of Plasmonics

2.1.1 Historical Overview

From his optical reflectance experiments in 1902 with metallic diffraction gratings, Wood unexpectedly observed sharp changes between high and low reflected intensities within narrow wavelength regions and under certain angles of incidence. He also noted that these anomalies occurred only with s-polarized light (electric field vector perpindicular to the grooves). Through additional experiments involving reflection from diffraction gratings, the idea of the surface plasmon was developed by Ritchie in 1957 [5]. The physical description involved collective oscillations of free electrons at the surface of a metal. Bohm and Pines [6] also interpreted the collective oscillation through the material bulk of Al as a bulk plasmon. These ideas were supported by an EELS experiment by Powell and Swan [7], showing peaks correspondings to both types of resonances in an Al thin film. It took until 1985 for Batson [8] to first spatially map bulk and surface plasmons localized at a boundary, and by 1994 Dawson et al. [9] directly observed an unbounded, propagating surface excitation using a scanning tunneling microscope. The Lycurgus cup, an antique of ancient Rome [10], was found to contain nanoparticles (unbeknowest to the original makers) that would reflect red light and transmit green light based on the scattering by surface plasmons. Building off these observations, the next couple decades witnessed a rise in surface plasmon resonance (SPR) experiments, particularly for biosensing research. Major improvements in density functional theory (DFT) [11], nanofabrication, and electron microscopy [12] unleashed the ability to study these phenomena at the nanometer and atomic level. However, much is still left unexplored, or not fully understood, despite the first questions to give birth to this field

were raised over a century ago.

2.1.2 Plasmon Theory

A plasmon is a general term for a type of quasiparticle that represents the oscillation of a group of electrons. There are different kinds, arising from the type of oscillation (longitudinal or transverse) to the location in the material (bulk or interface). In this thesis, the basic theoretical description of plasmons is adapted from Stefan Maier's *Plasmonics: Fundamentals and Applications* [13]. A simple method, developed in 1900 by the German physicist Paul Drude, of describing the characteristics of a plasmon involves a system of free electrons within a finite metal slab (Figure 2.1a), perturbed by an external electric field $E = E_0 e^{i\omega t}$ of amplitude E_0 and angular frequency ω varying over time t. The material is assumed to be linear, homogeneous, isotropic, and consisting of atomic nuclei represented as static positive charges. The equation of motion for an unbound electron would follow Newton's first law of motion as it is displaced by a distance x by the perturbation:

$$m\frac{d^2x}{dt^2} + m\gamma\frac{dx}{dt} = -qE, \tag{2.1}$$

where m is the electron mass, γ is the damping constant (or collision frequency) related to the scattering time $\tau_s = \gamma^{-1}$, and q is the electron charge. When $m = m_0$, the electron is completely free, or unaffected by the Coulombic potential of the background, else $m = m^*$ when the potential is not ignored and the electrons are *nearly* free.

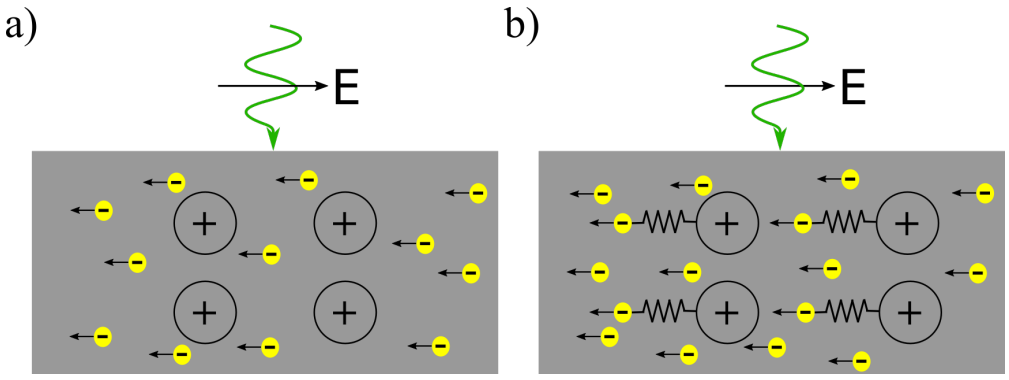

Figure 2.1: Displacement of a) the Drude electron gas (yellow) and b) additional bound charges over a positive ion background as a response to an external electric field of amplitude E.

By assuming a collective displacement of $x = x_0 e^{i\omega t}$, similar in form to the external

driving force, the solution to this differential equation is,

$$x = \frac{q}{m(\omega^2 + i\gamma\omega)}E, \tag{2.2}$$

The displacement of N charge density contributes to a polarization vector P within the metal by,

$$P = -Nqx = -\frac{Nq^2}{m(\omega^2 + i\gamma\omega)}E. \tag{2.3}$$

The electric displacement field D that forms within the material is,

$$D = \varepsilon_0\varepsilon_b E + P \tag{2.4}$$

$$= (\varepsilon_0\varepsilon_b - \frac{Nq^2}{m(\omega^2 + i\gamma\omega)})E \tag{2.5}$$

$$= \varepsilon_0(\varepsilon_b - \frac{\omega_p^2}{\omega^2 + i\gamma\omega})E \tag{2.6}$$

$$= \varepsilon_0\varepsilon(\omega)E, \tag{2.7}$$

where ε_0 is the permittivity of free space and ε_b is the relative, or background, permittivity of the material at frequencies much greater than the plasma frequency ω_p,

$$\omega_p = \sqrt{\frac{Nq^2}{\varepsilon_0\varepsilon_b m}}. \tag{2.8}$$

This is the maximum frequency at which electrons can oscillate to cancel out the external E field. The result is an E field that strongly decays exponentially past the interface (i.e. an evanescent wave), and propagation into the material bulk is not permitted. With this parameter, the behaviour of these charges can be modeled by assuming that the polarization does not occur instantaneously, and that it is frequency-dependent. The (relative) dielectric function,

$$\varepsilon(\omega) = \varepsilon_b - \frac{\omega_p^2}{\omega^2 + i\gamma\omega} \tag{2.9}$$

$$= \varepsilon_b - \frac{\omega_p^2}{\omega^2 + \gamma^2} + i\frac{\omega_p^2\gamma}{\omega(\omega^2 + \gamma^2)}, \tag{2.10}$$

of a Drude material is plotted in Figure 2.2. For $\gamma = 0$ and $\varepsilon_b = 1$, the zero crossing of $\mathrm{Re}\{\varepsilon(\omega)\}$ occurs at $E_c = \hbar\omega_c = \hbar\omega_p$. In the case of a material with electrons bound to the positive cores (Figure 2.1b), as in Au, Equation 2.1 is modified to include its natural

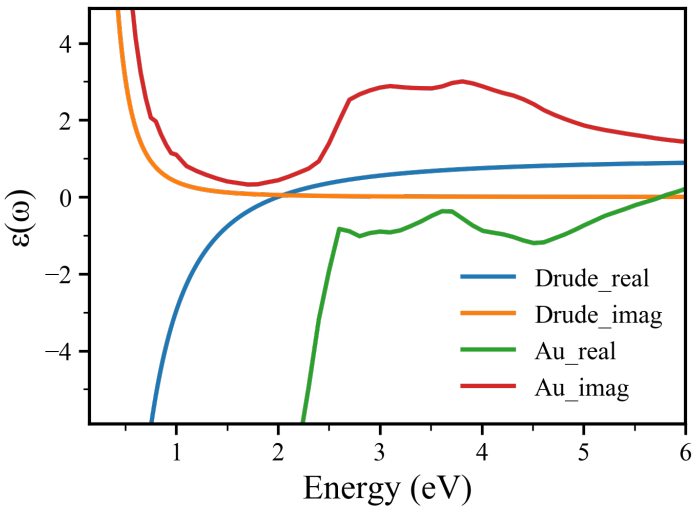

Figure 2.2: Real and imaginary components of the dilectric function for a Drude metal with $\varepsilon_b = 1$, $\omega_p = 2$ eV and $\gamma = 0.01$ eV compared with that of Au (taken from Babar and Weaver [14]).

frequency ω_b. Thus, in addition to the Drude model, $\varepsilon(\omega)$ can exhibit a summation of terms of the form,

$$\varepsilon(\omega) = \frac{\omega_{pb}^2}{\omega_b^2 - \omega^2 - i\omega\gamma}, \tag{2.11}$$

where ω_{pb} is the plasma frequency for the bound electrons. This resonance is represented by the humps in Figure 2.2 for Au.

Electromagnetic waves travelling through a medium (or free space) are described by a time or frequency dependent electric field that is a solution to the wave equation. Equation 2.12 varies with frequency, and provides a convenient picture of two different kinds of waves with wavector K,

$$K(K \cdot E) - K^2 E = -\varepsilon(K, \omega)\frac{\omega^2}{c^2}E, \tag{2.12}$$

where c is the speed of light in vacuum. Equation 2.12 shows that for longitudinal electric fields ($E \parallel K$), $K \cdot E = KE$ leads to $\varepsilon(K, \omega) = 0$. However, for transverse electric fields ($E \perp K$), $K \cdot E = 0$ reveals the phase velocity as a function of frequency (spatial and temporal):

$$v_{ph} = \frac{c}{\sqrt{\varepsilon(K, \omega)}} = \frac{\omega}{K} \tag{2.13}$$

These cases suggest that transverse waves propagate with energy and momentum that

follow Equation 2.13, whereas longitudinal waves only exist at the zeros of $\varepsilon(K,\omega)$. Substituting $\varepsilon(\omega)$ for a Drude material (Equation 2.10) into Equation 2.13 results in the dispersion relation,

$$\omega^2 = \omega_p^2 + k^2c^2, \tag{2.14}$$

where $k = |K|$ is the wavenumber, and plotted in Figure 2.3 as bulk_{rad}. This corresponds to a transverse plasmon that can couple to light (i.e. radiative). When the material becomes transparent ($\omega > \omega_p$), the dispersion of this plasmon approaches that of light in vacuum at high frequencies. For the case where $\omega = \omega_p$, the group velocity $\frac{d\omega}{dk}$ is zero and $\varepsilon(\omega) = 0$ in Equation 2.10, illustrating that a longitudinal plasmon at ω_p exists as a standing wave. This is known as a bulk plasmon resonance. Such a resonance can also be achieved using a high energy electron incident onto the free electron gas. The dispersion of this type of interaction can be modelled using the formulation developed by Lindhard[1], and is represented by $\text{bulk}_{\text{nonrad}}$ in Figure 2.3.

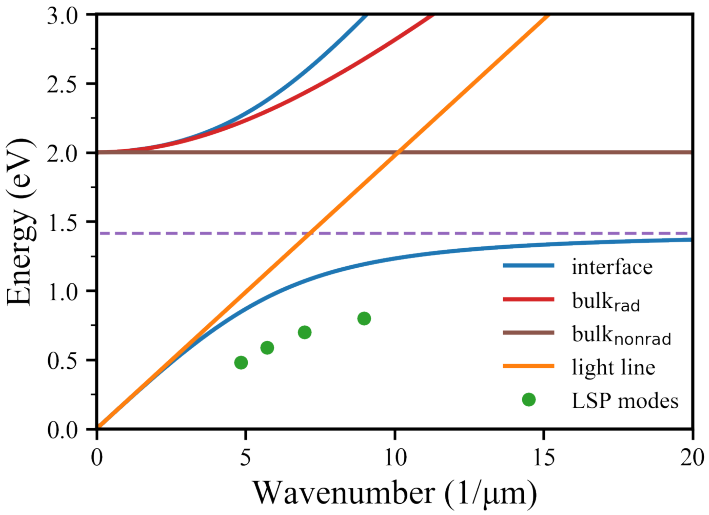

Figure 2.3: Dispersion relations for an undamped Drude metal with ω_p = 2 eV and ε_b = 1, showing the bulk dispersion for photon (red) and electron (brown) excitation. Interface plasmons also have a dispersion above ω_p (blue). SPPs are represented by the blue curve below ω_{sp} and a single LSP mode by the green dot. Light in vacuum (orange) can couple to any modes to the left of this line.

According to Equation 2.14, k is imaginary when $\omega < \omega_p$, which gives the evanescent wave its characteristic exponential decay in amplitude with increasing distance away from the interface. Although forbidden throughout the bulk, wave propagation is still possible along (or guided by) the interface of the metal. Take the permittivity of a

[1]The plotted dispersion curve used $E = \hbar\omega_p = 2eV$, $\alpha = 1$, and $m = m_0$ [15].

dielectric (e.g. air) and semi-infinite metal to be $\varepsilon_1(\omega)$ and $\varepsilon_2(\omega)$, respectively. A propagating wave can be described by finding a solution to Equation 2.12 at the interface by assuming continuity of E at the interface boundary,

$$\varepsilon_1(\omega)E_{1\perp} - \varepsilon_2(\omega)E_{2\perp} = 0 \tag{2.15}$$

$$E_{1\parallel} - E_{2\parallel} = 0, \tag{2.16}$$

to get the dispersion [13][16],

$$k_x = \frac{\omega}{c}\sqrt{\frac{\varepsilon_1\varepsilon_2}{\varepsilon_1+\varepsilon_2}} \tag{2.17}$$

where k_x is the component of the wave vector parallel to the interface of ε_1 and ε_2. This dispersion relation only exists for TM polarized light (parallel to the plane of incidence) and if $\mathrm{Re}\{\varepsilon(\omega)\}$ of each material is of the opposite sign. These waves are known as surface plasmon polaritons (SPPs), which approach c for low wavenumbers. At large k, the SPP approaches a standing wave condition, given the name of surface plasmon (SP), as the group velocity approaches zero. An ideal metal-dielectric interface gives the SP frequency,

$$\omega_{sp} = \frac{\omega_p}{\sqrt{\varepsilon_1+\varepsilon_2}}, \tag{2.18}$$

which can change depending on the dielectric, as well as the amount of damping that arises from material defects. The damping has the added effect of limiting SPPs to smaller wavenumbers. Note also that transverse plasmons right at the interface have a dispersion above ω_p that is slightly different from within the material bulk and moves away from the light line at very high k.

When confining such wave excitations to smaller dimensions (e.g. nanostructures), SPPs can reflect off the physical boundaries to set up standing charge density waves. These can be excited with an electric field that polarizes the nanostructure, so that the wavelength λ_{LSP} of the charge density wave equals,

$$\lambda_{LSP} = 2d, \tag{2.19}$$

$$k = \frac{\pi}{d}, \tag{2.20}$$

where d is the distance between antinodes of the electric field amplitude along the nanostructure surface. Each localized surface plasmon (LSP), or resonant mode, appears as a discrete point on a dispersion curve in Figure 2.3, with each increasing energy,

or mode order, approaching $E_{sp} = \hbar\omega_{sp}$.

Now, for a finite thin film both interfaces must be considered. For small thicknesses, the interface SPs can couple and produce symmetric (even) and anti-symmetric (odd) SPP dispersion curves. The differences in polarization direction are illustrated in Figure 2.4 for a 50 nm thick metal film, along with the nonretarded[2] dispersion for each mode. With increasing thickness, the curves approach each other for large wavevectors to the right of the light line. Hybridization models for such plasmons are explored by Halas and Nordlander [19] in a variety of nanostructure geometries.

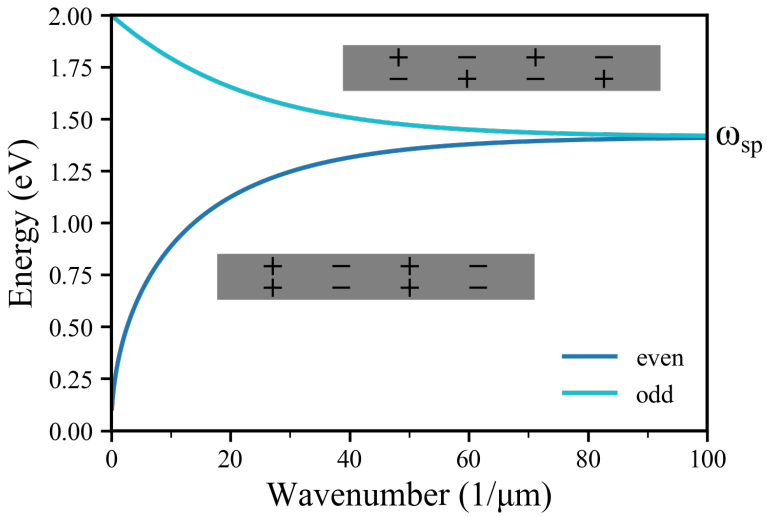

Figure 2.4: Dispersion curves for even and odd coupled modes of a 50 nm thick conductive film.

2.1.3 Plasmonic Materials

The requirement that $\mathrm{Re}\{\varepsilon(\omega)\}$ on either side of an interface has to be of opposite sign spurred research into metal-based plasmonics. Due to their high carrier density N and visible-UV wavelength response, metals such as Au, Cu, Ag, and Al have been the materials from which the field of plasmonics as been built [20]. With the push for commercial plasmonic devices, however, such metals are not completely suitable. Their implementation is hampered by an inherently high damping of resonances, low melting points, high costs, and in the cases of Cu and Ag, oxidation and degradation over time. This is especially detrimental to IR telecommunication operation at the desired μm wavelength band [21] as losses, represented through $\mathrm{Im}\{\varepsilon(\omega)\}$ (Equation 2.10), typically increase with increasing wavelength (decreasing angular frequency ω). These

[2]For a more rigorous analysis on dispersion relations, consult the papers by Economou [17] and Burke et al. [18].

problems have been outlined by Khurgin and Boltasseva [22], who also propose ways to overcome or avoid them, which are explored in this section.

A push towards exploring semiconductors as potential plasmonic materials has been realized in the past decade. The motivation comes from the inability for highly conductive materials to meet a number of metrics to be suitable for plasmonic devices. Most important is the high loss present in metal-based plasmonics, arising from contributions to $\mathrm{Im}\{\varepsilon(\omega)\}$ related to energy band transitions, as shown in Figure 2.5a. The overlap of many atomic orbitals results in a splitting of individual states into higher (anti-bonding) and lower (bonding) energy states. With enough atoms arranged periodically, these states make up energy bands. In semiconductors, interband transitions mainly occur between the occupied valence band (VB) and unoccupied conduction band (CB) states. The energy $E = \hbar\omega_b$ needed to excite a bound electron from the VB needs to be at least greater than the band gap energy E_g. Intraband transitions, occurring between states in the CB and expressed through γ, arise from impurities, surface defects, ohmic losses, and phonon scattering, the latter of which is the most significant for this kind of transition. Both processes add to $\mathrm{Im}\{\varepsilon(\omega)\}$ and increase the strength of plasmon damping, as energy from the plasmon is used to excite these single electron transitions. In the case of metals, Au is shown in Figure 2.5b to exhibit electronic transitions from the d-band to the sp-band near the visible wavelength range. Although this is detrimental to the plasmon lifetime, the major factor in controlling intraband losses involves the carrier density N.

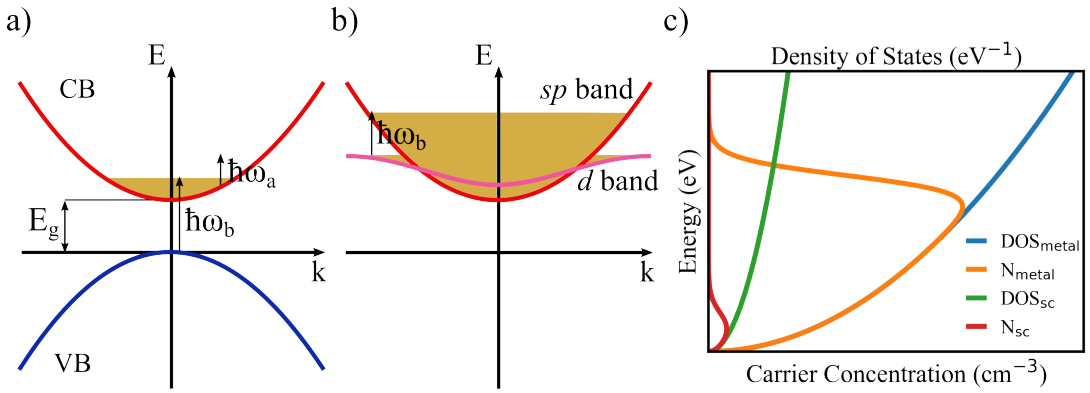

Figure 2.5: a) Simplified E-k band diagram for semiconductors outlining transitions between and within bands requiring $\hbar\omega_a$ and $\hbar\omega_b$ energy, respectively. b) shows the major loss process in Au involving interband transitions from the d-band to unoccupied states in the outermost sp-band. A comparison of the density of states (DOS) and free carrier density N between a generic metal and doped semiconductor is presented in c).

The high N in metals increases the likelihood of intraband transitions and truly restricts their implementation into plasmonic devices. The density of states (DOS), or the

number of available energies for electrons per eV and per unit volume, influences the amount of loss from absorption. Figure 2.5c illustrates how the number of final states for an electron excited with E=$\hbar\omega$ is much greater for metals than semiconductors thanks to the high N and consequently high DOS. Metals typically have $N \sim 10^{23}$ cm^{-3}, whereas highly doped semiconductors are many orders of magnitude less $N \sim 10^{19}$ cm^{-3}, thus contain fewer states available for intraband transitions to occur. Compensation of this loss has been explored by introducing gain media that can induce the stimulated emission of plasmons at a metal surface. One such demonstration by Noginov et al. [23] involves optical light incident on a 44 nm Au particle coated with dye-doped silica. However, this still requires an excitation wavelength larger than the active material. Fully sub-wavelength systems are still far from being realized [22]. This fact just adds to the difficulty of designing metals with high N for plasmonic devices that are supposed to move data faster while consuming less power than current technologies.

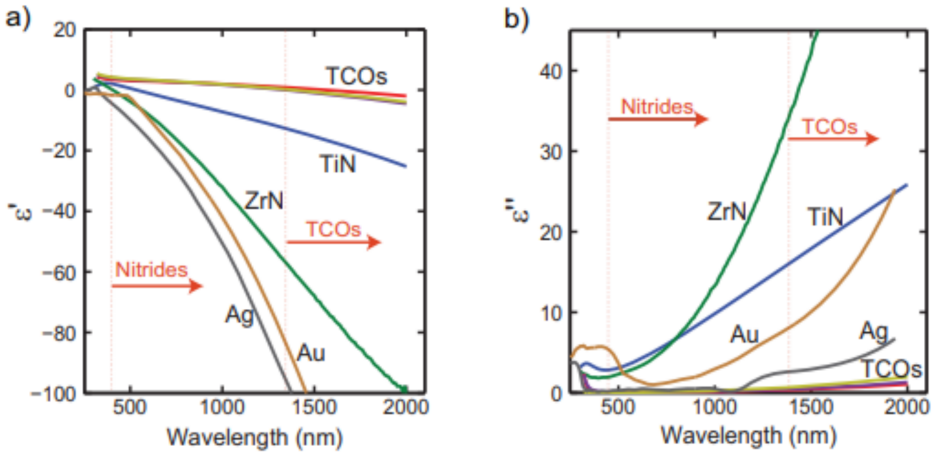

Figure 2.6: Comparing the dielectric function of metals (Ag, Au), nitrides (ZrN, TiN), and TCOs (AZO, GZO, ITO). The arrows show the ranges over which nitrides and TCOs are metallic (and thus plasmonic). Taken from [24].

A number of different ways can be employed to improve materials for plasmonics. Reducing N in metals, or using highly doped semiconductors, are the obvious choices to realizing lower intraband losses. Figure 2.6a and 2.6b display the real and imaginary parts, respectively, of $\varepsilon(\omega)$ for metals, nitrides, and TCOs. In the cases of semiconducting nitrides and TCOs, a lower N has the combined effect of producing a small Re$\{\varepsilon(\omega)\}$ as well as a small Im$\{\varepsilon(\omega)\}$. This is also advantageous for metal-dielectric systems that want comparable values of Re$\{\varepsilon(\omega)\}$. However, such low N limits the plasmonic range to lower frequencies (recall Equation 2.8). Doping these materials heavily enough, including common semiconductors such as silicon (average

doping of 10^{15} cm^{-3} leads to $\omega_p \sim$1 meV), could be detrimental to their electrical and optical behaviour, even inducing phase separation, in the hopes of achieving metal-like characteristics in the optical frequency range. A material free of unwanted defects or impurities is essential to reducing γ and improving plasmon lifetimes. The reduction of phonon scattering by cooling metals is actually demonstrated to decrease the number of phonon scattering events, allowing SPPs to travel 200% further at 80 K than 300 K [25]. Unfortunately the difficulty in keeping materials so cold, as well as the fact that the greatest improvements are seen at low frequences (THz region) [22], prevents such uses in commercial devices. Therefore, reducing N seems to be the easiest way to developing future plasmonic materials.

Suitable materials must also be tested on their compatibility with current silicon-based technologies and manufacturing processes. One obstacle comes from the difficulty in fabricating nanometer-sized components. Ultra-thin metal films for conductive pathways can exhibit discontinuous islands (<50 nm) [26], and the resistance of such films becomes much larger as surface roughness increases. Another drawback involves the unwanted diffusion of metal contacts into silicon, which can create traps within its band gap [27]. Furthermore, some metals like silver and copper react readily with ambient air, forming sulfides and oxides, respectively, that degrade or alter their optical properties. Although extra steps in the processing may be required to implement them [28], some semiconductors are better suited, in part due to their higher melting points. Silicon itself can be plasmonic, but as mentioned previously challenges arise when doping it enough to behave like a metal within the telecommunications frequency band [20]. Therefore many factors need to be addressed when choosing suitable plasmonic materials, such as reactivity to environments and temperature, doping efficiency, and carrier transport at the nanoscale, in addition to the aforementioned unwanted absorption processes and location of ω_p.

Some potential materials and classes of materials being explored include (see Figure 2.7) silicon, germanium, III-V semiconductors (e.g. GaN), ceramic nitrides (e.g. TiN, ZrN), TCOs (e.g. ITO, AZO, GZO, ZnO_2, SnO_2), and graphene [20][29]. The ideal plasmonic material has a lower N than metals, high μ, and no interband transitions. TiN has similar optical properties to Au, with the addition of a low $\mathrm{Re}\{\varepsilon(\omega)\}$, high strength, very high melting points, and already widespread use in transistors. However, interband transitions contribute so much so that the inefficiency in signal transfer is comparable, if not greater, to that of Au. The material with characteristics closest to the ideal candidate is graphene [22]. It has a low N, high μ, long lifetime, and holds promise for applications involving flexible substrates and 2D systems, however the difficulties in fabrication make it challenging to study and engineer in practice [30]. TCOs are in gen-

eral of particular interest because of their optical transparency and high IR conductivity and reflectivity. There are no interband transitions in the IR-visible range, and because the band gap is so large there are fewer free carriers. The majority of losses arise from intraband transitions, but even still these are lower in the IR than for metals (see Figure 2.6b) due to the much lower N and available states for scattering to take place. Complex oxides such as ITO are already widely used in the semiconductor industry thanks to these properties, including their relatively high melting points ($\sim$ 2200 K). The biggest advantage comes from its tunable properties, from the variety in doping mechanisms to its sensitivity to interfaces and fabrication parameters.

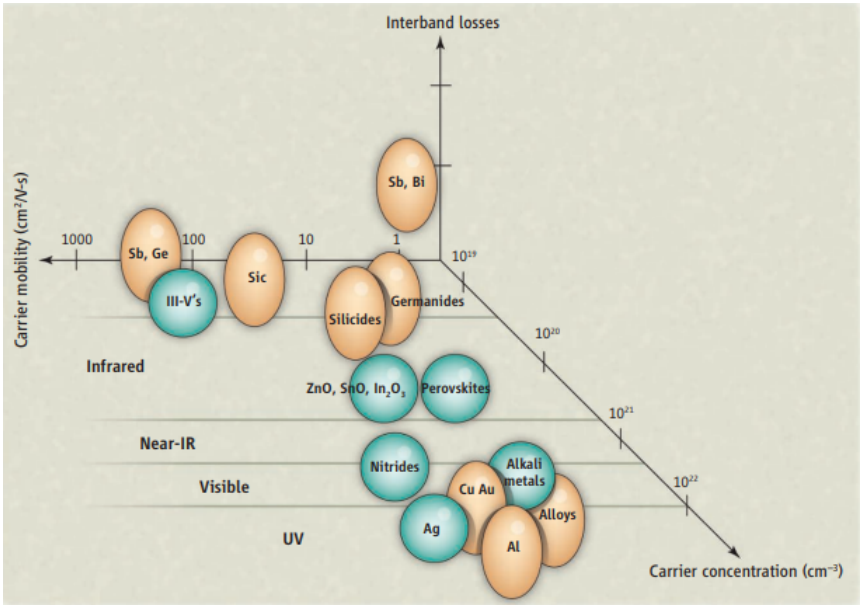

Figure 2.7: Comparing alternative plasmonic materials based on N, μ, and interband losses. Ideal candidates lie within the left of the quadrant, the closest of which are TCOs and nitrides. Chart taken from [31].

TCOs, although promising, still come with disadvantages that make them difficult to work with. For example, the sensitivity to ambient oxygen is non-negligible, requiring the application of protective coatings. Modeling and controlling the fabrication of thin films and nanostructures can be difficult due to the complexity of their atomic arrangements, as well as their surface sensitivity to oxygen and substrate materials. Some elements such as Cd and In are considered toxic, and their supply is not so abundant. Since the demand for compounds such as ITO keeps increasing every year [1], other materials are being explored to replace them, and improvements in recycling hope to lessen their consumption from the raw mineral state. Efforts into understanding these types of oxides from the material science perspective, to the final application level, can lead to a longer usage lifetime and help to grow the field of plasmonics.

2.2 Sn-doped Indium Oxide

In_2O_3:Sn, or Indium Tin Oxide (ITO), is a wide band gap TCO, heavily n-doped to lower its resistivity and increase its transparency for a variety of thin film applications. Additional research on ITO nanowires [32] [33], nanoparticles [34] [35], and patterned films [36] reveals the capacity for this material to function in a controlled manner at the nanometer scale, exclusively within the IR wavelength range. In this section, the bulk and surface characteristics are discussed so that they can be extended to thin film and nanostructure geometries. Some background on thin film growth and carrier transport has been collected from *Nanostructures and Nanomaterials* by Guozhong Cao [37], in addition to a number of scientific articles.

2.2.1 Crystal Structure and Growth

In its most stable form, undoped In_2O_3 crystallizes into a body centered cubic bixbyite (fluorite-type) structure with $Ia\bar{3}$ space group symmetry [38]. Its unit cell is composed of 80 atoms, where In has a coordination number of six (six oxygen atoms, two structural vacancies) to form InO_6, and can occupy two possible configurations. 25% of sites contain vacancies along the body diagonal, also known as the b-sites, whereas 75% are d-sites that contain vacancies along the face diagonal. The configurations result in two ways of bonding: corner (one oxygen atom) and edge (two oxygen atom) sharing, as shown in Figure 2.8a. Rotations of these sites can decrease the coordination number of In atoms, effectively inducing an extra oxygen vacancy. Such distortions in the polyhedra lead to changes in the In-In distance and In-O-In bond angles that contribute to an amorphous structure, as discussed by Buchholz, et al. [38].

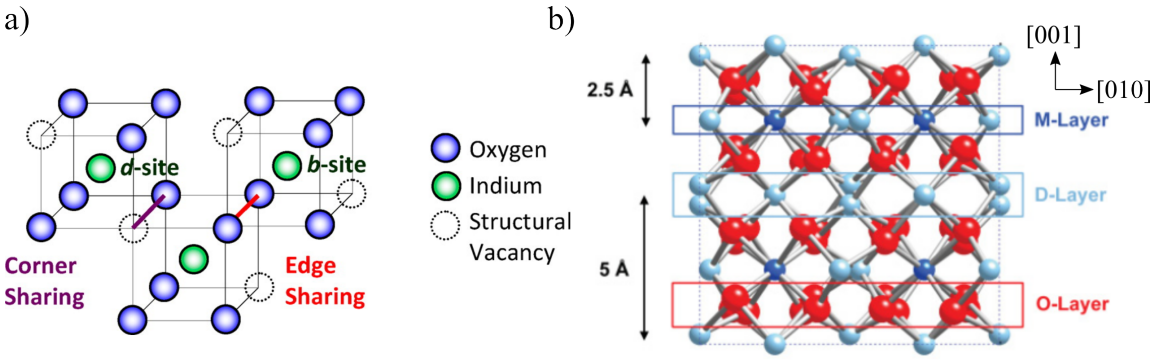

Figure 2.8: a) Arrangements of In sites in In_2O_3, obtained from [38]. Vacancies exist along two directions, forming two distinct polyhedra in a unit cell. b) Unit cell with 1 nm lattice parameter showing layers of oxygen (O-layer), In d-sites (D-layer), and a mix of In d- and b-sites (M-layer), taken from [39].

The atomic arrangement for a crystalline lattice terminated at the (100) surface is displayed and segmented in Figure 2.8b. It reveals unique layers of atomic sites consisting of oxygen atoms (O-layer), d-sites (D-layer), and a mixture of d- and b-sites (M-layer). These layers effectively create a net electric dipole that may cause faceting at the surface, in contrast to the (111) and (110) surfaces which are non-polar and form a smooth surface [40] [41]. Depending on the growth and post-deposition conditions, typical films exhibit preferred orientations along the (100) and (111) directions [42] [43].

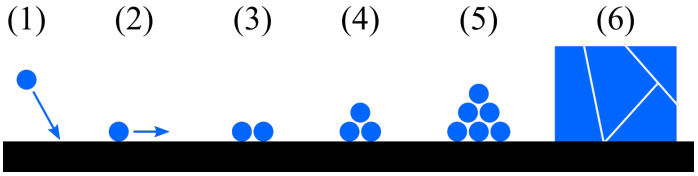

Figure 2.9: Stages of film growth including (1) adsorption, (2) surface diffusion, (3) bonding, (4) nucleation, (5) growth, and (6) grain boundary formation.

The growth of a thin film follows a number of steps outlined in Figure 2.9. The process is aimed at reducing the energy, or tension, at the terminated surface that arises from the attractive forces of the surrounding atoms [37]. Vapour-phase species that are adsorbed onto the substrate surface can then diffuse to a site that has the lowest surface energy (if not desorbed first). Further deposited species become bonded to these adatoms and begin to form unstable unit cell arrangements that attempt to reduce the surface area (and therefore the surface energy). These nucleation sites can mainly arise from the formation of islands, layers, or an island-layer mixture, each structurally different depending on the energies of the vapour-substrate, vapour-film, and film-substrate interfaces. Once a certain size is achieved, the cluster becomes a structurally stable crystal grain that grows until its surface meets other grains, forming boundaries. Further grain growth is possible by the diffusion of solid species throughout the bulk and across grain boundaries.

The number and critical size of nucleation sites have a major influence on the crystallinity of the film. Low substrate temperatures and high deposition rates favour low critical radii, producing many small grains early in the growth process. This can lead to a polycrystalline or amorphous film with only short range order. High substrate temperatures would instead increase the surface energy, and therefore the critical radius, leading to fewer, larger grains. A low deposition rate also helps ensure a highly crystalline film by allowing sufficient surface diffusion of each adatom.

The growth of an ITO thin film may be carried out using a variety of techniques (e.g. pulsed laser deposition (PLD), sputtering, evaporation), of which sputtering has

become widely used. The attractiveness comes from its ability to quickly produce uniform films of low sheet resistance over large areas. Sputtering involves the growth of thin, transparent films by the bombardment of gas ions at an opaque, bulk slab. Such a target is created by pressing powders of In_2O_3 and SnO_2 together into a mold, and sintering the mold above 1250 °C in an oxygen-controlled atmosphere [44]. A schematic of a sputtering process that uses a radio-frequency (RF) source voltage is illustrated in Figure 2.10.

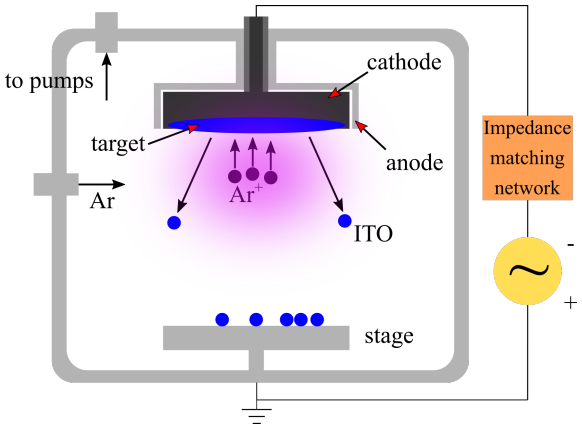

Figure 2.10: Schematic of RF sputtering process in a grounded chamber, which is isolated from the gun cathode. An impedance matching network consists of circuit elements that reduce the amount of signal being reflected back to the AC source.

With RF sputtering, flowing Ar gas into a high vacuum chamber leads to an ionization process caused by the rapid movement and collisions of Ar atoms. As long as the mean free path of an electron is at most the distance between the cathode and anode, further collisions are likely to create an avalanche effect which ionizes a significant portion of the gas and creates a plasma. Through every cycle of the source voltage, the positively charged ions accelerate into the target, dislodging neutral ITO atoms which fall randomly onto a rotating sample stage. Magnets behind the target also prevent the free electrons from moving out of the plasma and bombarding the sample.

Depositions at room temperature (∼23°C) can form a layer of *a*-ITO or *c*-ITO depending on the thickness, substrate, sputtering power, and deposition method [45]. Sun et al. [46] propose that the RF-sputtered growth of ITO thin films at room temperature on amorphous glass follow the Volmer-Weber mechanism (Figure 2.11) of 3D island growth, where species prefer to bond with each other rather than the substrate.

Conductive pathways arise when the islands are large enough to coelesce, which can explain a drop in resistance measurements after a critical deposition thickness. The absence of lattice-matching with the substrate can also lead to voids of missing material

Figure 2.11: Volmer-Weber nucleation mechanism that forms 3D islands of irregular size which eventually cluster together. Typical for growth on amorphous substrates due to the inability for species to lattice match.

throughout the film thickness[3], as seen by Kulkarni et al. [49] and Ow-Yang et al. [47] using cross-sectional transmission electron microscope (TEM) imaging. The voids are distributed vertically between the substrate and air/ITO surface. Kulkarni et al. state that the size of the voids shrink after a post-deposition anneal, effectively increasing the average grain size from a few nanometers to tens of nanometers. In general it seems that increasing the post-deposition annealing temperature [50] and time [51] increases the average grain size and can relieve the mechanical stress of randomly arranged bonds [52][53]. Muranaka et al. [54] experimentally illustrate the amorphous to crystalline transformation using TEM imaging and diffraction. A 55 nm thick film, deposited at room temperature by reactive evaporation, is reported as being fully amorphous (Figure 2.12a). By increasing the substrate temperature for separate depositions, they show that

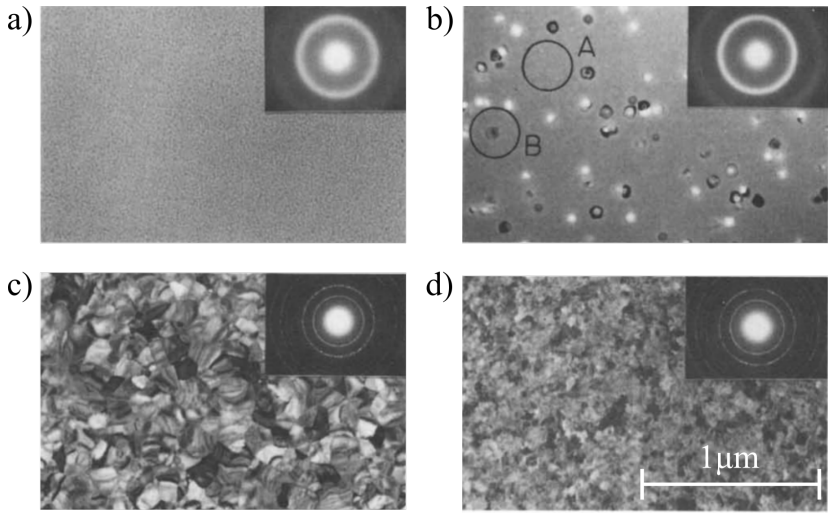

Figure 2.12: TEM micrographs and diffraction patterns for ∼55 nm thick films deposited at a) 0 °C, b) 100 °C, c) 150 °C, and d) 250 °C. The labels A and B in b) specify amorphous and crystalline areas, respectively. Reprinted from [54], with permission from Elsevier.

small single crystals form (Figure 2.12b) and grow to about 140 nm (Figure 2.12c) at 150 °C. The diffraction patterns confirm this change by exhibiting defined rings, char-

[3]Voids in as-deposited ITO are attributed to low adatom mobility [47], and can be avoided by using electron beam evaporation, as proposed by Paine et al. [48].

acteristic of polycrystalline films. Further increases in temperature lead to decreases in grain size (Figure 2.12d) to about 30 nm, at which no dependence is observed anymore. They report a similar trend of increasing grain growth when increasing the thickness from 2.5 nm to 55 nm at a constant room temperature.

Ow-Yang et al. and Paine et al. [48] attempt to model this amorphous to crystalline transition. Ow-Yang et al. include the columnar voids into their explanation, although Paine et al. argue against it, proposing that the nucleation of crystallites occurs from In metal sites throughout the film. These sites experience isotropic growth in all directions until they are confined by each interface. The growth then becomes two-dimensional along the radial direction, as illustrated in Figure 2.13. They also suggest that prior to nucleation, the distorted bonds in the amorphous phase relax into InO_6 sites as the annealing progresses. A consequence of this relaxation involves the creation of oxygen vacancies, which is used to confirm an observed drop in resistivity. Thus, the structural characteristics such as grain size and thickness are strongly linked to its electrical properties.

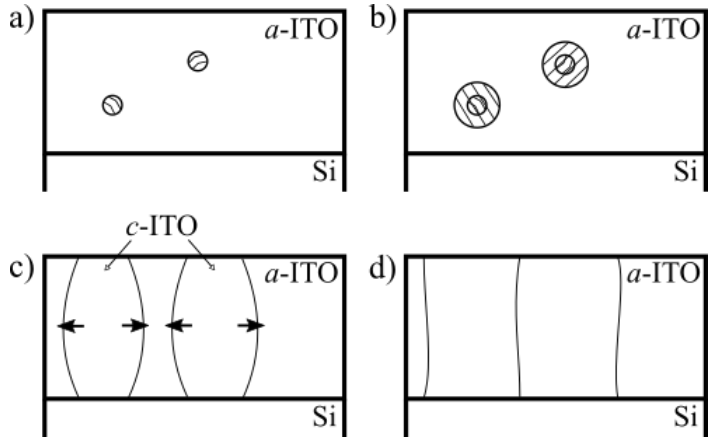

Figure 2.13: Proposed grain growth of ITO, redrawn from [47], showing a) nucleation of crystallites within an amorphous matrix, b) isotropic growth until c) surfaces confine growth radially until d) grains of different orientations meet to form boundaries.

2.2.2 Defects and Carrier Transport

To create ITO suitable for commercial applications, the knowledge and control of different kinds of dopants is essential. Sn, the dopant typically used for low film resistivities and increased carrier density N, can replace In substitutionally up to $\sim$10 wt% before the solubility limit disallows further dopants from contributing a free carrier [55]. Intentionally or not, a variety of defects are added to In_2O_3 to alter these properties (Figure 2.14). For instance, the formation of

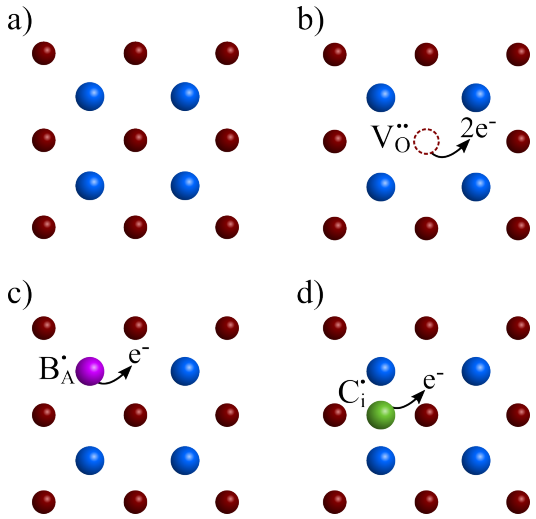

Figure 2.14: Illustration of common doping mechanisms in a) a lattice of metal cations (blue) and oxygen anions (red). Oxygen vacancies are shown as double electron donors in b), whereas c) substitutional and d) interstitial impurities are single donors. Each defect acts as a Coulombic scattering site that contributes to ionized impurity scattering (IIS). Redrawn from [56].

oxygen vacancies $V_O^{\bullet\bullet}$ can be expressed using [57],

$$O_O \rightleftharpoons V_O^{\bullet\bullet} + \frac{1}{2}O_2, \tag{2.21}$$

which can be extended to a thermally ionized vacancy,

$$V_O^{\bullet\bullet} \rightleftharpoons V_O^{2+} + 2e, \tag{2.22}$$

that forms at room temperature to provide two extra free electrons. Although debatable (as discussed in the following section) this gives undoped In_2O_3 its *n*-type conductivity which may be modified during and after deposition. Oxygen can also compensate for donors such as Sn, Ti, or Zr [58] either by filling vacancies or as an interstitial. Li et al. [32] use ITO nanorod arrays to show this dependence of N on oxygen. Grown on a crystalline yttria-stabilized zirconia (YSZ) substrate by the vapor-liquid-solid (VLS) mechanism, the crystalline nanorods are compared under different post-synthesis annealing atmospheres. Transmittance spectra from Fourier transform infrared spectroscopy (FTIR) reveal an increase in ω_p from ~1.53 eV to 1.61 eV when annealed in N_2 gas. They also find a slight decrease in ~5% O_2 gas (the remainder is N_2), with a more dramatic decrease to 1.12 eV in ambient air. Because the rods were crystalline prior to annealing, the assumption is made that the Sn dopants already contribute electrically and that the $V_O^{\bullet\bullet}$ concentration is what changes. The reducing N_2 atmosphere increases N, whereas

the oxidizing atmosphere decreases N.

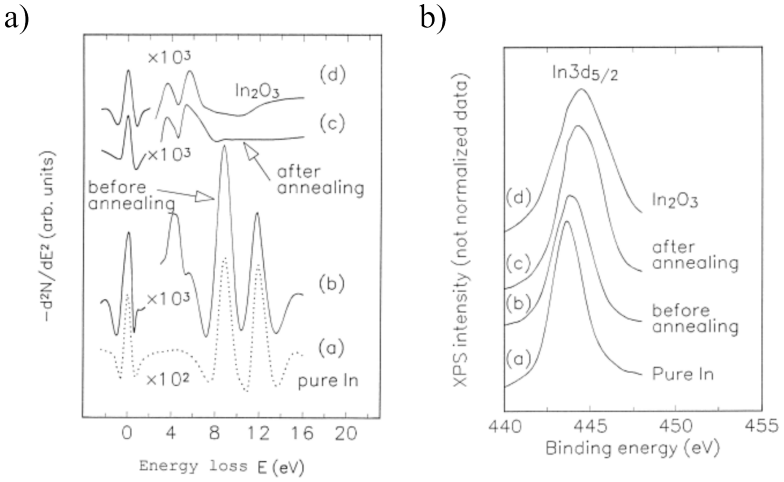

Figure 2.15: a) Disappearance of In surface (9 eV) and bulk (12 eV) plasmon peaks in low-energy EELS spectra, attributed to oxidation during annealing. Further evidence of this is shown in b) XPS spectra of the In $3d_{5/2}$ peak as it shifts with the anneal. Reprinted from [59], with permission from Elsevier.

Besides $V_O^{\bullet\bullet}$, hydrogen $H_i^{\bullet}$ and $In_i^{\bullet}$ interstitials can also be considered as unintentional dopants that contribute to the n-type conductivity. Zhu et al. [59] characterize unannealed and air-annealed ITO (5 wt% Sn) films using EELS and x-ray photoelectron spectroscopy (XPS). Low energy EEL spectra show a clear disappearance of pure In metal surface (9 eV) and bulk (12 eV) plasmon peaks after annealing. Coupled with XPS measurements showing a shift of the In $3d_{5/2}$ peak at 443.6 eV to 444.4 eV post-anneal, which is close to that of pure In_2O_3 (444.6 eV), they conclude that In oxidizes when annealed in air, and they attribute the plasmon peak disappearance to this oxidation. Additionally, no changes in characteristic Sn peaks are observed, and so they propose that the deposition can form defects and In metal agglomerations that contribute to N. These findings are supported by Albrecht et al. [60], who provide an additional hypothesis of $H_i^{\bullet}$ playing a dopant role to help explain the increase in In_2O_3 conductivity under reducing atmospheres. They reference DFT calculations by Limpijumnong et al. [61] that show $H_i^{\bullet}$ to be effective donors under In-rich conditions.

In addition to phonons, lattice defects, and grain boundaries, these impurities, as well as others detailed in the defect model by Frank and Köstlin [55], control the electrical conductivity σ and mobility μ through electron scattering. The average distance between collision events is known as the total mean free path (MFP) λ_T, and Mathiessen's rule relates the scattering contributions to the total scattering rate λ_T^{-1} [37],

$$\frac{1}{\lambda_T} = \frac{1}{\lambda_{th}} + \frac{1}{\lambda_D} + \frac{1}{\lambda_S}, \tag{2.23}$$

where λ_{th}, λ_D, and λ_S are the MFPs between phonon, defect (impurity, lattice defect, grain boundary), and surface collisions, respectively. σ, or the inverse of resistivity ρ, is defined by,

$$\sigma = \frac{1}{\rho} = \frac{l}{RA}, \tag{2.24}$$

relating the cross-sectional area A, length l, and resistance R of a resistive element. Values of ρ are on the order of $\sim$1x10^{-4} Ωcm for high quality ITO [62]. 4-point probe measurements for films of thickness d (much smaller than the probe spacing) can help calculate ρ by measuring the sheet resistance $R_s = \frac{\rho}{d}$. The speed at which a charge carrier can travel through a material in the presence of an electric field can expressed through the mobility μ,

$$\mu = \frac{q\tau}{m^*} = \frac{q\lambda_T}{m^* v_F} = \frac{\sigma}{Nq}, \tag{2.25}$$

where v_F is the Fermi velocity. This can follow a more complicated empirical relationship,

$$\mu = \mu_{min} + \frac{\mu_{max} - \mu_{min}}{1 + (\frac{N}{N_{ref}})^{\alpha}} \tag{2.26}$$

for heavily doped materials, where μ_{min}, μ_{max}, α, and N_{ref} are fit parameters.

A defect's physical size and charge state control the Coulomb potential around it. The scattering process involves either no energy loss (elastic) or energy loss (inelastic), the latter of which impacts σ and μ. For thin films and nanostructures that have comparable dimensions to the MFP of electrons traveling in the bulk (λ_b), the Thompson model,

$$\lambda_f = \frac{d}{2}\left(ln\left(\frac{\lambda_b}{d}\right) + \frac{3}{2}\right), \tag{2.27}$$

where λ_f is the MFP of the film, is required. Therefore, substituting this expression into Equation 2.25 suggests σ and μ are dependent on the film thickness for small d. Other mechanisms intrinsic to the material, such as ionized impurity scattering (IIS), may be significant.

IIS is labelled as the major hinderance to μ and σ of In_2O_3 [58] and ITO [55] thin films. The ionization of both structural vacancies and dopant atoms, such as Sn, creates a positively charged potential within the lattice that interrupts current flow. In *a*-ITO, the Sn does not contribute to the free carrier concentration, and may only contribute to elec-

tron scattering by neutral impurities [63]. For films annealed in a reducing atmosphere, Yamada, et al. [64] demonstrate that μ decreases as Sn is activated, consistent with the IIS mechanism. They also discover a similar effect when annealing in an oxidizing atmosphere, suggesting that the chemical state of Sn changes to accommodate interstitial oxygen atoms. Such Sn-O complexes are included as major scatterers contributing to IIS.

Grain boundary scattering (GBS) also has a role in influencing the carrier transport throughout ITO over different thicknesses. The PLD-deposited films on 300 °C substrates by Kim et al. [65] interestingly show that the surface roughness and R_s decrease (N, μ, and ω_p increase) exponentially with increasing thickness until approximately 200 nm, at which point any further changes are much more gradual. They attribute these findings to the increase in grain size; thicker films have larger grains, and fewer grain boundaries for carriers to scatter from. However, this is contrary to other studies

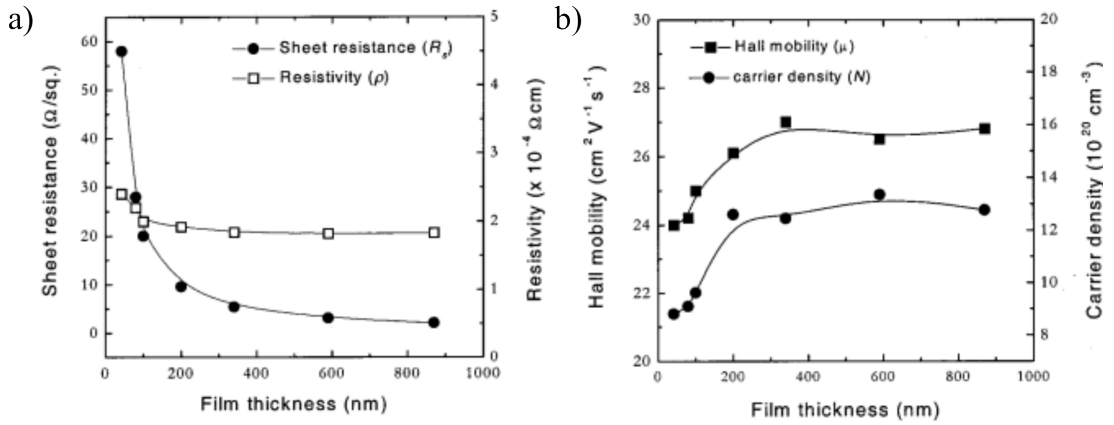

Figure 2.16: a) Sheet resistance R_s and resistivity ρ with b) mobility μ and carrier density N for films of varying thicknesses at 300 °C. Reprinted from [65], with the permission of AIP Publishing.

[66] that suggest GBS is insignificant in relation to IIS, due to the small MFP of carriers with respect to grain size. The actual temperature-dependent scattering mechanisms may be outlined by Lee et al. [67] and can be extended to the transport properties as a function of thickness. They note two distinct temperature regions in which either GBS or IIS are the dominant scattering mechanisms in sputtered films. GBS is significant for depositions with substrates up to ∼300 °C, a region exhibiting both amorphous and polycrystalline phases. Here, μ is proportional to temperature as GBS decreases and more Sn dopants are incorporated. At even higher substrate temperatures, these dopants are so prevalent that IIS becomes significant. Therefore, the observations by Kim et al. may be due to the deposition temperature residing in the GBS-dominated region. Nevertheless, such thickness-dependent properties are consistent in the literature, and some

also propose that when GBS is neglected, substrate interface defects become important for very thin films [68] [69]. Ultimately, the temperature must also be accounted for to understand the carrier transport properties as a function of thickness.

Finally, surface defects may play a large role in the conductivity of this material. Lany et al. [57] suggest that σ in undoped In_2O_3 arises from surface defects as opposed to those from the bulk, which could make the material very sensitive to air, substrate, and grain boundary interfaces. They compare σ at high temperatures for equally thick polycrystalline and single crystal In_2O_3 to show that the polycrystalline sample exhibits an order of magnitude higher σ, concluding that N is higher at the boundaries. Additionally, they perform DFT calculations and Hall measurements for epitaxial In_2O_3 thin films on a YSZ substrate to show that (111) surface contributions dominate for thicknesses up to 150 nm. Such surface states include oxygen vacancies $V_O^{(111)}$ and In adatoms $In_{ad}^{(111)}$, which contribute two and one free carriers, respectively. Their results, illustrated in Figure 2.19 of the following section, propose that N arising from V_O is much lower within the bulk material. An examination of the energy states of such defects can provide some insight into their influence on the carrier transport.

2.2.3 Energy Band Structure

The band gap of ITO is a controversial characteristic due to the contradicting values reported from different optical experiments and DFT calculations. The relatively large number of atoms within a unit cell has made it especially difficult to perform first-principles calculations until the first attempt by Odaka, et al. [61] in 1997. The most widely cited value of $\sim$3.75 eV is determined through light absorption experiments [70]. However, some sources report seeing an onset of low absorption at $\sim$2.7 eV [71] [58]. DFT calculations predict band gaps of about 1.5 eV [72], or suggest multiple gaps that try to explain the variation in literature [73]. The debate is extended to the locations of defect states within the gap. To understand where these discrepancies come from, some semiconductor band theory will now be explored.

The assumption that each band is parabolic in energy E and momentum k allows for the effective mass of free electrons m^* to be described by the curvature of the CB edge,

$$m^* \propto \left[\frac{d^2E}{dk^2}\right]^{-1}. \tag{2.28}$$

This means that a large curvature induces a small m^*, and from Equation 2.25 a large μ. ITO has $m^* \sim 0.3m_0$ [2], which gives it its low DOS (i.e. fewer possible intraband transitions) and high μ (excluding effects from IIS and GBS). In reality, the CB is not

perfectly parabolic, and states higher in energy will have an m^* that differs from those near the bottom of the band [33]. m^* is observed to increase exponentially for highly doped semiconductors [74] as more CB states get filled, thus complicating the accurate modeling of carrier transport with the use of empirical relationships such as Equation 2.26.

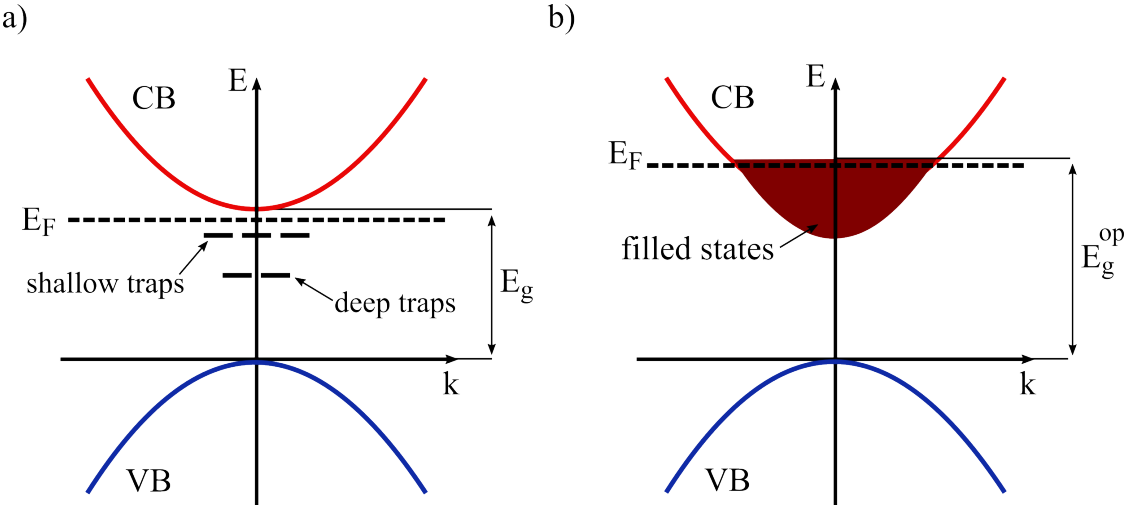

Figure 2.17: Simplified band diagrams illustrating a) *a*-ITO with deep and shallow energy states being occupied by possible V_O, In_i, or H_i. Sn occupies deep trap states unless electrically active in b) *c*-ITO where they form an impurity band over CB, enlarging E_g.

An indirect band gap is a consequence of the misalignment of the VB maximum and CB minimum in k-space. This makes it unlikely to promote a VB electron to a CB state because the electron, in addition to extra energy, requires some change in momentum. Therefore, direct transitions of $\hbar\omega$ absorption and carrier recombination are much more likely to occur than indirect transitions. Doping can help increase the chance of traversing this gap by creating energy levels within it. Figure 2.17a shows these localized states (i.e. shallow donors), which effectively decrease the optical gap E_g^{op} with respect to the fundamental band gap E_g. In ITO, $V_O^{\bullet\bullet}$, $Sn_{In}^{\bullet}$, $H_i^{\bullet}$, and $In_i^{\bullet}$ can all be considered as shallow donors [58], however not enough evidence supports this. For example, in *a*-ITO, since Sn does not contribute electrically [63], its location can be argued to reside at a deep trap level (approximately halfway between the band edges), and so the extra valence electron is much less likely to populate the CB compared to a shallow trap that would likely exist in the crystalline form. Similarly, Tomita et al. [75] suggest that $V_O^{\bullet\bullet}$ occupy deep states and that $In_i^{\bullet}$ are responsible for the n-type conduction in *c*-In_2O_3.

The Fermi energy E_F is defined as the maximum energy of occupied states at 0 K. At room temperature (kT$\sim$0.025 eV), this level is shifted to a higher energy because of

the increased probability of inducing a transition between higher states. When n-doping semiconductors, the introduction of additional states shifts E_F to near the CB minimum. For heavy doping, the localized states are so numerous that they can form an impurity band that overlaps with the CB. The Burstein-Moss shift, illustrated in Figure 2.17b, describes the increase in E_g^{op} when enough dopant states exist that the bottom of the CB is filled. This compensates for the slight decrease caused by shallow donor states within the gap region [70].

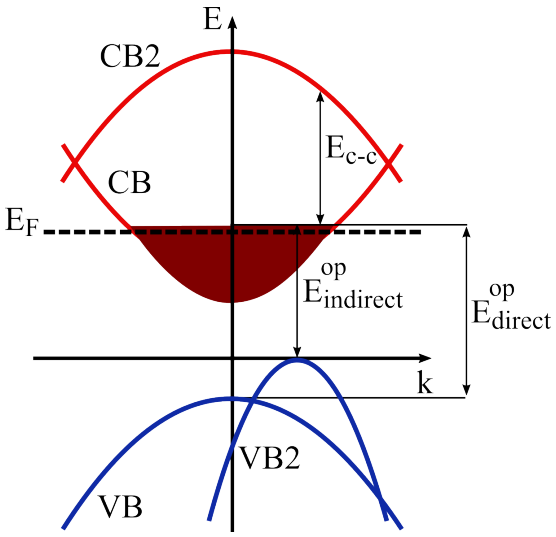

Figure 2.18: Simplified band diagram redrawn from [76], showing possible indirect and direct transitions between VBs (VB and VB2) and CB states. Additional transitions can occur between lowest lying CBs (CB and CB2) for sufficiently high *n*-doping.

The differing reported band gaps partly arise from an observed slight increase in light absorption around 2.7 eV, and significant absorption in the UV. This suggests that these experiments are witnessing both a direct and indirect band gap. In fact, DFT calculations by Karazhanov et al. [71] confirm this and show that direct transitions actually come from below an indirect VB maximum (Figure 2.18), although the values are severely underestimated when compared to experiment. It is also theorized that this weak absorption takes place between states within different CBs (>2 eV) [76]. Overall, there is still dispute on the origin of the band gap, but based on experiments, the general agreement of its value locates it within the UV wavelength range (∼3.75 eV).

The band diagrams from Lany et al. can further add to the variety of dopant states in ITO (Figure 2.19a). $V_O^{(111)}$ and In adatoms $In_{ad}^{(111)}$ at the (111)-terminated surface produce shallow energy states close to the CB. Since In has a 3+ valence charge, their calculations show that it creates one filled and one half-filled state, where the former transitions between shallow and deep levels for bulk and surface configurations, respectively. The opposite transition (deep state in bulk turns into shallow at the surface) is

presented for $V_O^{\bullet\bullet}$. These surface defects can contribute much more to the carrier trans-

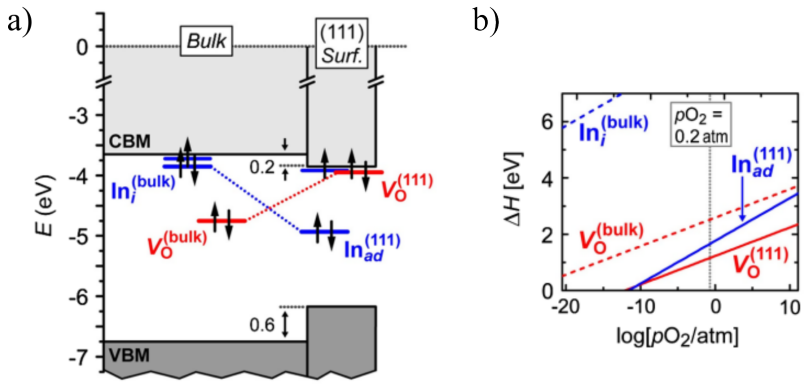

Figure 2.19: a) Calculated energy band diagrams for bulk In_2O_3 and the [111] surface, comparing the positions of defects in the bulk (In_i^{bulk}, V_O^{bulk}) and at the surface ($In_{ad}^{(111)}$, $V_O^{(111)}$). The formation energies ΔH of each defect are shown in b) as a function of oxygen partial pressure pO_2 at a temperature of 1023 K. Figures obtained from [57].

port properties than the bulk. Note also that a narrowing of the band gap is evident at the surface. Within the bulk, it may seem that In_i^{bulk} should play a large role in contributing free carriers. However, Figure 2.19b shows that the formation energy of such a defect is relatively high (>6 eV) for increasing O_2 concentrations. In fact, both defects involving In and oxygen have lower formation energies at the surface. Space-charge simulations from King et al. [77] demonstrate that the outcome of these surface donor defects is an accumulation layer of electrons near the surface. The ionized defects are positively charged, and the free electrons attempt to screen this charge from the material bulk. Although they show that this accumulation effect can be reduced by Sn-doping, further work is needed to supplement these simulated results and provide a better understanding of the band structure at different surfaces for different defect concentrations.

2.3 Characterization with Electron Microscopy

2.3.1 Imaging

A lens diagram is presented in Figure 2.20, which is the basic component of an imaging system. Here, light rays refract when passing through a transparent lens and can be traced from the object, point O, to the image plane at point I as a flipped reconstruction of the original object. Any incident rays that are parallel will converge at a focal point F in the back focal plane (BFP). In contrast, lenses in electron microscopes consist of a set of current-carrying Cu coils that produce a magnetic field, deflecting the electron

trajectory as it passes through. Simply varying the current will control the strength of deflection through the lens, and therefore the beam convergence and magnification.

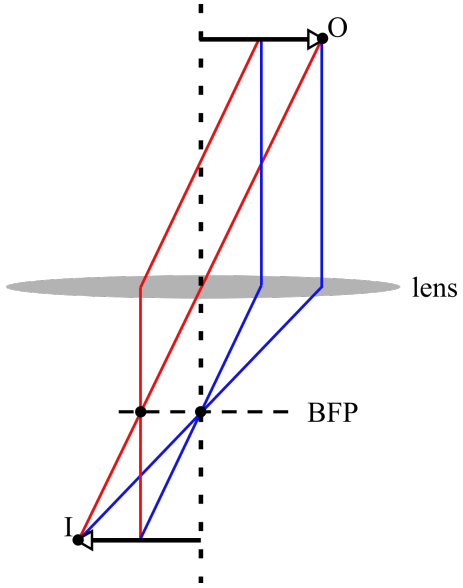

Figure 2.20: Basic ray diagram for a thin lens. Rays are refracted in relation to the center dotted line (optic axis) unless they pass through the middle of the lens.

A scanning electron microscope (SEM) utilizes these magnetic lenses to focus a beam of electrons (1-30 keV energy) onto a sample. The source gun can use a potential field to extract electrons from a thermionic (e.g. heated LaB_6) or field emission (e.g. ZrO_2-coated tungsten) filament [78]. The electrons are accelerated to a specified kinetic energy and collected by these lenses to form a beam with the desired spot size and current at the sample plane. A number of interactions with the sample can occur, one of which involves so-called secondary electrons. The beam can eject these electrons from near the sample surface, which are then attracted to a charge-coupled device (CCD) by a small potential field. An image is formed when the probe is rastered across the sample area and the detected CCD signal is shown on an external computer monitor. The intensity value at each pixel corresponds to the number of secondary electrons captured by the CCD at the specific beam location.

An interesting application of the SEM concerns the fabrication of nanostructures using electron beam lithography (EBL). In general, lithography is a printing technique used to define areas in which to deposit material. It involves the separation of this material from undesirable areas using a mask, typically a photo-sensitive polymer, that is exposed to UV light or an electron beam. The exposed areas are weakened and, when removed, outline the areas in which to deposit material. Conventional UV lithography is useful for defining micro- to millimeter size areas of metal contacts for photovoltaics,

whereas with EBL the small probe size allows for the definition of dimensions down to tens of nanometers. This is dependent on the mask material, dosage (current per unit area), and exposure time at a specific area. Furthermore, the software used to control an EBL probe allows the formation of custom patterns and shapes with ease.

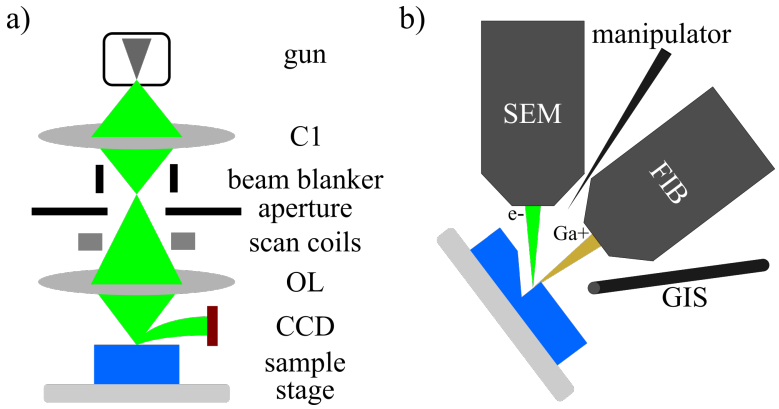

Figure 2.21: Schematics of a) SEM based on the JEOL 7000F design and b) FIB operation.

SEMs can also host a focused ion beam (FIB) to modify the imaging area at high spatial resolution. Ions such as Ga^+ may be accelerated onto the sample to mill, or sputter off, material. To alleviate undesirable sputtering, ion implantation, or damage of the underlying structure, the milling can be assisted with the introduction of metal-organic molecules through a gas injection system (GIS). Following the bonding of these molecules to the sample surface, they can be decomposed by the FIB primary beam over a selected area. The organic component is sputtered off while the metal, such as tungsten, remains. Thus, the FIB can also perform additively, and in conjunction with a manipulator probe the milled section can be transferred onto a TEM grid for analysis. Figure 2.21b illustrates the relative positions of the FIB, GIS, and manipulator with respect to the sample.

2.3.2 The Transmission Electron Microscope

The transmission electron microscope (TEM) also utilizes a set of magnetic lenses, but to image very thin specimens ($\sim$<100 nm) so that high energy (60-300 keV) electrons pass through. A schematic is given in Figure 2.22 (left) for a conventional two-condenser system. The condensers C1 and C2, along with the current-limiting C2 aperture, determine the spot size, current, and convergence angle at the sample. The upper OL forms the parallel beam that is diffracted by the sample and projected onto a phosphor-coated screen or CCD, forming a bright field (BF) image. For simplicity, the set of lenses below the lower OL is omitted in the diagram. Depending on the strength

of some of these post-specimen lenses (diffraction lens, intermediate lens), the BFP can be projected onto the image plane to view the diffracted beams in reciprocal space.

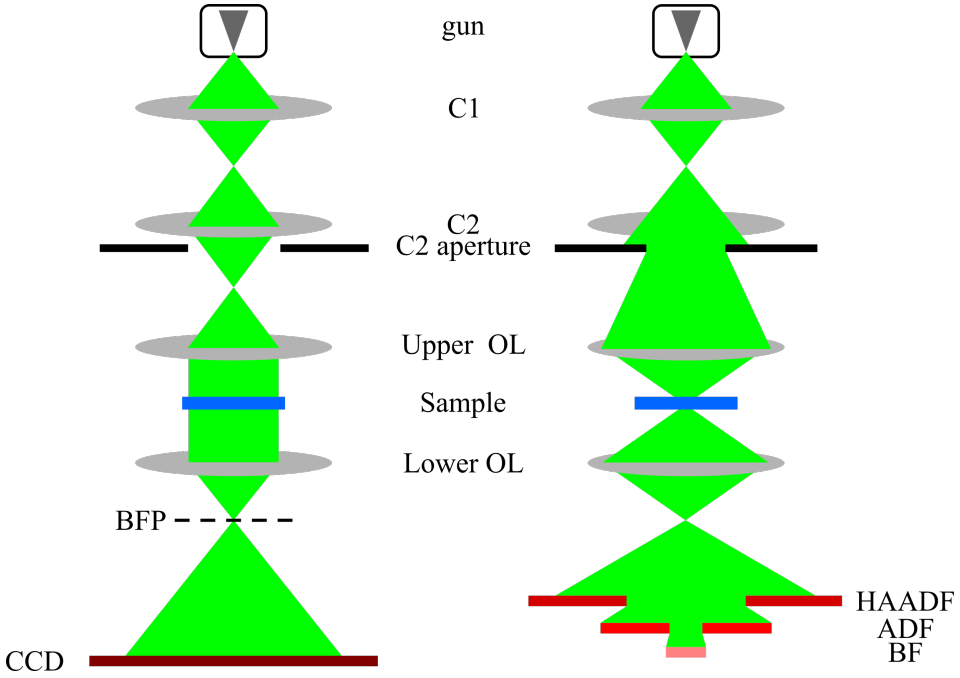

Figure 2.22: TEM diagram for parallel illumination of sample (left) and STEM configuration for a convergent probe (right).

Figure 2.22 (right) also displays the layout of a scanning TEM, or STEM, in which the probe is converged to a small size and scanned (rastered) across the sample. The scanning is controlled by a set of deflection coils to ensure that the beam travels parallel to the optic axis at each point. The C2 lens is de-excited to allow the upper OL to focus the probe (few systems have a third condenser lens to create an even smaller probe). Aberration-corrected STEM imaging can form a small enough probe to even resolve individual atoms when aligned along a set of crystal planes (i.e. the zone axis). To view these images, annular dark field (ADF) and high angle ADF (HAADF) detectors capture a range of electron scattering angles, from which the contrast arises mainly from variations in atomic number and thickness (Z-contrast). The direct, or undiffracted, beam is collected by a retractable BF detector, or a spectrometer for analytical techniques such as EELS as pictured in Figure 2.23a and outlined by Kociak and Stéphan [79].

EELS involves imaging the sample (object plane) at a scintillator (image or dispersion plane). The paths of electrons are dispersed with respect to their energy as they exit the sample and pass through the spectrometer entrance aperture. A magnetic field acts to separate them just as an optical prism separates photons by their wavelength (energy). A set of post-prism lenses are used to control the magnification and focus of the beam

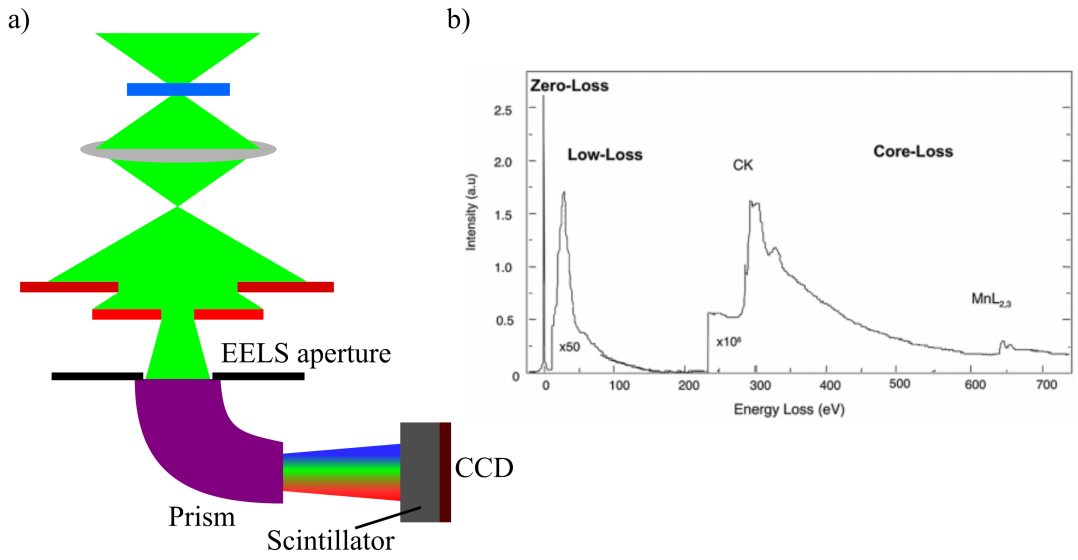

Figure 2.23: a) Schematic of the direct beam travelling into the spectrometer to be dispersed in energy and form b) a typical EELS spectrum, obtained from [79].

onto the dispersion plane. Photons emitted from the scintillator are then captured by a CCD to form a spectrum of intensities. STEM mode is able to correlate each spectra with a position on the sample plane, effectively creating a 3D dataset (position X, position Y, energy Z).

2.3.3 The Low-Loss Region

Optical tools for characterizing low energy excitations rely on fitted models and are limited by the diffraction of light. EELS has the ability to directly provide information about the material's dielectric function and spatially map plasmons at the nanoscale, which include additional LSPs that cannot be excited with light (i.e. dark modes). A typical spectrum from this technique is plotted in Figure 2.23b. The zero-loss peak (ZLP) represents elastic scattering (no energy loss) from the sample. The intensity of this peak shows that the majority of electrons interact very little, or not at all, with the sample. With inelastic scattering (energy loss), the low-loss region consists of peaks corresponding to plasmon resonance excitations (both surface and bulk types) and energy band edges. The low-loss region is where Powell and Swan [7] observe EELS peaks and interpret them as plasmons using the formalism developed by Ritchie [5]. Batson and Silcox [80] further contribute with studies on momentum-resolved EELS. Since then, authors such as Nelayah et al. [81][82],(Figure 2.24), Bosman et al. [83], and Rossouw et al. [84] have successfully visualized their spatial distribution to a high resolution across nanostructures. Supplemental techniques such as cathodoluminescence

(CL) [85] and electron energy gain spectroscopy (EEGS) [86] are also being explored to gain more information about material defects and photon-electron interactions. In this section, the pioneering work of Ritchie [5], Raether [87] [16], and the texts by Egerton [15] and Daniels [88] are detailed to provide a physical description of the low-loss EELS technique.

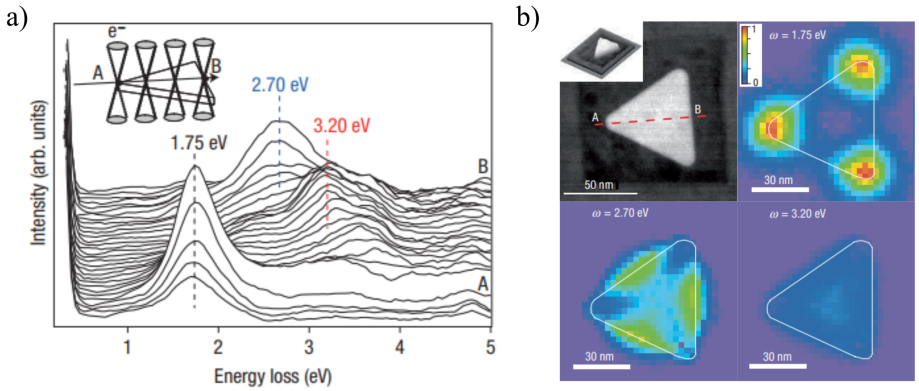

Figure 2.24: LSPs detected in a Ag triangle in STEM mode. a) Raw EELS spectra from a corner to the opposite edge, highlighting three peaks (1.75 eV, 2.70 eV, and 3.20 eV) corresponding to LSP excitations that are spatially mapped in b). Probability of energy loss is greatest for red pixels. Reprinted by permission from Springer [81].

The single inelastic interaction between an electron of energy E_0 and momentum $k_0 = |\mathbf{k}_0|$ with a material is given in Figure 2.25a. The electron loses energy ΔE and momentum $q = |\mathbf{q}|$ as it scatters through an angle θ with respect to the incident direction. The vector $\mathbf{q}$ represents the momentum imparted to the sample, with both components $q_\perp$ and $q_\parallel$ illustrated. Each can be shown to be approximately equal to,

$$q_\perp = \frac{mv\theta}{\hbar} = k_0\theta \tag{2.29}$$

$$q_\parallel = k_0\theta_{\Delta E}, \tag{2.30}$$

where $q_\perp$ is the projection seen by the CCD and $\theta_{\Delta E}$ is the characteristic scattering angle,

$$\theta_{\Delta E} = \frac{\Delta E}{2E_0}, \tag{2.31}$$

or an approximation[4] for the most probable scattering angle for an energy loss event of

[4]Ignoring relativistic effects gives 8 % and 18 % error in $\theta_{\Delta E}$ for 100 keV and 300 keV electrons, respectively [15].

ΔE. Combining the components gives the total scattering vector amplitude,

$$q^2 = k_0^2(\theta^2 + \theta_{\Delta E}^2). \tag{2.32}$$

The probability of energy ΔE and momentum q transfer per unit length can be expressed as,

$$P(\mathbf{q}, \Delta E) = P_b + P_s, \tag{2.33}$$

where P_b and P_s are the bulk and surface contributions, respectively. When considering a very thick film, the scattering probability is defined only by P_b,

$$P_b = t\left(\frac{q_e}{\pi\hbar v}\right)^2 Im\left(-\frac{1}{\varepsilon(\Delta E)}\right)\frac{1}{\theta^2 + \theta_{\Delta E}^2}, \tag{2.34}$$

where q_e is the electron charge. Equation 2.34 can be broken into three components. First, the probability of inelastic scattering is directly proportional to the thickness t, and inversely proportional to the velocity v-squared (kinetic energy) of the incident beam. Second, an inverse dependence on q-squared is evident when considering Equation 2.32, suggesting that the likelihood of scattering decreases at larger angles. This is seen by the angular distribution of a 100 nm thick film in Figure 2.25b (for normal incidence). At $\theta = 0$, bulk excitation is maximum with $\mathbf{q}$ purely parallel to $\mathbf{k}_0$, and increases in θ reduce the probability by a factor of θ^{-2}. The final term is known as the energy loss function,

$$Im\left(\frac{-1}{\varepsilon(\Delta E)}\right) = \frac{Im\{\varepsilon(\Delta E)\}}{Re\{\varepsilon(\Delta E)\}^2 + Im\{\varepsilon(\Delta E)\}^2}, \tag{2.35}$$

which represents the influence of the dielectric environment and acts as a weighting function to the scattering distribution. This is plotted in Figure 2.25c for a Drude-like film with nonzero damping ($\gamma \neq 0$). Recall that for an ideal Drude film, a bulk plasmon excitation occurs at $E_p = \hbar\omega_p$, and with Equation 2.35 the presumption can be made that an electron cannot excite a bulk plasmon for $\gamma = 0$ (since this causes $\mathrm{Im}\{\varepsilon(\omega)\} = 0$). As $\gamma \to 0$ however, the loss function consists of a peak very near E_p as long as $\mathrm{Im}\{\varepsilon(\omega)\}$ remains low (i.e. no interband transitions). For background permittivity $\varepsilon_b > 1$, bulk excitation (and therefore the loss function peak) instead occurs at a reduced energy[5], since $E_p \propto \varepsilon_b^{-0.5}$, which corresponds to the zero crossover of $\mathrm{Re}\{\varepsilon(\omega)\}$. Again, this is true when $\mathrm{Im}\{\varepsilon(\omega)\}$ is small.

[5] Also known as the screened bulk plasma energy

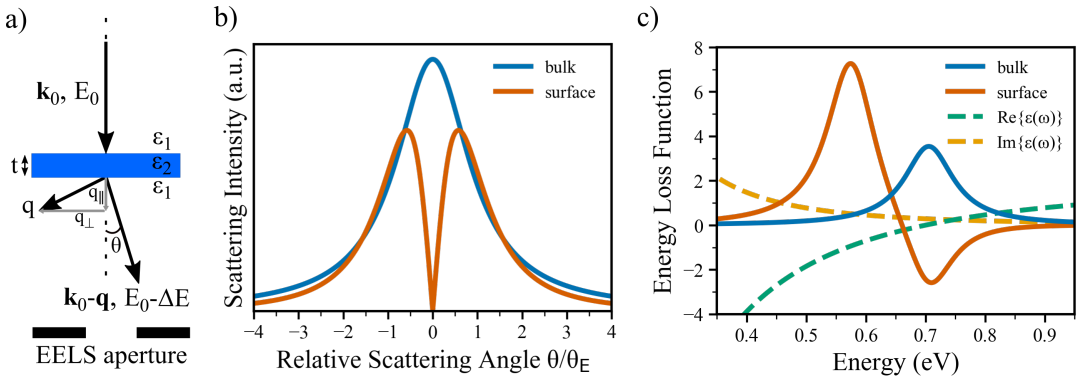

Figure 2.25: a) Momentum vector diagram of inelastic scattering (with exaggerated $\mathbf{q}$) at angle θ. b) Angular distribution of scattering within the bulk and at the surface relative to θ_E. The EELS aperture acceptance is typically $\sim$100 mrad $\gg \theta_E$ [78]. c) Bulk and surface loss functions after substitution of $\varepsilon(\Delta E)$ for a non-ideal Drude material ($\omega_p = 1$ eV, $\varepsilon_b = 2$ and $\gamma = 0.1$ eV). For low γ, the bulk resonance occurs at the $\mathrm{Re}\{\varepsilon(\omega)\}$ crossover.

Modifications to $P(\mathbf{q},\Delta E)$ must be made when considering the contributions from surfaces, radiation losses[6], relativity, and plural scattering, although the theory behind these are beyond the scope of this thesis. Nevertheless, a brief exploration of the surface effects can complement the concepts introduced thus far. At a single interface between a dielectric and semi-infinite metal, the possibility of a surface plasmon (SP) excitation is described in P_s,

$$P_s = \frac{1}{k_0}\left(\frac{q_e}{\pi\hbar v}\right)^2 Im\left(\frac{(\varepsilon_1-\varepsilon_2)^2}{\varepsilon_1^2\varepsilon_2}R(t)\right)\frac{2\theta}{(\theta^2+\theta_E^2)^2}, \tag{2.36}$$

where the factor of 2 takes into account SPs on both sides of the film. $R(t)$ is a thickness-dependent factor, and for sufficiently small t, it modifies Equation 2.36 as the SPs couple to split ω_{sp} into two frequencies. Evidently, the angular distribution of scattering (Figure 2.25b) is different from that of the bulk. Since $q = q_{\|}$ at $\theta = 0$, no SP vector is realized. A maximum scattering intensity is seen at $\theta = \theta_E/\sqrt{3}$, and further increases in θ show a decrease proportional to θ^{-3}.

By momentarily assuming that $q_\perp t \gg 1$, surface coupling can be ignored and the surface loss function becomes independent of thickness as,

$$Loss_{EELS} = Im\left(\frac{(\varepsilon_1-\varepsilon_2)^2}{\varepsilon_1\varepsilon_2(\varepsilon_1+\varepsilon_2)}\right). \tag{2.37}$$

[6]This includes damping from i) light emission (radiation scattering) and ii) a non-negligible particle size with respect to the incident E field (retardation effects).

The surface and bulk loss functions are compared in Figure 2.25c. For an ideal Drude film, the positive peak at $\varepsilon_1 = -\varepsilon_2$ corresponds to SP excitation at $E_{sp} = \hbar\omega_{sp} = \hbar\frac{\omega_p}{\sqrt{1+\varepsilon_1}}$, which red-shifts for non-ideal Drude films. The negative peak at $\varepsilon_2 = 0$ subtracts from P_b, becoming more significant for $P(\mathbf{q},\Delta E)$ as t decreases[7]. Raether [87] describes the bulk peak intensity decreasing by over $\sim$30% between 100 nm and 10 nm thick aluminum films. For thicknesses $t \sim q_{\perp}^{-1} = \frac{v}{\omega_p}$ or lower, the coupling between surfaces leads to the SP splitting into symmetric and anti-symmetric modes.

Simulating these interactions can be carried out with the Metal Nanoparticle Boundary Element (MNPBEM) MATLAB toolbox [89]. This software models the interaction of different excitations (e.g. plane wave or electric dipole) with particles of arbitrary size (usually nanometer-scale dimensions). The wave equation is solved for an unbounded region using an ad-hoc scalar potential that includes an unknown surface charge distribution as a function of distance along the boundaries. This term is calculated so that the boundary conditions from Equation 2.16 are fulfilled. Recall that these conditions utilize a complex $\varepsilon(\Delta E)$, so the toolbox needs to have this specified for each region (i.e. particle and environment). The bulk interaction is calculated using this $\varepsilon(\Delta E)$ and Equation 2.35, whereas for the surface, the particle boundary is discretized into a triangular mesh to obtain the total electric field (from the probe and surface charges) and scattering probability at the centroid of each element.

2.3.4 The High-Loss Region

The high energy region consists of peaks (i.e. ionization edges) related to electron excitations from below the valence band, involving core-level electrons. Although these transitions do not link directly to plasmons, the power comes from identifying the potential sources of free carriers that control the availability of such resonances. The excitation of core-level electrons into higher energy states or the continuum provides useful information on the elements and phases present, as well as the atomic bonding based on the shape and positions of peaks.

Since bulk inelastic scattering is inversely related to q-squared (Equation 2.34), the intensity of high energy transitions is much lower than for plasmon excitations. As a result, the signal-to-noise ratio (SNR) decreases with energy and the detection limit of the spectrometer becomes important. Additionally, the plasmon signal has a tail that extends to these high energies that, if multiple plasmons are excited (by one incident electron), may be intense enough to interfere with the core-loss ionization edges.

Samples with thicknesses below one MFP are essential to avoiding plural scatter-

[7] Also known in the literature as the *berzenung* effect

ing effects for both plasmon and core-loss excitations. Egerton [15] details a common method for estimating the thickness (relative to the inelastic MFP of the incident electron) which involves the ratio of the elastic signal intensity I_0 to the total signal intensity I_{total}. Assuming that each inelastic event is independent, the probability of n collisions follows Poisson statistics as,

$$P_n = \frac{I_n}{I_{total}} = \left(\frac{1}{n!}\right)\left(\frac{t}{\lambda}\right)^n e^{-t/\lambda}, \tag{2.38}$$

where t/λ is the average number of collisions. The ZLP intensity I_0 can be measured, and for $n = 0$ Equation 2.38 arranges into,

$$\frac{t}{\lambda} = ln\left(\frac{I_{total}}{I_0}\right). \tag{2.39}$$

Ideally $t/\lambda \leq 1$ so that there is one inelastic collision per incident electron. Larger values risk adding intensity to ionization edges, modifying their shape (through the convolution of the edge and plasmon tail at the CCD), or hiding them behind the background.

The true shape of an ionization edge arises from the density of unfilled states above the Fermi energy that a core electron can be promoted into. Recall the DOS for a metal or semiconductor from Figure 2.5, which is a simplification because the bonding environment introduces variations into the DOS as a function of energy. These variations correlate with the shape of the ionization edge, where the EELS intensity is proportional to the DOS above E_F for core-level inelastic transitions [78].

Of the few EELS studies on ITO, Morikawa et al. [90] use core-loss spectra to report qualitative observations of an increase in the $Sn_{4,5}$-edge intensity at grain boundaries. They relate this increase to the segregation of Sn away from the grain bulk. A portion of the high energy spectrum is given in Figure 2.26 for their c-ITO thin film. The 440-600 eV range highlights the locations of the In $M_{4,5}$-edge (443 eV), $Sn_{4,5}$-edge (485 eV), and oxygen K-edge (532 eV), the latter of which has a clear set of multiple peaks at higher energies from the local bonding with In and other oxygen atoms. Here, high energy resolution is essential for distinguishing these post-edge peaks from each other and the background noise.

2.3.5 Energy Resolution

The energy range of the initial electron beam can make separating energy loss events difficult, especially those close to the ZLP. A monochromator can aid with this by filtering the nonzero energy spread to keep a desired beam energy. TEMs may be equipped

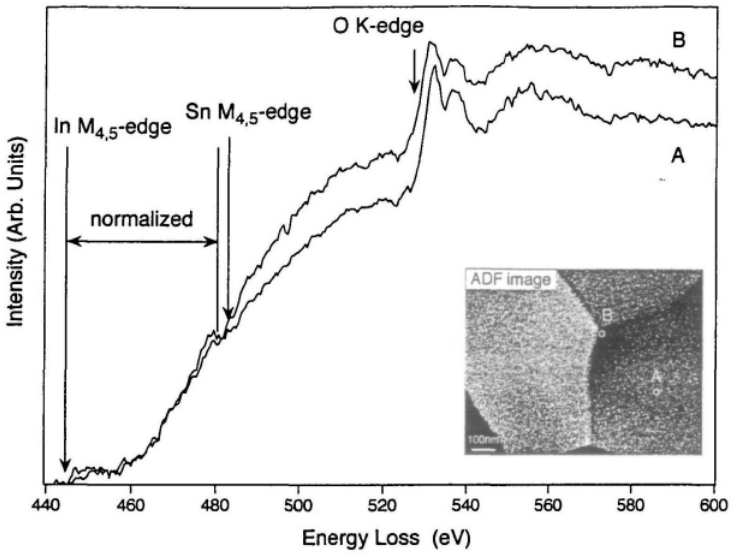

Figure 2.26: EELS spectra and ADF image of an ITO film annealed at 533 K in vacuum. To show contributions from In only, they normalized the spectra between 445 eV and 480 eV by the intensity of the In $M_{4,5}$-edge. Obtained from [90] by permission of Oxford University Press.

with this to improve energy resolutions of 100 meV down to 60 meV, and more recently 9 meV with the development of new designs. In addition to the monochromator, the Richardson-Lucy deconvolution tool has also been demonstrated to uncover hidden features in energy loss experiments and will be introduced here.

Figure 2.27a gives a layout of the gun in a monochromated TEM. The current and speed of electrons entering the monochromator can be controlled by the voltage potentials at the extractor, gun lens, and monochromator[8]. The addition of a monochromator after the gun also adds an entrance aperture and a removable energy-selecting aperture, the latter of which is placed at the C1 aperture position. A lens (accelerator) is used to focus the monochromator exit at this plane.

The working principle of the monochromator can be explained with a Wein filter, as illustrated in Figure 2.27b. After exiting the gun lens, electrons travel between two oppositely charged parallel metal plates at potential V within a uniform magnetic field B. Those entering the filter along the center axis with velocity $v = \frac{qV}{B}$ pass through undeflected because the electric and magnetic forces are equal and opposite. However, those exiting the gun lens can vary in velocity and distance from this axis. The voltage of each plate and the magnetic field are set so that the beams converge at the exit of the monochromator. This is also known as the monochromator excitation value. Higher excitation increases the dispersion, allowing the energy-selecting slit to further narrow

[8]More details on the different operating modes can be found in the FEI Titan monochromator manual.

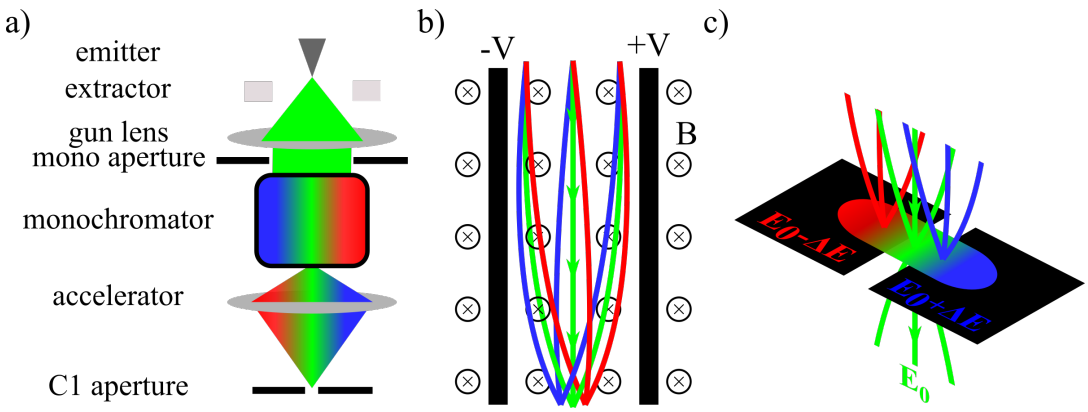

Figure 2.27: Simplified schematic of monochromator used in FEI Titan microscopes

the energy range of electrons entering the C1 lens. Figure 2.27c gives a general idea of how the exit aperture can filter electrons that differ in energy by ΔE. Of course, this is limited by the size of the aperture, as well as the stability of the beam position. Therefore, improvements in energy resolution come from reducing environmental effects (e.g. temperature gradients, mechanical vibrations, noise from the high voltage source) that destabilize the beam. One way includes using a spectrum acquisition time much shorter than the oscillation period of the 60 Hz ($\sim$17 ms) voltage supply [81]. Additionally, the *effective* energy resolution (the resolution obtained after the acquisition) can also be improved through the limited application of signal processing techniques.

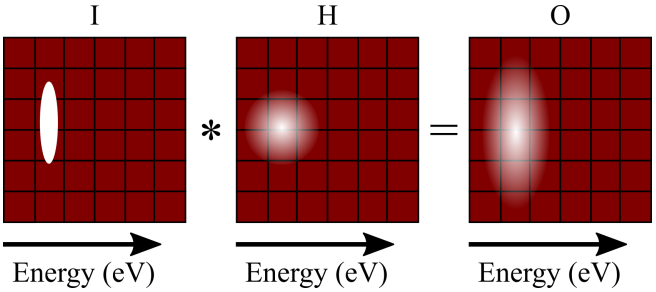

Figure 2.28: Pictured is a spectrometer CCD with a profile of incident photons originating from the beam hitting the scintillator. The spectrometer disperses energy in the horizontal direction, and any signal along the vertical is summed. The effect of the PSF is to broaden the ideal ZLP I over additional pixels to get O.

The Richardson-Lucy deconvolution algorithm based on the Bayesian probability theorem [91][9] can be applied to EELS spectra to improve the effective energy resolution. Bellido et al. [92] uses this post-acquisition approach to reduce the influence of the spectrometer, achieving an effective $\sim$10 meV resolution compared to $\sim$60 meV at the time of acquisition. In general, deconvolution procedures attempt to recover the

[9]Demonstrated by Kennett et al. on photoneutron experiments at McMaster University

true input, I from the output O of a signal processing system, blurred by the system's impulse response or transfer function, H. With EELS, the range of electron energies

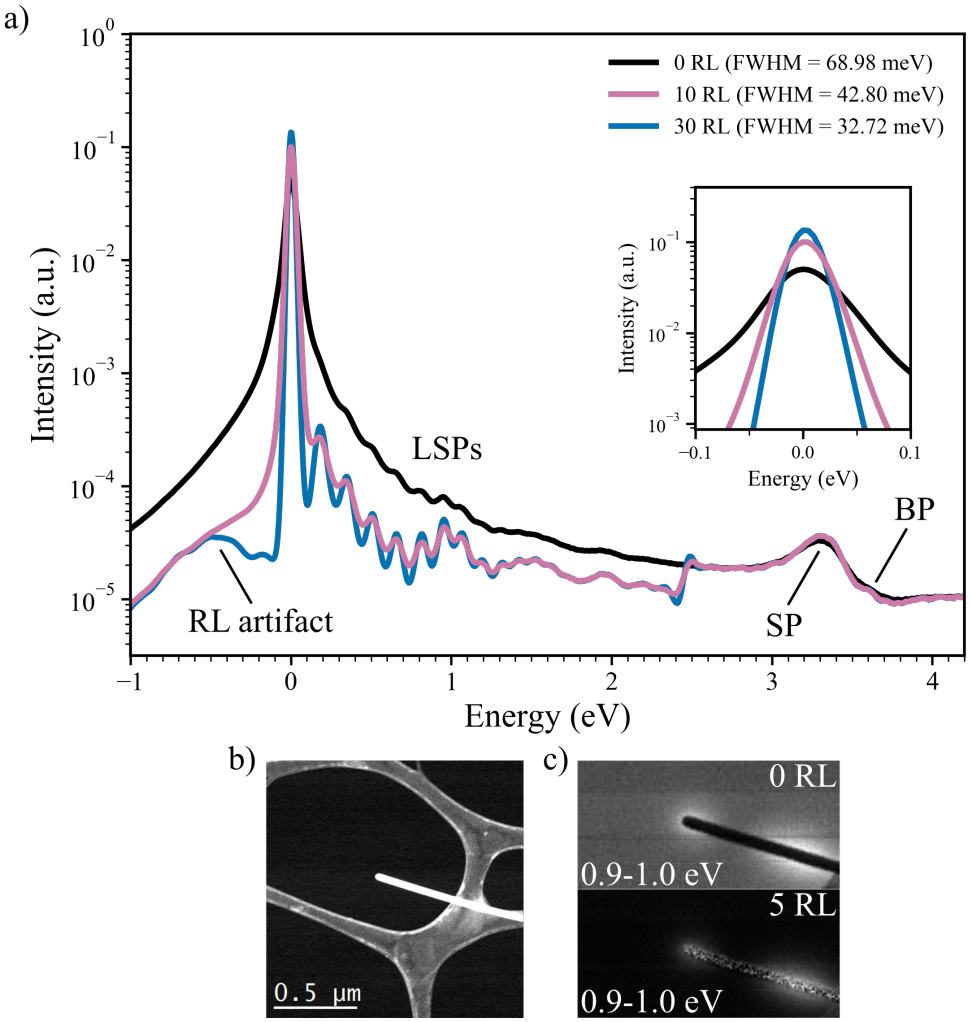

Figure 2.29: a) Raw and deconvoluted EELS spectra integrated over the nanowire. Each peak from 0.2 eV until the SP at 3.3 eV corresponds to an LSP. b) HAADF image of the Ag nanowire suspended over vacuum. c) SIs showing spectra at each pixel integrated between 0.9-1.0 eV. Raw data courtesy of Isobel Bicket on the Titan LB at 80 kV.

after the sample can be considered as I, the spectra displayed on the computer as O, and H can represent the beam spread and any aberrations caused by the spectrometer lenses. Figure 2.28a gives an idea of how a generic beam spreads over multiple energy channels (or CCD pixels) after being convolved with the spectrometer's impulse response (point spread function (PSF)). The probability $P(I_i)$ that an event, or photon, originating from the true input I, hits a pixel i on the CCD can be expressed using Bayes' theorem [93], as elaborated in the Appendix. The original input signal I_i can thus be estimated by

iteratively removing the contribution of the PSF. Figure 2.29a gives an example of the difference between spectra, averaged over a Ag nanowire supported above vacuum by a holey Cu grid. With a FWHM of $\sim$69 eV, the raw spectrum (normalized to its integral) displays some small peaks corresponding to the many LSP excitations, including an SP peak. With 30 additional iterations, the FWHM improves significantly (visualized with the inset plot) to about half of the original value, uncovering more LSPs and the bulk plasmon (BP). With enough iterations however, artifacts can also arise on either side of the ZLP, and can be exacerbated by a noisy spectrum. Although this sample has characteristics (i.e. very thin, no substrate) that lead to an excellent SNR, the RL procedure is known to amplify noise with each iteration [92]. These, along with the processing time, limit its use. Nevertheless, as long as the SNR is sufficient, the reduction in the ZLP tail over each pixel can even improve the SI contrast [92]. This is visible in Figure 2.29c after 5 iterations as the loss intensity spread of an individual plasmon (bright areas) is reduced.

Chapter 3

Experimental Methods and Simulations

Nanofabrication followed the steps developed by Bellido [92], which offers great control (50 nm resolution can be reasonably achieved) and flexibility of structure shapes and sizes. The fabrication of ITO nanostructures and thin films, as well as their cross-sections, are detailed here, along with the characterization setups for each sample. Three TEM samples T1, T5, and T8 refer to grids with ITO thicknesses of 30 nm, 50 nm, and 100 nm (these were the preset values entered to the sputtering machine), respectively. T8 is given to 100 nm ITO after rapid thermal annealing (RTA) and T6 is given to a separate grid of unannealed 100 nm thick ITO. Ellipsometry and TEM imaging of 50 nm and 100 nm cross sections revealed that their actual thicknesses were 32 nm and 71 nm, respectively. Therefore, the actual values will be used for the duration of this thesis. A cross-section of a 30 nm preset film was not fabricated.

3.1 Fabrication Overview

Circular, rectangular, and triangular nanostructures were prepared on Norcada TEM grids with nine 50 nm thick SiN windows. Starting off, each sample was cleaned of residual organic contaminants using a Gatan Solarus Advanced Plasma Cleaner with Ar, O_2, and Ne flow gasses at 50 W for 3 min. In a Class 10000 cleanroom, 3% 950 kg/mol polymethyl methacrylate (PMMA) in anisole solution was drop cast onto the TEM grid and spun at 6000 RPM for 90 s, then cured for 5 min at 175 °C. An optical microscope was used to check if the film was uniform across all the SiN windows. An example is shown in Figure 3.1a.

EBL, controlled by Nanometer Pattern Generation System (NPGS) software, was performed on a JEOL 7000F SEM with 10 kV beam voltage, 25 pA beam current, and 13 mm working distance. For each SiN window, five sets of arrays were patterned to

a) b)

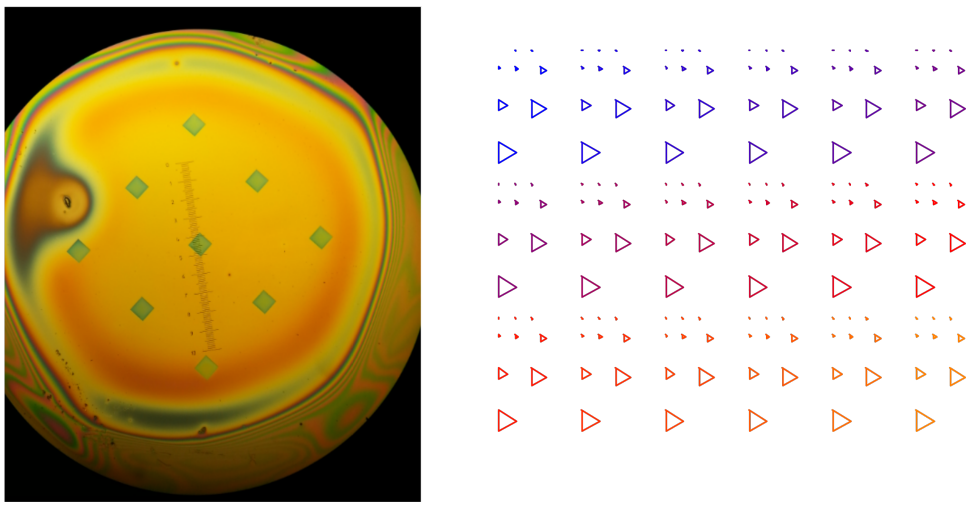

Figure 3.1: a) Example of PMMA droplet spun onto a TEM grid, encountering a dirt particle or bubble outside the membrane region. b) Array of custom triangle shapes for EBL, ranging from 50 nm to 1200 nm side lengths.

increase the chances of obtaining high quality nanostructures (uniform Z-contrast across the surface, no apparent damage, missing material, or contaminants within its vicinity). Figure 3.1b shows a schematic of such an array, color-coded to represent the range of increasing dose (500-700 $\mu C/cm^2$) from top left to bottom right. After exposure, the grid was dipped for 120 s into a developer solution containing a 1:3 ratio of methyl isobutyl ketone (MIBK) and isopropyl alcohol (IPA), followed by a quick rinse in IPA and dried with compressed N_2 gas.

RF sputtering took place in a Torr International Compact Research Coater CRC-600 system with an ITO target (90:10 wt% In_2O_3:SnO_2) from LTS Research Laboratories Inc. Prior to sample loading, both the target holder and casing were hand-cleaned with a steel wool brush to remove material from previous depositions (e.g. Au, Ag, Al, Cu, SiO_2, Mo, and Ti) made by other users. For a uniform deposition, the sample was placed halfway between the center and outer edge of the rotation stage, with a medium rotation speed setting of 4. The chamber was then left to pump down overnight to a pressure of $\sim$1x10^{-6} Torr.

The source power was set to 50 W and the RF plasma was ignited by setting the Ar flow to approximately 30-40 sccm to decrease the mean free path of particle collisions. The gas flow was then slowly brought down to 4 sccm to increase the deposition rate. Approximately 10 nm of ITO was sputtered (with the sample covered) to avoid depositing any surface contaminants or oxide growth from the target surface. The working

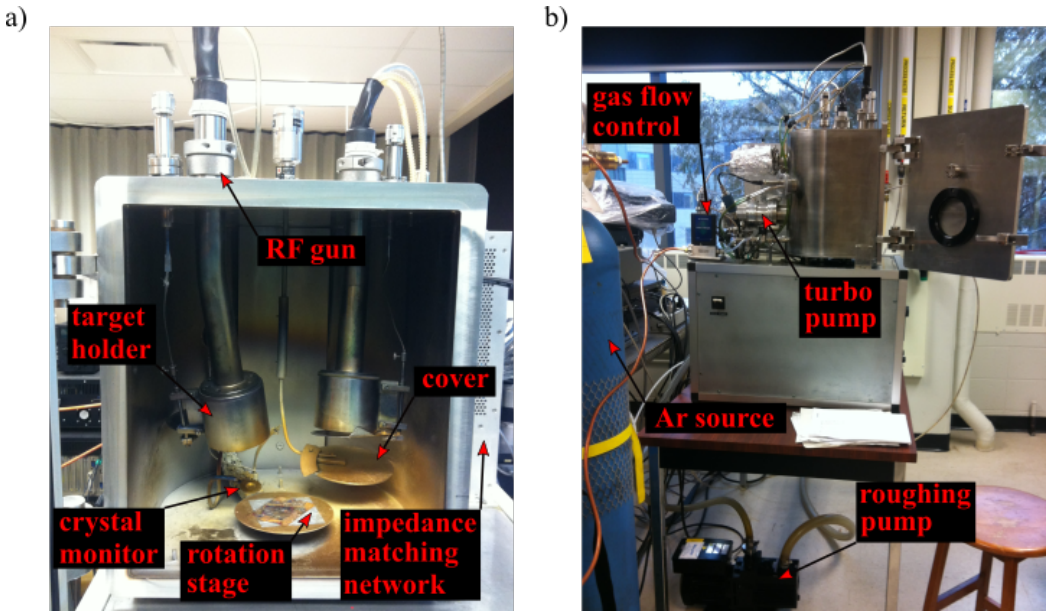

Figure 3.2: Images of sputtering machine used for ITO depositions.

pressure was $\sim$1x10^{-3} Torr. Presets for the control module included a Z factor[1] of 1, a density of 7.1, and either 30 nm, 50 nm, or 100 nm thickness. Finally, after the sample was uncovered, the deposition rate increased to between 0.8-1 Å/s and terminated once the preset thickness value was detected on the crystal monitor.

Samples that were annealed were individually placed in a solid carbon container, also known as a "boat", and covered with a carbon lid. A pair of thermocouples were used to measure the temperature as the power to the halogen lamps above the boat was increased. 700 sccm of N_2 gas was used to purge the sealed chamber for 15 s before raising the temperature in a series of steps to 400 °C, as illustrated in the Appendix. The thermocouple setpoints at 200 °C, 300 °C, 350 °C, 375 °C, were each reached at 10 s intervals, followed by 400 °C within 20 s. Then, the temperature was held at 400 °C for 60 s within the N_2 atmosphere. This was followed by a 5 min cool down at room temperature. The thermocouple reading over time is shown in the Appendix. Figure 3.3 outlines the complete process.

TEM BF and selected area diffraction imaging of each sample were carried out using a Philips CM12 microscope at 120 kV. By rotating the sample stage, the beam was aligned to a zone axis for samples T1 and T5, which were indexed afterwards using the Eje-z online applet[2].

In addition to the four TEM samples, 32 and 71 nm thick ITO films were made

[1] A vibrating quartz crystal measures the thickness deposited by using the Z factor to compensate for the differing acoustic impedance with that of quartz. A Z factor of 1 suggests equivalent properties.

[2] `http://www2.uca.es/dept/cmat_qinor/catalisis/tem-uca-server.htm`

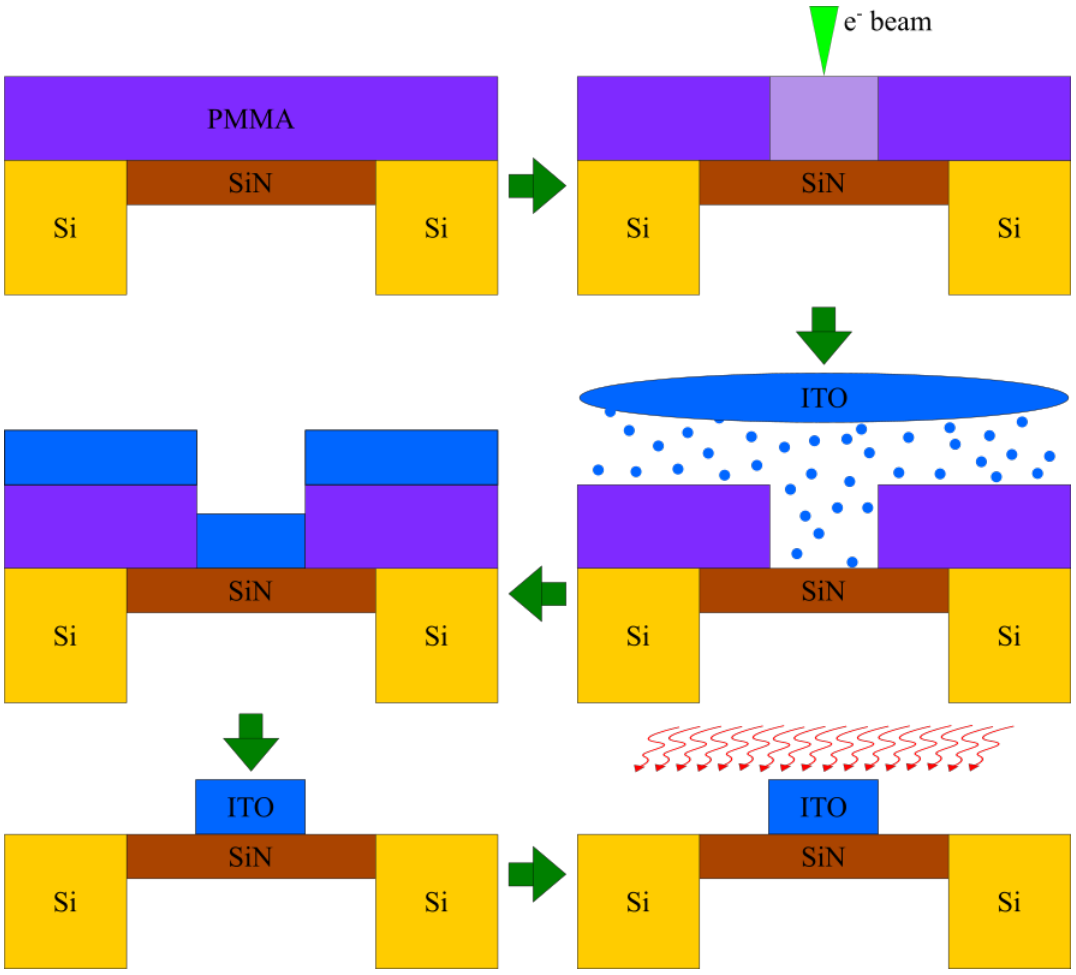

Figure 3.3: Process flow for fabricating ITO nanostructures on 50 nm thick SiN membrane windows. Spin coated PMMA is weakened in an EBL-defined pattern, and after it is removed the ITO can deposit over the mask. Removing the remaining PMMA isolates the pattern which can then be annealed.

separately on scribed Norcada Si wafer pieces with $\sim$10 mm^2 surface area and 50 nm thick SiN overlayer. Excluding the lithography, their preparation involved similar steps. To characterize them, resistivity and ellipsometry measurements were performed. Five resistivity measurements with the 4-point probe Van der Pauw method were averaged for the 71 nm thick ITO before and after RTA. The film was prepared on a wafer piece that had the sides covered in Kapton tape during the deposition. This was to ensure that no material could create a path of low resistance to the semi-conductive Si substrate. Similar to Figure 3.4a, the metallic probes were arranged across the sample. An ohmic contact was ensured by testing the resistance between probe and sample to be $\sim$100-200 Ω. Current-voltage plots were created using current values between 0.4 mA and 2.4 mA. More details on the experimental parameters can be found in the Appendix.

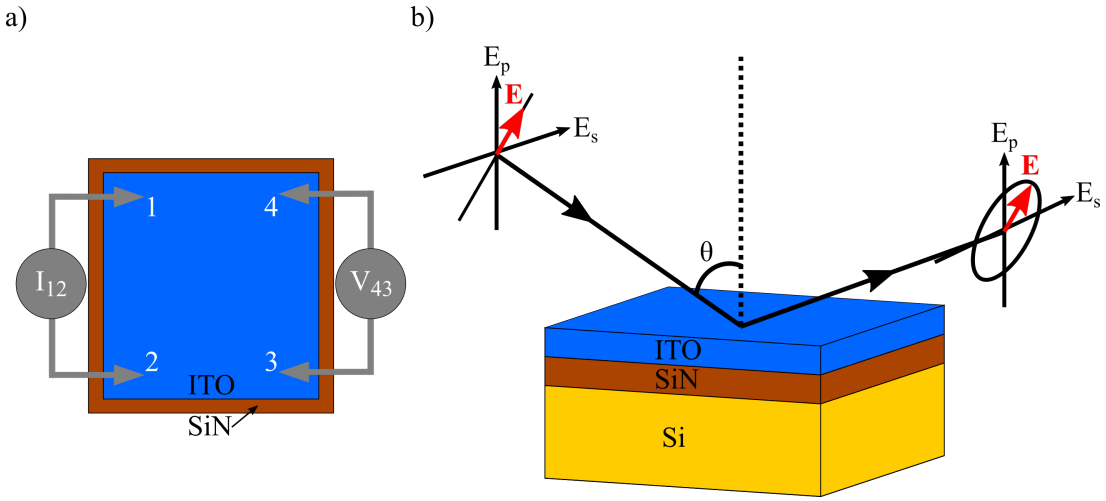

Figure 3.4: a) 4-point probe configuration where current I_{12} flows from probe 1 to 2 and the induced voltage V_{43} is measured across probes 4 and 3. b) General principle of ellipsometry which measures the change from linearly polarized light to elliptical with respect to the s- and p-plane (perpendicular and parallel to the plane of incidence, respectively). The software uses the reflected intensities and phase change to determine the optical constants of a 3-layer model (Si substrate, ~50 nm thick SiN film, and ITO film of unknown thickness).

3.2 EEL Simulations

The dielectric function of ITO was obtained for 32 nm (after RTA) and 71 nm (before and after RTA) thick ITO films using a UV-Vis Variable Angle Spectroscopy Ellipsometer (VASE) averaged over five angles of incidence between 55-75 °. CompleteEase v4.05 software was used to build three model layers (Figure 3.4b). This was achieved by first performing ellipsometry on a clean SiN/Si wafer piece and fitting the experimental spectra with a dispersion model of constants given in Table 3.1. The substrate

thickness (nm)	A	B	C	k amplitude
51.61	1.987	0.01	0	0

Table 3.1: Ellipsometry fit parameters for a SiN film over a Si substrate, described by a Cauchy dispersion model[4].

layer was described by a default set of optical constants for Si. This 2-layer model was then used to fit the experimental spectra from an ITO layer that was deposited on the SiN/Si sample. This was carried out using a Drude dispersion model between 700 nm (1.77 eV) and 1680 nm (0.74 eV). The scattering time $\tau_s = \gamma^{-1}$, ε_b, and $\mathrm{Re}\{\varepsilon(\omega)\}$ were used to calculate ω_p in Equation 2.10. The calculated ω_p was compared with literature,

and by using it in Equation 2.10 a Drude model $\varepsilon(\omega)$ was created that fit the experiment. The model was then used to extrapolate $\varepsilon(\omega)$ down to 12.4 μm (0.1 eV).

To simulate the plasmonic response of a finite structure, a 71 nm thick triangle of 1200 nm side lengths was discretized into a fine mesh (Figure 3.5[5]) using the MNPBEM toolbox (version 14) in MATLAB 2016a. The corners of the triangle were rounded to imitate the result of the non-zero beam spread of the EBL probe. While the dielectric environment was set to vacuum ($\varepsilon = 1$), the triangle was defined by the complex $\varepsilon(\omega)$ obtained with ellipsometry for the same film before and after RTA. Because each response follows a Drude model, the fit to lower energies from the near-IR ($\sim$0.7 eV) into the mid-IR ($\sim$0.1 eV) was justified for the EEL simulations. Here, the full set of Maxwell's equations were solved using the *bemret* solver between 0.1 eV and 0.9 eV. At probe energies of 60 kV and 80 kV, the beam width was set to 0.2 nm and, when exciting edge modes, the impact parameter was $\sim$2 nm.

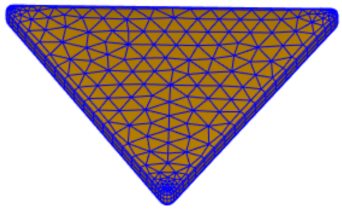

Figure 3.5: Example of a 71 nm thick structure created in the MNPBEM toolbox with a fine triangular mesh applied over its surface. Node densities are higher at the corners due to rounding.

3.3 Low-Loss EELS

Here the acquisition and post-processing conditions are outlined for low-loss EELS spectra taken on samples T8, T5, and T6 (T1 broke prior to EELS). A spectrum image (SI) was taken for each structure, as well as for isolated portions of SiN or vacuum (i.e. over a broken window, if there was one). The SiN or vacuum spectra were used as the PSF spectra for the post-acquisition Richardson-Lucy (RL) deconvolution. With each low-loss acquisition, an analysis to isolate plasmon peaks over different areas in the SI was performed using SpectrumImagingAnalysisPy Python software [94]. The analysis involved aligning, padding, deconvolving, and integrating. First, the ZLPs of each pixel in each SI were aligned to each other along the energy axis. Then, the spectra at each

[5]The author is grateful to Andrew Scullion for his smoothshape() MATLAB function which modifies the mesh by removing duplicate nodes and spacing them out more evenly to obtain smoother features.

pixel in the reference SI (PSF) were made symmetric about the ZLP by lengthening the dataset with zeros on either side. The RL algorithm [92] was then employed for varying iterations, depending on the SI. Deconvolved spectra from each pixel were integrated over selected areas, mainly the corners, sides, center, and entire surface area of each structure. To achieve a better SNR, some integrations was performed prior to deconvolution.

T8 was imaged using a monochromated FEI Themis[6] in STEM mode at 60 kV. The spectrometer dispersion was set to 5 meV/channel and acquisitions for each pixel took 5 ms. The energy resolution, measured by the full width at half maximum (FWHM) of the ZLP, was $\sim$32 meV when taken over the SiN grid window. The post-acquisition deconvolution involved either 1 RL iteration over the ITO, improving the FWHM to $\sim$29 meV, or 11 RL iterations over the SiN to obtain $\sim$19 meV.

T5 was imaged using a monochromated FEI Titan LB (low-base configuration) in STEM mode at 80 kV with 5 meV/channel dispersion. EELS spectra were acquired over four equilateral triangles of different EBL dosage. The FWHM over the SiN grid window was $\sim$65 meV using a 10 mm C2 aperture and 1 mm Tridiem GIF spectrometer aperture. The monochromator was set to a 3000 V potential and 1.8 excitation and between 7 and 20 RL iterations were used to improve the effective energy resolution to $\sim$42 meV.

T6 was also imaged using a monochromated FEI Titan LB in STEM mode at 80 kV with 5 meV/channel dispersion. The process involved imaging three triangles of the same EBL dosage, taking the grid out, performing an RTA, inserting the annealed grid back into the Titan, and acquiring spectra over the same three structures. The FWHM was $\sim$65 meV over the SiN using a 10 mm C2 aperture and 1 mm Tridiem GIF spectrometer aperture. The monochromator was set to an 800 V potential and 1.8 excitation. Over the ITO, 10 RL iterations improved the FWHM to $\sim$36 meV, while over the SiN, 30 RL iterations improved it to $\sim$27 meV.

3.4 Preparation of Cross-Section

Three samples were made to visualize the cross-section of annealed ITO using a Zeiss FIB-SEM at 30 kV. A 71 nm thick thin film, and triangles of 71 nm and 32 nm thicknesses were fabricated onto separate scribed SiN/Si wafer pieces. These were prepared using the same procedure outlined above for the TEM grids. Images of the film (Figure 3.6) and three equal-sized ($\sim$1200 nm side lengths) 71 nm thick triangles (Figure 3.7) are given.

[6] At the FEI Company in The Netherlands by Sorin Lazar

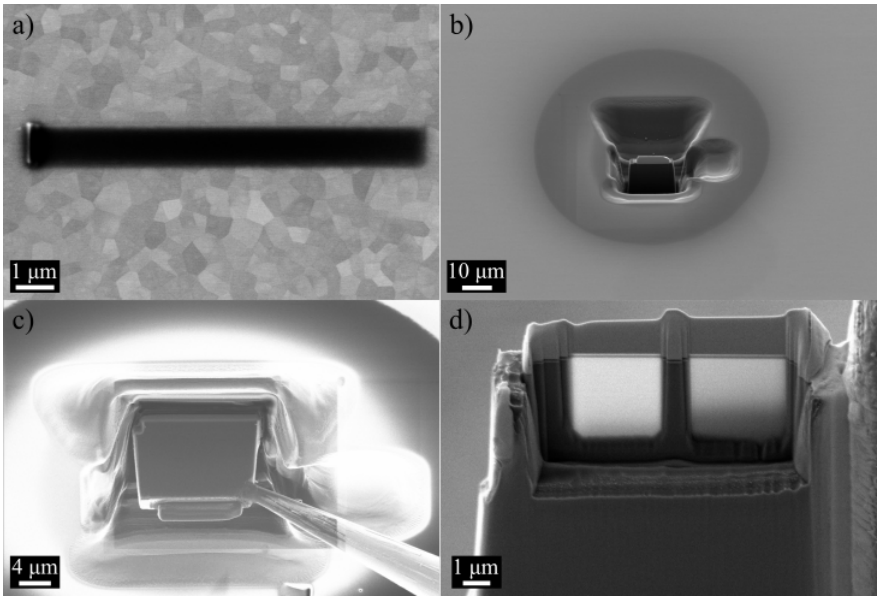

Figure 3.6: Steps in the lamella sample preparation, showing a) the initial tungsten deposition, b) the ion-milled trench, and c) the transfer to a Cu grid. Two electron transparent windows were thinned, as seen by the bright sections in d).

Preparation of the film section is outlined here, which was also followed for the other two samples (71 nm and 32 nm thick triangles). After depositing a thin layer of carbon using a Gatan 682 PECS[7], the sample was placed in the SEM and rotated 54° to align with the ion column. Tungsten was deposited over the desired area (Figure 3.6a) as a mask for protection against the ion beam. The Ga ion beam then milled away material on either side of this mask, well into the Si substrate (Figure 3.6b). The manipulator probe was connected to the mask through tungsten deposition (Figure 3.6c), and the lamella was cut loose by the ion beam. The probe transferred the lamella to a Cu TEM grid by tungsten deposition. Finally, the ion beam was used to thin the sample even further (Figure 3.6d) for electron beam transparency within the TEM.

3.5 Core-Loss EELS

An FEI Titan HB (high-base configuration) at 200 kV in STEM mode was used to obtain high energy (>200 eV) EELS spectra. Before loading, the samples were plasma cleaned for 3 min at 50 W. With the help of the diffraction pattern, each of the three sectioned samples were aligned to the zone axis of a single ITO grain by tilting the stage. The thickness, relative to the inelastic mean free path of electrons ($\frac{t}{\lambda}$), was calculated using Digital Micrograph software to be $\sim$1, suggesting a sufficiently thin sample.

[7]Precision Etching and Coating System

High resolution imaging and EELS were carried out over the entire ITO cross-section, including substrate and surface interfaces. Energy ranges were determined based on the known major core-level excitations of In (delayed from 443 eV), oxygen (532 eV), Sn (delayed from 485 eV), Ga (delayed from 1115 eV and 1142 eV), and nitrogen (401 eV). SIs for the analysis of composition and elemental distribution were acquired using a Quantum GIF spectrometer and a ZLP FWHM of $\sim$1 eV without monochromation.

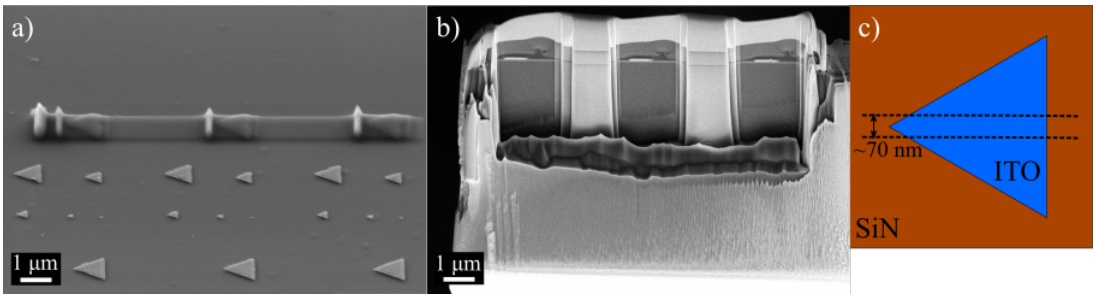

Figure 3.7: a) Tungsten deposition on three 1200 nm long triangles and b) final electron transparent lamella with each triangle visible as an embedded white rod. The section along the triangle center is shown in c), with the width (lamella thickness) approximated by the FIB operator.

Chapter 4

Results and Discussion

In this chapter, low energy simulated and experimental plasmon resonances observed in ITO nanostructures are presented along with the characterization of thin films. The effects of annealing and ITO thickness on both the low- and high-loss regions were explored and will be discussed. As mentioned previously, the literature on ITO bulk, thin film, and nanoparticle properties by optical characterization is extensive. To this date, a high energy resolution EELS study on ITO plasmons has not been achieved. Both an FEI Themis at 60 kV and an FEI Titan at 80 kV were used with their respective monochromators to visualize multiple LSPs, the bulk plasmon (BP), as well as a substrate phonon resonance. An FEI Titan at 200 kV was also used to gain insight into higher energy interactions.

4.1 Fabricated Structures

Bright field images of fabricated nanostructures are presented in Figure 4.1, with their respective diffraction patterns shown below each image. Differences are observed between the as-deposited T6 (Figure 4.1a) and annealed T8 (Figure 4.1b) samples. Tiny crystallites in Figure 4.1a may be viewed as the dark and light dots (with contrast arising from diffraction effects) within an amorphous matrix. The bright ring in the diffraction pattern may be evidence of such crystallites. A clear grain structure is shown post-RTA in Figure 4.1b, exhibiting a diffraction pattern similar to that of a powder (see Appendix). The width of the beam is fairly large relative to the structure, encompassing many grains which may be why the pattern appears random.

T5 is represented in Figures 4.1c and 4.1g, with grain sizes appearing to be much larger than the thicker structure. Tilting the sample revealed the [011] zone axis of one of the grains. The major $\langle 222 \rangle$ and $\langle 400 \rangle$ families of reflections agree with those found

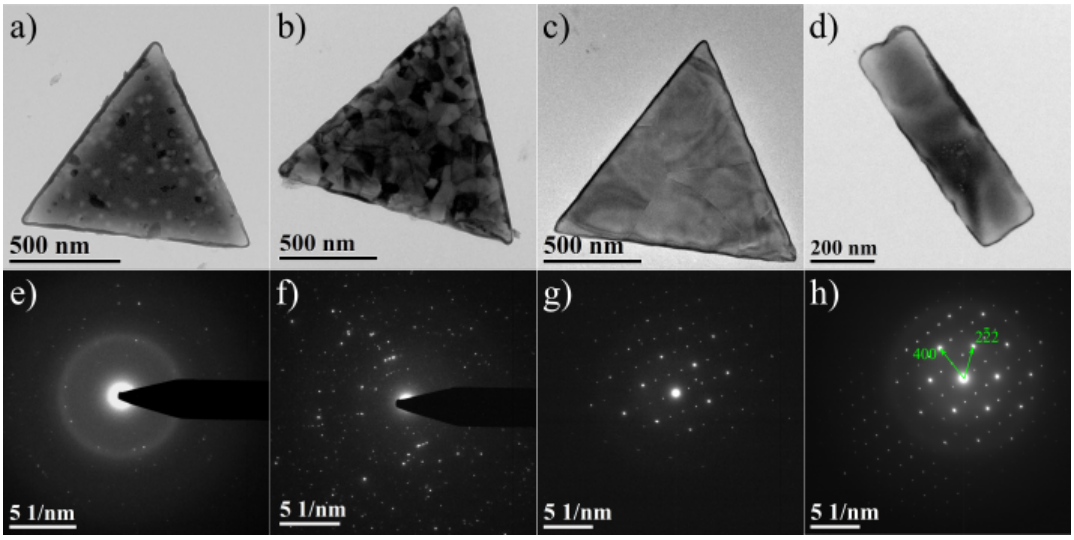

Figure 4.1: Bright field (a-d) and their respective diffraction (e-f) images of samples T6, T8, T5, and T1, taken on the CM12 TEM.

for thin films using X-ray diffraction [65]. Contrast across the structure may be related to diffraction effects caused by various grain orientations and differing amounts of lattice strain. Maybe more pronounced is this contrast in Figure 4.1d (sample T1), with the addition of some spherical features located in the dark region of the rod. Whether this is a type of dislocation, metal agglomeration, or surface roughness is unclear. Together with Figure 4.1h, the structure appears to be single crystalline over the amorphous SiN_x. As a result, the evolution of *a*-ITO to *c*-ITO, as well as the grain size dependence on thickness, can be inferred from Figures 4.1a-h. Island growth may produce the *a*-ITO phase containing tiny crystallites that grow with the RTA. Thinner films may have fewer crystallites and thus witness more lateral growth, leading to larger grains. These observations seem to agree with the models proposed by Sun et al. [46] and Paine et al. [48] (Figures 2.13 and 2.12).

FIB cross-sections of similar triangles to those in Figure 4.1 are laid out in Figure 4.2 to better understand the air/ITO and ITO/SiN interfaces and their influence on electrical properties (and plasmon characteristics). Both Figures 4.2a and 4.2d reveal that the fabrication process is imperfect. The ends of the cross-sections decrease in height and form into a moustache-like shape. A shadowing effect may have occurred during the deposition, caused by the height of the PMMA walls, and subsequent build-up of material right at the wall boundary. Ways to reduce this effect may include spinning a thinner PMMA layer (although not thinner than the deposited material), however it may not be a complete remedy. A bubble-like protrusion is also apparent in Figure 4.2a. The direct cause may arise from contamination either within the sputtering chamber or

PMMA left over from the mask development. The relatively lower density of this bubble could allow for further milling of the substrate, and therefore the dark line observed to extend from it.

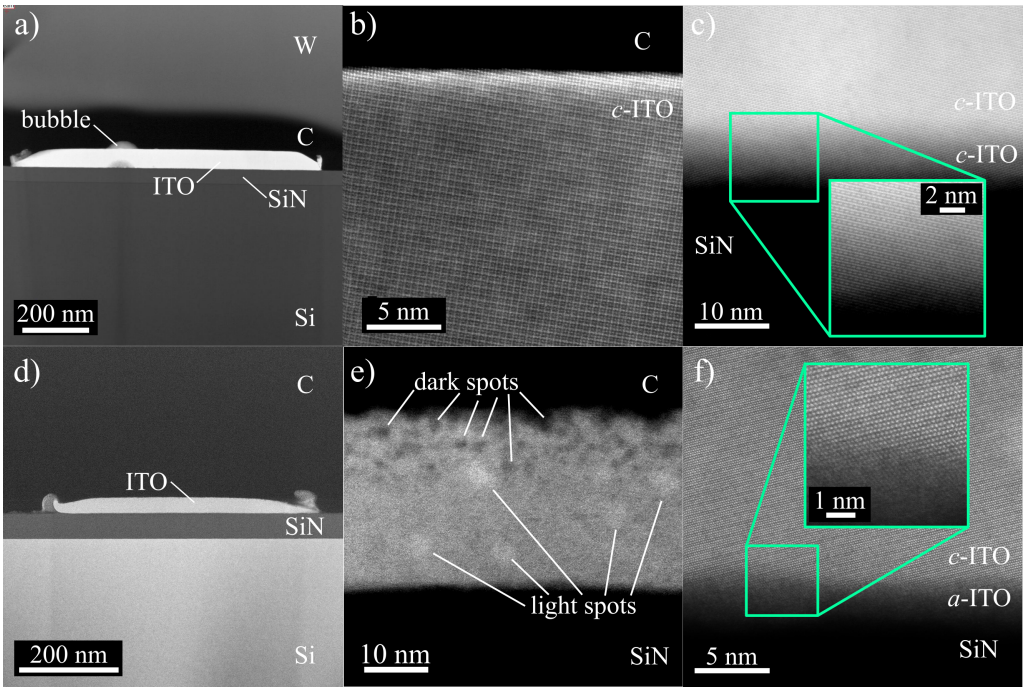

Figure 4.2: (a-c) ADF cross-sections of 71 nm ITO. In b), the surface of a continuous 71 nm thick film is presented instead of a lithographically fabricated nanostructure. c) shows the interface of a 1200 nm long triangle with SiN. 32 nm thick cross-sections of d) a 600 nm long triangle (HAADF) and (e-f) 1200 nm long triangle (ADF).

The surfaces, or carbon/ITO interfaces, of Figures 4.2b and 4.2e provide contrasting information about the thickness-dependent structure. Excluding the random assortment of intensities (attributed to carbon contamination), the 71 nm thick continuous film cross-section in 4.2b is uniform, crystalline, and terminates at the surface with a bright band (possibly from diffraction contrast as the crystal structure terminates). The 32 nm thick nanostructure cross-section (Figure 4.2e) exhibits clear variations in intensity across its surface. Dark spots can be seen along the top half of the ITO, while bright spots appear more within the bulk. Whether the spots and the surface roughness are linked is unclear. Possible FIB milling effects could be the source, such as ejecting material or Ga atoms collecting within the ITO, although EELS spectra (within the 950-1450 eV range) taken over these spots did not show peaks corresponding to Ga L_2- and L_3-edges. The light spots within the bulk are reminiscent of In particles embedded within an In_2O_3 matrix as imaged by Albrecht et al. [60]. They use high-resolution TEM to look at crystalline In nanoparticles and propose that their formation arises from the precipitation of oxygen vacancies. However, since $V_O^{\bullet\bullet}$ contribute two free elec-

trons to the CB, the resulting 2+ charge state should not allow for any clustering due to Coulomb repulsion. The reasoning that Albrecht et al. give is that these vacancy states are actually deep donor states, requiring large ionization energies >200 meV, and that hydrogen interstitials $H_i^{\bullet}$ are mainly responsible for the conduction in In_2O_3. At high temperatures (i.e. when annealing), two main effects occur. First, In_2O_3 decomposes and, if annealed in a reducing atmosphere, $V_O^{\bullet\bullet}$ concentrations increase as the material loses oxygen. Second, the extra energy promotes the deep state electrons into the CB, resulting in charged V_O^{2+} defects. After cooling, the freed electrons may become localized once again, and the ITO is supersaturated with neutral $V_O^{\bullet\bullet}$, forming In metal clusters that leave behind empty voids. This description could be used justify the appearance of these dark and light spots in Figure 4.2e, corresponding to vacancies and In, respectively. The fact that the contrast only appears near the surface could be interpreted by oxygen closer to the surface more likely to diffuse out of the film. Unfortunately the question of why this effect is more prominent for the thinner ITO still remains. Differences in the heating and cooling rates between 32 nm and 71 nm thick ITO might also be need to be considered, since Albrecht et al. mention that their observations occur for rapidly cooled ITO.

Figures 4.2c and 4.2f provide magnified images of the interfacial area between ITO and SiN. The decrease in intensity of ITO towards the substrate may arise because a rough SiN surface was imaged, or the beam was not completely parallel with the interface. What is notable are the differences between the two images. Figure 4.2c shows lattice planes within this area of reduced intensity, whereas the planes in Figure 4.2f stop abruptly before this area, which may be an *a*-ITO layer connecting the grain and substrate. Why this is not seen in the thicker ITO is unclear, and whether the two interfaces would have an appreciable impact on the electrical conduction of the bulk could be further explored. Cleary et al. [68] suggest that the carrier density N is sensitive to the thickness of ITO films due to interfacial defects that act as carrier traps and inhibit mobility. Going further, by performing ellipsometry measurements for (what thicknesses) ITO deposited on heated crystalline Si substrates, they propose a 14 nm thick "electrical dead layer" existing at the substrate interface for any thickness of ITO, which may correspond to the *a*-ITO in Figure 4.2f.

4.2 The Plasmonic Response of ITO

4.2.1 Visualizing LSPs

Fits to the ellipsometry data are displayed in Figure 4.3 for 71 nm thick ITO films before (71-as) and after (71-RTA) RTA, as well as a 32 nm film after annealing (32-RTA). Evidently, each response closely follows a Drude model between 700-1680 nm (0.74-1.77 eV), and the parameters for each fit are listed in Table 4.1. They were used to locate the crossing of $\mathrm{Re}\{\varepsilon(\omega)\}$ from negative to positive, also known as $\omega_c = \sqrt{\frac{\omega_p^2}{\varepsilon_\infty} - \gamma^2}$, or the *reduced* ω_p, when taking into account the screening by bound charges, so that the unscreened ω_p could be calculated using Equation 2.10. Energies corresponding to plasma frequencies are reported between 0.65 eV [95] and 1.86 eV [96] for thin films, although a greater range is possible [97]. The energies E_c at which $\varepsilon(\omega_c) = 0$ for 71-as, 71-RTA, and 32-RTA were determined to be 0.6351 eV, 0.7576 eV, and 0.7162 eV, respectively.

film	thickness (nm)	ε_∞	γ (eV)	$\rho(x10^{-4})\Omega$cm	MSE	E_p (eV)	E_c (eV)
71-as	69.15	4.173	0.1665	6.875	3.8	1.341	0.6351
71-RTA	71.23	3.871	0.1461	4.712	5.5	1.518	0.7576
32-RTA	37.98	3.870	0.1348	4.871	2.9	1.434	0.7162

Table 4.1: Fitting parameters for $\varepsilon(\omega)$ between 0.738 eV and 1.77 eV from ellipsometry measurements over three films. 32-RTA was fit with a thickness 6 nm greater than that measured in the cross-section. This may be because the fit does not take into account surface roughness and assumed that the optical properties are constant throughout the film thickness.

Already it can be seen that annealing increases E_c. 4-point probe measurements show that the sheet carrier density N increases from $3.7\pm0.1\text{x}10^{15}\text{cm}^{-2}$ to $8.1\pm0.8\text{x}10^{15}\text{cm}^{-2}$ and sheet resistance R_s cuts in half, from 109.5 ± 0.2 Ω/sq to 55.9 ± 2.3 Ω/sq. These changes are greater than those obtained by ellipsometry, possibly due to ionized impurity scattering (IIS) not being taken into account in the calculations carried out by the 4-point probe system. The sample was also not perfectly square, which is better for Van der Pauw configurations. Nevertheless, the increase in E_c can be attributed to the increase in N and decrease in ε_∞, along with a small contribution from γ. The zero crossing for the 32 nm thick film occurs lower in energy than the 71 nm post-RTA film, supporting observations in the literature of decreasing E_p and N for decreasing thickness [65] [68] [98]. Furthermore, ε_∞ decreases post-RTA, which also contributes to the reduction of E_p. The $\mathrm{Im}\{\varepsilon(\omega)\}$ for each film is relatively the same, with the 71 nm

post-RTA component scaling with the ω_p^2 (Equation 2.10). By using these fits, $\varepsilon(\omega)$ is extrapolated down to 0.1 eV and used as input for EEL simulations.

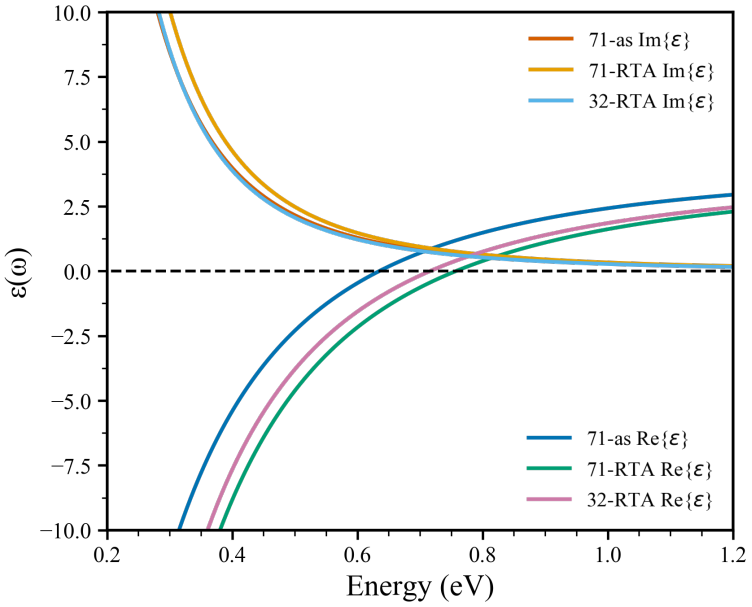

Figure 4.3: Fits to ellipsometry data for ITO films of 32 (annealed) and 71 nm thickness before (71-as) and after (71-RTA, 32-RTA) annealing.

With the MNPBEM toolbox, the probability of 60 kV electrons losing energy to a 71 nm thick, 1200 nm long equilateral triangle is plotted in Figure 4.4a at four different probe locations. Solid curves represent losses induced by surface charges only, with peaks corresponding to LSPs. The broken curves only consider bulk losses according to the bulk energy loss function (Equation 2.35). This BEM simulation reveals that the BP resonance occurs at ∼770.0 meV. Recall from Section 2.3.3 that when $\mathrm{Im}\{\varepsilon(\omega)\}$ is low, the crossover energy $E_c = \hbar\omega_c$ of $\mathrm{Re}\{\varepsilon(\omega)\}$ corresponds to a BP excitation condition. The value obtained from the BEM simulation thus agrees well with the E_c from ellipsometry. Thus, this thesis will use E_c to represent both the BP energy and the zero crossing of $\mathrm{Re}\{\varepsilon(\omega)\}$ since they should be approximately equal for ITO. The EEL maps in Figure 4.4b display the surface loss probability as a function of probe position over the triangle.

LSP resonance energies reach well into the mid-IR range, down to 235.6 meV. These peaks depend on the dielectric environment and geometry of the nanostructure. The beam can induce two kinds of resonances - edge and cavity modes. Edge modes occur along the particle side boundaries, where the electric field intensity follows a sinusoidal profile confined by the triangle corners. The lowest energy resonance at 235.6 meV consists of opposite charges on either end of an edge, leading to high EEL intensity at the

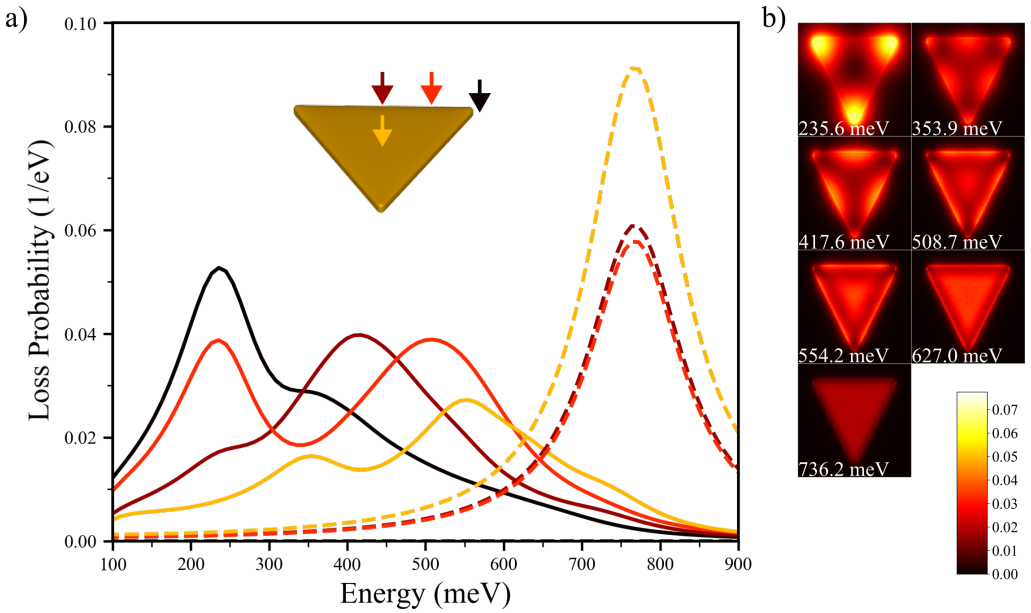

Figure 4.4: BEM simulation of EEL probabilities. Solid and dashed curves represent losses related to surface and bulk charges, respectively. With the exception of the center, the impact parameter of each probe is 2 nm from the nanoprism edge.

corners and low intensity at the antinode. Higher energy modes exhibit more antinodes along the edge with wavenumber according to Equation 2.20. Such resonances are spatially mapped out for 353.9 meV, 417.6 eV, and 508.7 meV. A second order edge mode can be excited at either 353.9 meV or 417.6 meV, the latter of which is more likely when probing the center of the triangle edge. The third and highest order edge mode occurs at 508.7 meV when probed 1/4 distance from the corner. Similarly, cavity modes appear over and are constrained by the surface center. Probing the triangle center excites a first order cavity mode at 554.2 meV, and similar to aluminum metal triangle EELS maps from Campos et al. [99] and Keast et al. [100], a higher order may be observed at 627.0 meV. It is unclear whether the small bump at 736.2 meV is physically significant. Unlike with the edges, the cavity antinodes are not visible, possibly due to the delocalization of each mode or the mesh discretization being too large. With a finer mesh and greater computing memory, additional LSP modes of higher energy could potentially be resolved. Simulations for both 60 kV and 80 kV excitations show peaks equivalent in energy but different in loss probability intensity. The lower energy beam increases the probability of both surface and bulk losses, as per Equations 2.34 and 2.36.

Figure 4.5a presents experimental EELS spectra integrated over areas of the HAADF image of annealed ITO (Figure 4.5b). Intensity variations along the triangle edges are apparent in the HAADF image due to the PMMA shadowing and uneven liftoff after deposition. The low-loss region of the raw EELS spectra did not exhibit any imme-

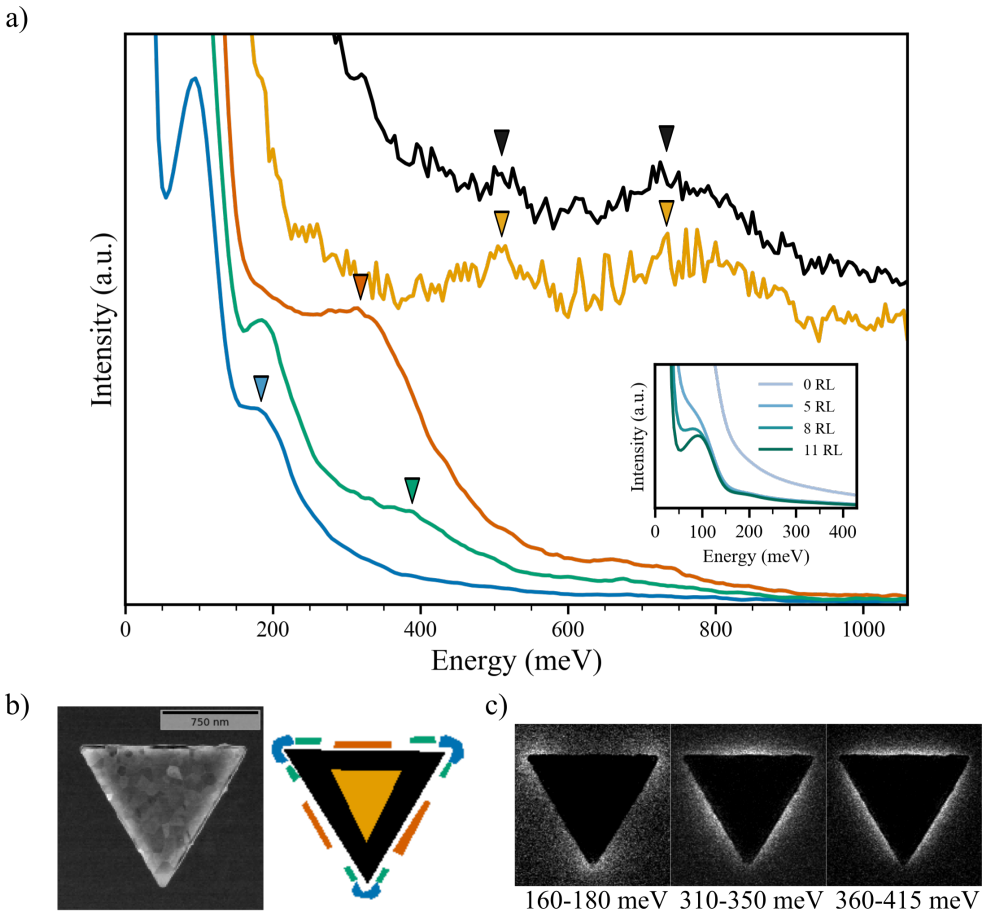

Figure 4.5: a) Experimental spectra acquired by Sorin Lazar using a Titan Themis at the FEI Company revealing the first three dipolar, cavity, and bulk resonances, including a substrate bulk phonon at ∼110 meV. b) HAADF-STEM image and c) experimental EELS maps of the first three dipolar SP modes.

diate features. However, after one RL iteration a bulk plasmon at 730±29 meV and cavity mode at 500±29 meV were distinguishable by integrating over the entire structure (black) and only the center (yellow). The bulk resonance, although quite broad and noisy from the relatively low beam current and thick specimen, seems to agree with the BEM simulated bulk peak at ∼770 meV. Possible surface oxidation from fabrication and storage may account for the difference between the triangle and continuous film. After integrating outside the triangle corners (blue), edge centers (orange), and between (green), 11 RL iterations revealed LSP peaks at 170±19 meV, 320±19 meV, and 380±19 meV in Figure 4.5a. The intensities of these spectra were offset from the others for a clearer illustration of peaks. EELS maps integrated over a few tens of meV (Figure 4.5c) show that the peaks at 170 meV, 320 meV, and 380 meV correspond to first, second, and third order edge modes, respectively. An additional bulk phonon peak at ∼110 meV from the SiN substrate was identified (agreeing with that found by Raman spectroscopy [101] and ellipsometry [102] for Si_3N_4) by integrating away from the structure and improving the effective energy resolution to 19 meV after 11 RL iterations (4.5a inset). Spatial maps of the SiN bulk phonon, ITO bulk plasmon and 500 meV cavity mode are not given because of the low SNR that impairs the contrast.

The simulated and experimental spectra are in agreement with the general evolution of LSP modes, but still do exhibit some differences. The experiment shows peaks that are red-shifted with respect to simulation. The dielectric function of the SiN and a mesh discretization that accounts for the film/substrate discontinuity would be needed for a proper model. Furthermore, the fabricated structure is tapered or curled at the ends (Figure 4.2a) which changes the boundaries seen by the plasmons. Another difference involves the small simulated peak at 353.9 meV which is not seen in the experiment. Nelayah et al. display peaks of similar simulated intensity between major LSP peaks [81]. They do not however expand on their existence, and do not observe them in their experimental EELS either. Their appearance may be unlikely because the probe is not incident on the edge.

The spatial and spectral mapping of multiple LSPs and a bulk resonance in ITO have been demonstrated using monochromated EELS and the necessity of post-acquisition deconvolution. These results support the Drude characteristics often cited in the literature through optical techniques. As a potential material for plasmonics devices operating in the IR to mid-IR, Figure 4.5 verifies its low energy response and proximity to the phononic region. The variety in its plasmonic properties however is not so apparent with a single demonstration, and will now be presented in the next two sections.

4.2.2 Effect of Annealing

Control of the dielectric environment and post-deposition temperature is essential to engineering high quality deposited films for many applications. EELS can expose modifications of $\varepsilon(\omega)$ resulting from changes in N, ε_∞, or γ. These can be interpreted to better understand how ITO evolves with temperature at the nanoscale, allowing the comparison of its plasmonic properties with other materials.

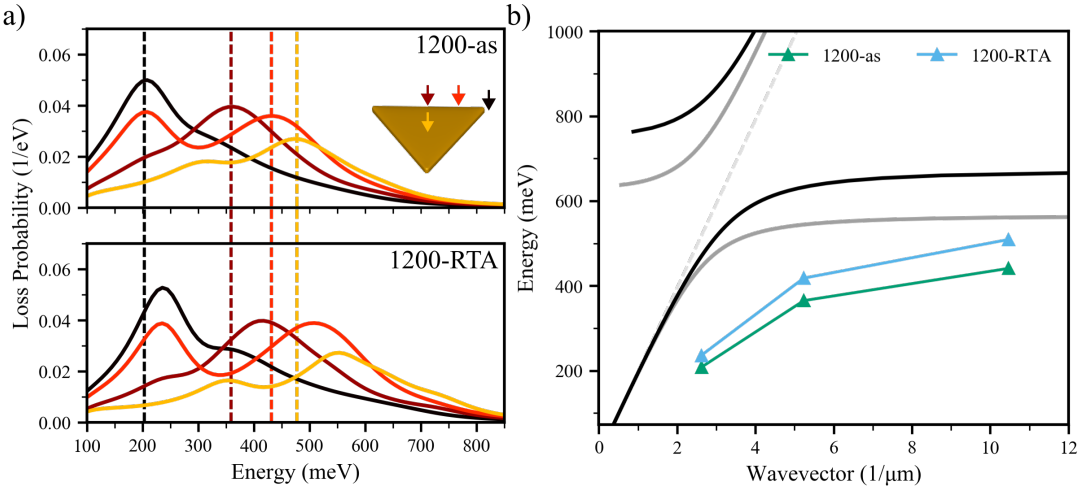

Figure 4.6: a) Simulated EEL results for before (top) and after (bottom) annealing using $\varepsilon(\omega)$ obtained from ellipsometry for continuous films (71-as and 71-RTA). b) Dispersion relations of a triangle (with $\varepsilon(\omega)$ for a film) with 1200 nm long sides before (1200-as) and after (1200-RTA) annealing, consisting of the first three edge modes. These are plotted against the dispersion of a continuous ITO film interface before (light) and after (dark) annealing, as well as the light line in vacuum (dotted).

By recalling Equation 2.8 for ω_p and its relation to N, ε_∞, and mobility μ, this work attempts to see a shift within the low-loss EELS region before and after RTA. Because probing $\varepsilon(\omega)$ of a material is invariant to the method of excitation (longitudinal or transverse) [88], a shift in E_c viewed in EELS could potentially be correlated with the shift obtained from ellipsometry on a thin film.

Simulations to demonstrate this effect on the LSPs and BP are pictured in Figure 4.6a for a 71 nm thick triangle. Ellipsometry fits before and after RTA for thin films are used as input, resulting in a noticeable shift to higher LSP resonance energies for each mode when the film is annealed, although not by the same proportion. This may be explained by the change in plasmon dispersion [103], as plotted in Figure 4.6b and compared to the dispersion for SPPs at a continuous interface (light and dark curves). Along with the increase in $E_c = \hbar\omega_c$ at the long wavelength limit, $E_{sp} = \hbar\omega_{sp}$ at the small wavelength limit also increases. A greater range of LSP energies is now accessible with respect to

the as-deposited state.

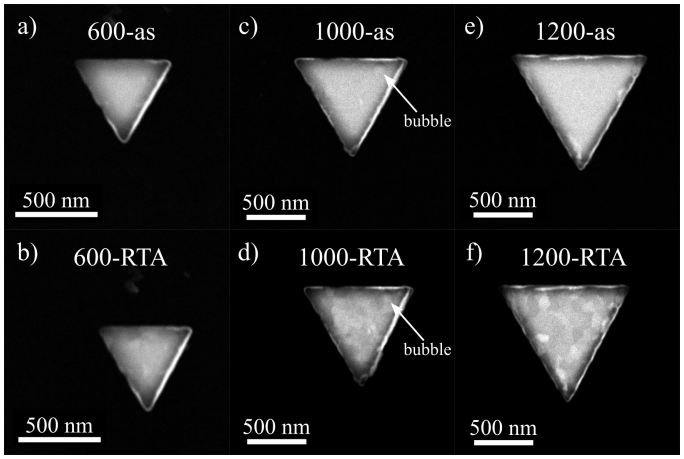

Figure 4.7: HAADF images of 71 nm thick ITO triangles of (a-b) 600 nm, (c-d) 1000 nm, and (e-f) 1200 nm side lengths. Figures b), d), and f) are annealed, with diffraction contrast revealing grain boundaries. Z-contrast along the edges arise from the fabrication.

Figure 4.7 displays three triangles of different lengths (600 nm, 1000 nm, and 1200 nm) before and after annealing. A bubble protrusion is shown in the Figures 4.7c and 4.7d, which seems to have survived the RTA, but its effect could not be quantified or even visualized. The grains of the annealed structures are visibly more defined as the side lengths increase, making it difficult to compare the average grain size between them relying only on the HAADF signal contrast. Figures 4.8 and 4.9 compare the resultant EELS spectra for these triangles.

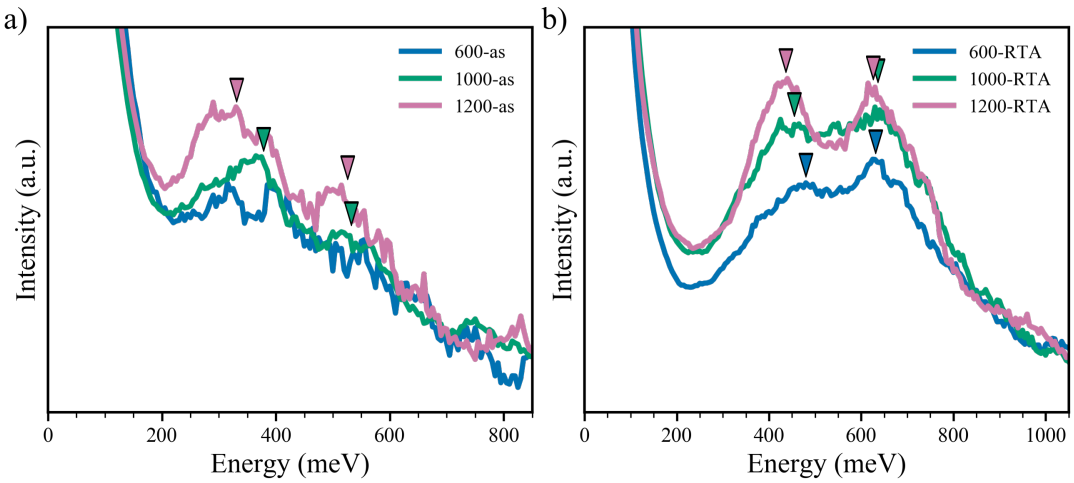

Figure 4.8: Comparison of EELS spectra over the triangle surface a) before (600-as, 1000-as, 1200-as) and b) after (600-RTA, 1000-RTA, 1200-RTA) annealing. First order cavity modes and bulk modes are highlighted after 10 RL iterations for each SI.

Each spectrum in Figure 4.8 was integrated over the structure surface, and therefore each suffers from additional scattering within the sample. As a result, the SNR is poor, and coupled with the peak broadening arising from plasmon damping (frequent collisions as γ increases) it is difficult to discern exactly the peak positions in Figure 4.8a. Through visual inspection, the cavity modes for structures 1000-as and 1200-as are approximated to occur at 367$\pm$39 meV and 330$\pm$39 meV, respectively. A value could not be estimated for 600-as. Peaks around 515$\pm$39 meV seem consistent and are hypothesized as the BP energy for the as-deposited ITO because the BP is a bulk property and independent of the surface geometry. The most prominent difference after annealing is seen in Figure 4.8b, where the peak intensity from the ZLP tail becomes much higher. The peak broadenening with decreasing triangle size may be attributed to an increased plasmon damping, or higher scattering rate, from the tapered boundaries. Additionally, the cavity modes are blue-shifted to 480$\pm$36 meV, 441$\pm$37 meV, and 435$\pm$37 meV for 600-as, 1000-as, and 1200-as, respectively. Even higher in energy are peaks clearly consistent at about 628$\pm$36 meV, which may be used to confirm a blue-shift of the BP from 515 meV. The changes in Figure 4.8 are consistent with the ellipsometry results that show an increase in N and decreases in γ and ε_∞. Interestingly, compared to the Themis results in Figure 4.5, E_c for 1200-RTA is lower by $\sim$102 meV. The two spectra come from two samples fabricated alongside each other, however, the RTA and acquisition of T8 (Figure 4.5) occurred $\sim$18 months prior to T6. Although the sample was mainly kept inside an evacuated desiccator, it is not unlikely for ambient oxygen to have reacted with the a-ITO nanostructure surface. E_c would then be reduced due to the compensated donor sites.

Whether or not grain boundary scattering (GBS) has any damping effect between the annealed structures is unclear since the lineshapes look relatively consistent. Figures 4.9a and 4.9b illustrate shifts in first order and second order LSP edge modes, respectively. They seem to have an agreeable trend with first order LSP resonances in ITO nanocrystals [104] that are photo-doped with UV light to increase the LSP energy from $\sim$750 meV to $\sim$850 meV. Similarly, the RTA promotes electrons in energy to participate in the free carrier resonance. The spectra illustrating this effect are integrated to the outsides of the triangle boundaries, and because they have a better SNR than Figure 4.8 it is much easier to compare peak characteristics. The first and second edge modes show a clear dependence on size, where the mode energy blue-shifts with decreasing dimension. Furthermore, by changing the dielectric environment, the modes are also blue-shifted after annealing. These two effects (geometry and RTA) are presented in Figure 4.10 along with the dispersion relations of annealed and unannealed films. A clear blue-shift is observed compared to the simulation (Figure 4.6b) due to the absence

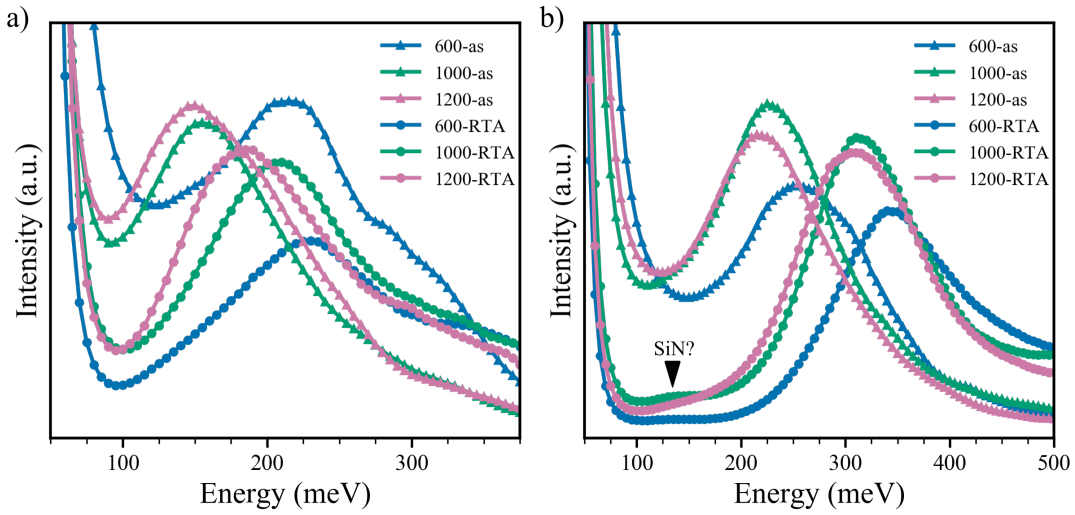

Figure 4.9: Comparison of spectra integrated beside the triangle a) corners and b) sides after annealing. 50 RL iterations for each. The small bump at ∼115 meV may correspond to a SiN phonon resonance.

of a substrate and surface oxidation. Each triangle should have a relation that approaches a different SP energy, due to the surface (geometry) being different. There are only two points for each geometry, which may not be enough to fit an accurate curve to, however, it still gives the idea that greater changes in LSP energy occur for higher order modes when annealing. For example, the change from 218 meV to 311 meV (difference of 93 meV) between the second modes of 1200-as and 1200-RTA is greater than between the first modes at 150 meV and 186 meV (difference of 36 meV).

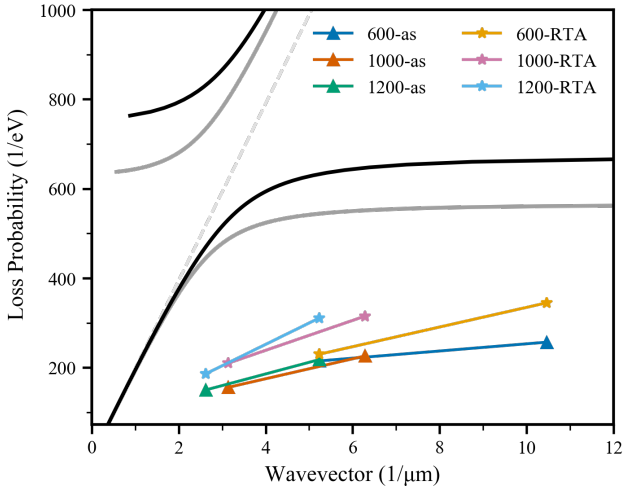

Figure 4.10: Experimental dispersion relations for 600 nm, 1000 nm, and 1200 nm long triangles (before and after annealing) compared to thin films from ellipsometry data and the light line.

A better dispersion may be obtained by using a larger structure to spread out the LSP modes in energy, as the dispersion becomes closer to that of a continuous film. However, the instrument, sample, and signal processing technique must be improved to get the dispersion relation for smaller structures. Proof of this is apparent between the Titan results of Figure 4.8 and Themis results of Figure 4.5. Figure 4.8 does not show the third edge mode that is visible with the Themis microscope, which has a ZLP FWHM about 40 meV smaller. The finding supports the necessity of pushing resolution capabilities to obtain a more complete picture of ITO's plasmonic response. This is especially true when exploring the microstructure and temperature effects on N, since the thickness and plasmon damping can severely degrade the signal, as observed with a-ITO.

4.2.3 Effect of Thickness

Naik et al. [24] report thickness-dependent optical properties of GZO thin films on heated glass substrates below ∼50 nm, where the carrier concentration N decreases and resistivity ρ increases as thickness t decreases. They attribute these effects to traps at the interface and increased GBS from higher densities of grain boundaries. They also extend this argument to ITO and other TCOs, which are reported elsewhere [98] [105] [68] to have similar thickness-dependent properties. To explore this relationship, observations in both low-loss and core-loss EELS regions are presented here.

Recall the study by Cleary et al. that proposes an electrically dead interfacial layer between ITO and its substrate (crystalline Si in their case). They find that N and μ decrease while R_s increases for thinner films. The crossing of $\mathrm{Re}\{\varepsilon(\omega)\}$ redshifts for thicknesses decreasing from 100 nm, and $\mathrm{Re}\{\varepsilon(\omega)\}$ becomes completely positive by thicknesses of ∼10 nm. Thus a different bulk peak should be expected for films of decreasing thickness as μ becomes more sensitive to the interfacial defects (i.e. greater rate of electron scattering). In terms of the lateral size dependence, no change should be expected when considering N, because the inactive volume fraction remains the same. R_s on the other hand, is potentially influenced if the lateral confinement varies the number or size of grains. Brewer et al. [105] derive a different equation for ω_p from that of Equation 2.8,

$$\omega_p = \sqrt{\frac{1}{R_s t \tau \varepsilon_0}}, \tag{4.1}$$

where R_s is the sheet resistance, τ is the average time between scattering events and t is the thickness. They use Equation 4.1 to explain the observed inverse dependence of ω_p

on R_s and τ of ITO thin films during near-IR reflectance measurements for constant t.

Visualizing the thickness effect was attempted with the MNPBEM toolbox. Since each t results in a unique $\varepsilon(\omega)$, more films of different t need to be analyzed for a wider model. A more accurate method might be to directly obtain $\varepsilon(\omega)$ from the experimental EELS spectra of a triangle using the Kramers-Kronig relations [88] [15]. If t is varied and $\varepsilon(\omega)$ is kept constant with that obtained from the 32 nm thick film, simulations of the 32 nm thick triangle have shown no observable change in the number of EEL peaks when compared with the 71 nm thick triangle of Figure 4.4. Additionally, proof of coupled surface modes in the form of extra peaks was unachievable even when performing a range of simulations for thicknesses between 10-200 nm. This was performed to back up the research by Rhodes et al. [98], who claim that when decreasing the thickness of ITO, SPR experiments witness the appearance of a surface-coupled resonance. A significant change was, however, observed in the relative peak intensities of the surface and bulk losses, which is presented here experimentally with Figures 4.8 and 4.11.

Low-loss spectra are given in Figure 4.11 for annealed 32 nm thick equilateral triangles of 1270 nm, 780 nm, 400 nm, and 200 nm lengths (1270-RTA, 780-RTA, 400-RTA, and 200-RTA, respectively). Each curve is the sum of spectra over each triangle surface to capture the bulk contribution. For 400-RTA, the peak at 285$\pm$42 meV is a second order edge mode excited with the beam over the center, similar to the simulation in Figure 4.4 at 354 meV. For triangles 1270-RTA, 780-RTA, and 400-RTA, the first order cavity modes are found at 383$\pm$42 meV, 459$\pm$42 meV, and 540$\pm$42 meV, respectively, and peaks at 751$\pm$42 meV, 865$\pm$42 meV, and 912$\pm$42 meV for each sample, respectively, may represent BP excitations. Excluding the indistinguishable peaks of 200-RTA, possibly due to a significantly non-uniform shape, an inverse relationship with the size of the triangle length is observed. The spectra are in contrast with the consistent 628 meV peak for the annealed 71 nm thick triangles (Figure 4.8). This may suggest that the microstructure and carrier transport dramatically changes between triangles, and that E_c is more sensitive to scattering centers with the reduced thickness. Further evidence that these peaks (at 751 meV, 865 meV, and 912 meV) come from the bulk include the intensity ratio between them and the cavity modes (at 383 meV, 459 meV, and 540 meV) compared to the ratio from the thicker triangles (Figure 4.11b). An additional red-shift of the surface cavity mode is seen for the thinner triangle. Decreasing the thickness reduced the BP intensity, which agrees with the proportionality with thickness t in Equation 2.34 and the surface effect reported by Raether [87] in Equation 2.36.

Inputting $\varepsilon(\omega)$ from ellipsometry into the bulk energy loss function gives a resonant condition at $\sim$724 meV, shown by the dotted black line in Figure 4.11. It seems

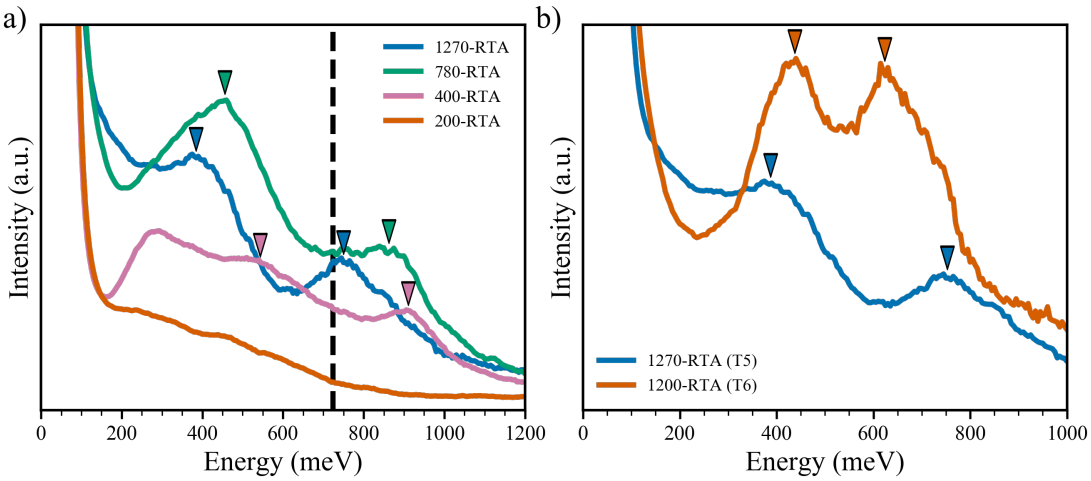

Figure 4.11: a) Triangles of 32 nm thickness and associated EELS spectra integrated over their entire surface area. The dotted black line represents the bulk loss function peak value for a continuous film. All spectra except for 780-RTA were acquired in the same session. b) Comparison of largest triangles in samples T5 and T6. The BP peak decreases and the surface cavity mode red-shifts with respect to the thicker triangle.

to follow the trend of decreasing E_p for increasing side length. 1270-RTA has a bulk resonance ($E_{c1270} = 751$ meV) approximately equal to the 730 meV bulk resonance of the thicker (1200 nm side length) triangle found with the Themis. However, the accuracy of such comparisons is unknown because these samples were fabricated separately. Uncontrolled variables include O_2 gas exposure from the spin coating, EBL, and deposition, as well as residual material in the chamber from previous depositions. Both of these could affect the position of the bulk resonance.

Recalling Figures 4.2c and 4.2f that unveil the interfacial regions between ITO and *a*-SiN, core-loss EELS maps were taken over these cross-sections to potentially observe whether this electrically inactive layer exists and whether it influences the shapes or intensities of oxygen, In, and Sn ionization edges. Spectra are given in Figures 4.12 and 4.13 for 32 nm and 71 nm thick ITO cross-sections, respectively. The energy range of interest is between 380-550 eV, where similar changes are observed around the oxygen K-edge at 532 eV and N K-edge at 401 eV between the two samples. The $M_{4,5}$-edges of In and Sn are located at 443 eV and 485 eV, respectively, therefore overlapping in energy with each other and the oxygen edge, making it difficult to distinguish In and Sn components. The Sn $N_{4,5}$-edge at 24 eV does not provide any contrasting information and the SNR at higher energies (In L_3-, L_4-edges around 3730 eV and 3938 eV, Sn L_3-, L_2-edges at 3929 eV, and 4156 eV, respectively) is too low to distinguish an edge shape. A spectrometer with a better sensitivity to low signals may have to be utilized to observe excitations at these energies.

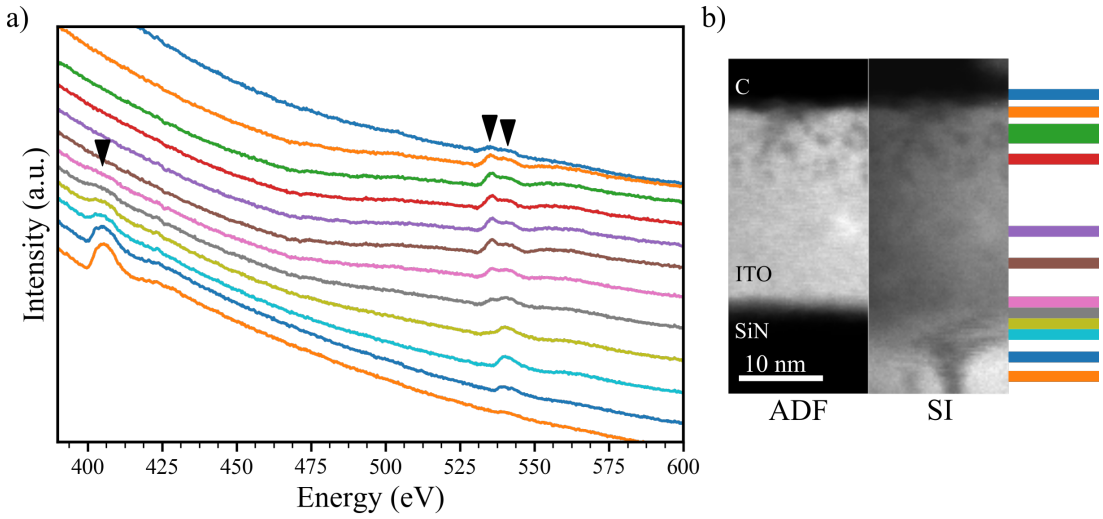

Figure 4.12: a) Core-loss EEL spectra for the carbon/ITO and ITO/SiN interfaces of the 32 nm thick triangle cross-section shown in the ADF image and integration areas of b). Spectra were acquired with ∼1 eV resolution. Little variation was observed over the bulk of the material.

Looking at the areas of integration from the substrate to film direction in Figure 4.12b and the resultant spectra in 4.12a, the N K-edge disappears completely past the interfacial area of reduced ADF intensity. In contrast, the oxygen K-edge seems to start gaining intensity within the substrate. This may occur if the incident beam is not entirely parallel to the interface, crossing both substrate and film. Therefore, it is difficult to specify where exactly the interface is. A small peak at 536±1 eV rises while moving up through the interfacial region as the N K-edge completely disappears. The edge present within the bulk (up from the brown curve) now appears similar to that observed by Morikawa et al. in Figure 2.26, consisting of a higher intensity peak at 536±1 eV, a lower peak at 540±1 eV. The Sn $M_{4,5}$-edge at 485 eV was indistinguishable over the signal noise and the intensities of In $M_{4,5}$- and oxygen K-edges. No variation (other than that attributed to noise) was observed throughout the film thickness, despite the appearance of bright and dark spots in the ADF and spectrum images, until the top surface where both peaks concurrently disappear (top, dark blue). An EDX map of this cross-section could be beneficial to correlate with these results, especially for the distribution of Sn throughout the thickness, granted a high enough SNR is achieved.

The changing oxygen K-edge over the ITO/SiN_x interfacial region may be attributed to a change in the unoccupied DOS that electrons from the 1s orbital are excited into. Interface defects that modify μ could vary the band structure and DOS in accordance with this edge shape. Following the findings by Morikawa et al. and Albrecht et al., any In metal precipitates or $V_O^{\bullet\bullet}$ clusters could cause changes to the oxygen and In peak

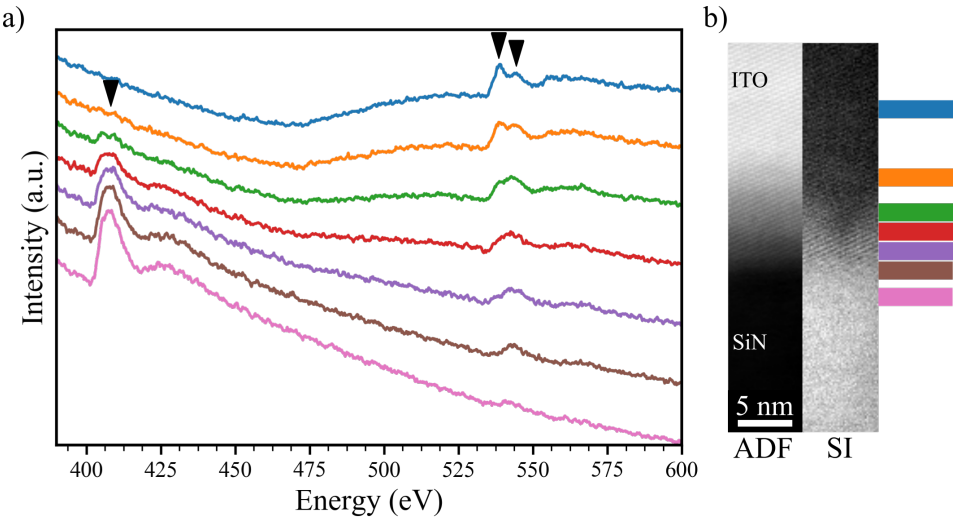

Figure 4.13: a) Core-loss EEL spectra for the ITO/SiN interface of the 71 nm thick triangle cross-section shown in the ADF image and integration areas of b).

intensities. It is surprising to find no discernible change in intensity over the dark and light spots, although their physical origin might constitute only a small fraction of the entire specimen thickness. When integrating over small areas in the SI, the spectra may need to be de-noised, such as with principal component analysis (PCA), to distinguish such changes.

Figure 4.13a displays core-loss spectra of the 71 nm thick triangle interface given in Figure 4.13b. Here, both the ADF and the SI show the periodic contrast (corresponding to lattice planes) observed in Figure 4.2c. Figure 4.2f may have a layer of *a*-ITO, thus the shape of the oxygen K-edge could be expected to be different than that of *c*-ITO. Recall that the Fermi level is lower for *a*-ITO than *c*-ITO due to Sn and $V_O^{\bullet\bullet}$ acting as deep energy traps. Qualitatively however, the core-loss spectra in Figure 4.13a illustrate the same trend across the interface as with the thinner structure (Figure 4.12a) that exhibits an area of *a*-ITO. Higher resolution EELS (i.e. using a monochromator) or X-ray photoelectron spectroscopy (XPS) may be required to reveal more detailed information, such as peak shifts of less than 1 eV. Post-processing to de-noise spectra should supplement these techniques. A thickness profile with Auger spectroscopy might also be sufficient to detail the elemental distribution throughout the film and closer to the interface.

Conclusions and Future Work

The fabrication of amorphous and crystalline ITO nanostructures was demonstrated on an amorphous SiN substrate by RF sputter deposition and a rapid thermal anneal. Variations in ITO's structure and electrical properties were observed for different triangle dimensions and post-annealing. TEM imaging and diffraction clearly illustrated that the as-deposited *a*-ITO crystallizes with the RTA, and that thinner structures resulted in larger grain sizes for the same RTA procedure. Compared to 71 nm thick ITO, 32 nm thick cross-sectional images exhibited intensity variations along the top half of the structure, which may be attributed to a clustering of oxygen vacancies and indium interstitials. Additionally, the interface with the substrate appears to contain a layer of *a*-ITO that is absent from the 71 nm thick cross-section. Both of these characteristics could be a consequence of the RTA, although a more systematic study over more film thicknesses and annealing times is required.

The combination of monochromated low-loss EELS and RL deconvolution successfully revealed LSP resonances down to $\sim$150 meV, well into the mid-IR wavelength range, as well as a bulk phonon resonance at $\sim$100 meV. Simulations using ellipsometry data used to derive the dielectric function confirmed the spectral regions of each LSP mode and bulk resonance in 71 nm thick triangles before and after annealing. The RTA caused a significant blue-shift in LSP and BP energies mainly by increasing the carrier concentration N and reducing the high-frequency dielectric constant ε_∞. Higher order LSP modes showed a greater blue-shift than lower orders, and higher energy resolutions are needed to make this more apparent in dispersion plots. Decreasing the triangle side length also blue-shifted the LSP peaks while the BP peak was consistently stable. A red-shift of $\sim$102 meV of the BP energy was, however, observed between triangles (1200 nm length, 71 nm height) from TEM grids fabricated together but had EELS performed on them months apart. This may be due to an oxide layer forming over a long period of time. Thus, the sensitivity of plasmon excitations in ITO to its environment and the fabrication process make it extremely flexible to engineer, opening the prospect for commercial plasmonic devices.

Low-loss EELS was also performed on $\sim$32 nm thick triangles, unveiling what is

believed to be a blue-shift of the BP peak with decreasing triangle side length. It is unclear what the origin of this relationship is, although it may be related to the clustered non-uniformities seen in the cross-sections. A significant change in either N or the mobility μ of free carriers at the interfaces (substrate, air, and grain) should be required to shift the BP energy. Core-loss EELS over the 32 nm thick cross-section was attempted to potentially relate a change in the In, Sn, or oxygen ionization edges to the parameters that control the BP. From the oxygen K-edge, the 536 eV peak was found to decrease as the probe moved from the ITO into the SiN substrate; however, this was also observed for the 71 nm thick cross-section and no other variations were present over different parts of the ITO structures. Density functional theory (DFT) calculations may be necessary to model how the DOS of bulk ITO can change closer to an interface.

In the low-loss region, $\varepsilon(\omega)$ could be extracted to pinpoint E_c and perform EEL simulations. A number of nanostructures of increasing size can then have their $\varepsilon(\omega)$ compared with each other, as well as those obtained from ellipsometry. Accuracy of the ellipsometry fits can be improved by modifying the model to include a surface roughness layer or an ITO layer that has a non-uniform $\varepsilon(\omega)$ throughout its thickness, which could be especially useful for the thinner ITO film. Although this increases the complexity of the fitting procedure, the resulting optical constants may be more reliable when comparing to those obtained by EELS. Additionally, using instruments (e.g. an IR-VASE ellipsometer) and dispersion models (e.g. Lorentz oscillator) that cover a larger wavelength range so that no extrapolation is necessary would help with the optimization.

The results presented in this thesis may inspire some further work to understand other characteristics of ITO in addition to its plasmonic behaviour. Its band gap is an example that, to date, has not yet been studied using EELS. An in-situ STEM-EELS heating experiment may be carried out to visualize the amorphous-to-crystalline transition along with the evolution (blue-shift and narrowing) of plasmon peaks. An interesting area to explore is the possibility of ITO plasmons coupling with the SiN bulk phonon to produce extra resonances. Due to their unique response at very low energies, engineering other TCOs to interact with insulators may be viable, effectively broadening the capabilities of these alternative plasmonic materials.

Appendix

A.3 Richardson-Lucy Deconvolution

In EELS, the signal A entering the spectrometer gets blurred by the spectrometer impulse response, or point spread function (PSF), H, and outputs the blurred signal B on the computer screen. Recall that each electron is converted into a photon, which is captured by the CCD. Assuming the ideal scenario where each observation made by a CCD pixel i is independent and corresponds to one event A_i, given that there are n possible events (n pixels) so that $P(A_1)+P(A_2)+...+P(A_n)=1$, where $P(A_i)$ is the probability of an event from signal A. If A is captured by pixel i, what is the probability of B at pixel j? This can be expressed as $P(B_j \mid A_i)$ (i.e. the PSF), and the total probability of B at pixel j becomes,

$$P\big(B_j\big) = \sum_i P\big(B_j \mid A_i\big) P\big(A_i\big). \tag{4.2}$$

The general form of Bayes' theorem is,

$$P\big(A_i \mid B_j\big) = \frac{P\big(B_j \mid A_i\big) P(A_i)}{P\big(B_j\big)} = \frac{P\big(A_i \cap B_j\big)}{P\big(B_j\big)}, \tag{4.3}$$

where $P\big(A_i \cap B_j\big)$ is the joint probability of both A and B being true. From [93], the total probability of A at pixel i may be expressed similarly to Equation 4.2 as,

$$P\big(A_i\big) = \sum_j P\big(A_i \mid B_j\big) P\big(B_j\big). \tag{4.4}$$

Substituting Equation 4.3 into Equation 4.4 gives,

$$P(A_i) = P(A_i)\sum_j \frac{P(B_j \mid A_i)P(B_j)}{P(B_j)} \tag{4.5}$$

$$= P(A_i)\sum_j \frac{P(B_j \mid A_i)P(B_j)}{\sum_k P(B_j|A_k)P(A_k)}, \tag{4.6}$$

which may be rewritten as an iterative procedure,

$$A_i^{(m+1)} = A_i^{(m)}\sum_j \frac{H_{ji}B_j}{\sum_k H_{jk}A_k^{(m)}}. \tag{4.7}$$

A.4 RTA Procedure

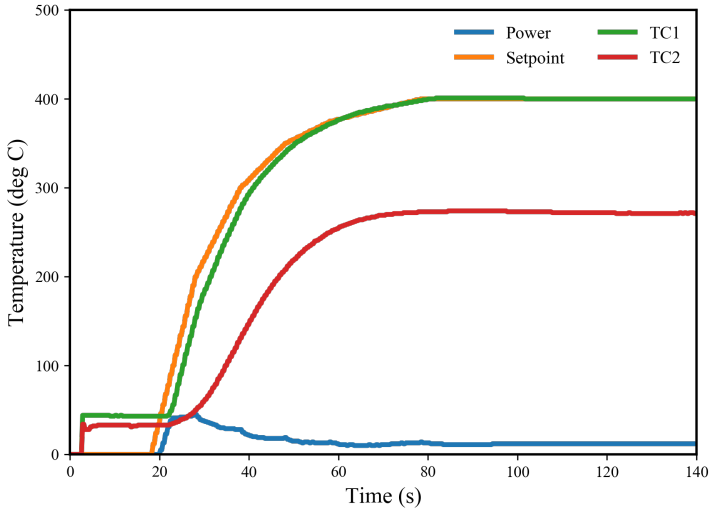

Figure 4.14: Temperature evolution of RTA chamber. The setpoint (orange) and power (blue) are set to different temperatures at certain times. The temperature is read by the thermocouples TC1 and TC2, where TC2 was known to underestimate at the time of annealing.

A.5 Additional Images

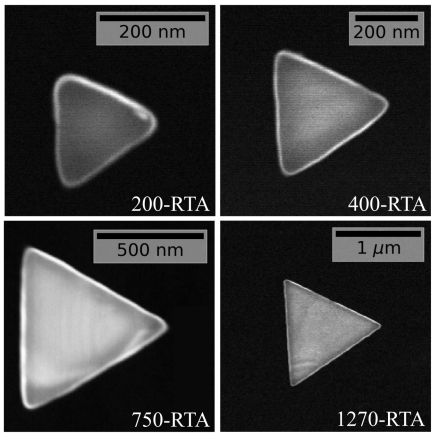

Figure 4.15: HAADF images of 32 nm thick triangles of 200 nm, 400 nm, 750 nm, and 1270 nm length that correspond to spectra in Figure 4.11a.

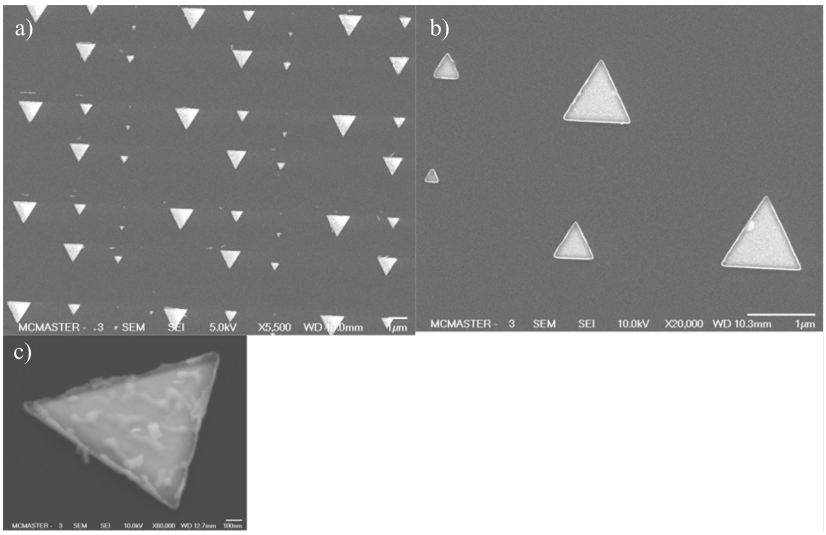

Figure 4.16: SEM images of (a-b) 32 nm thick and c) 71 nm thick fabricated triangles after annealing. Some thicker triangles showed lots of bubbles, the origin of which is unknown. It is also unclear how to avoid this effect.

A.6 X-Ray Diffraction of ITO Film

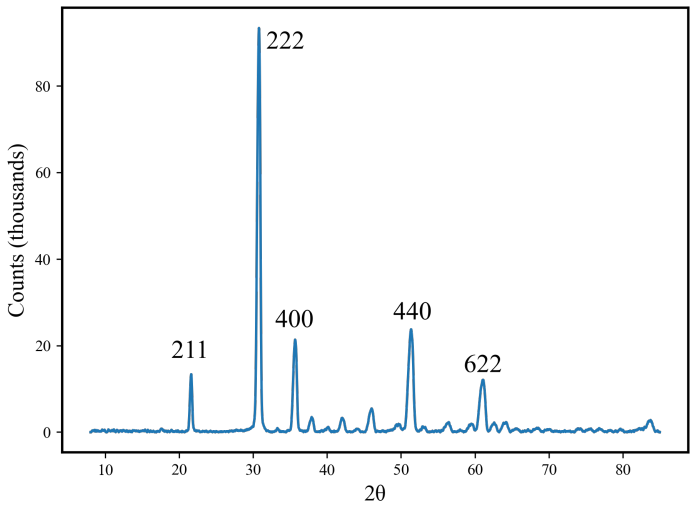

Figure 4.17: XRD of an annealed 71 nm thick film of $In_{1.958}Sn_{0.042}O_{3.021}$ using a CuKα source. Analysis finds a cubic lattice with constant 10.12Å of the 1a-3 (206) space group. Comparison in JEMS software[1] with ITO in powder form gives the same diffraction pattern.

[1] `http://www.jems-saas.ch/Home/jemsWebSite/jems.html`

Bibliography

[1] R. L Moss et al. *Critical Metals in Strategic Energy Technologies: Assessing Rare Metals as Supply-Chain Bottlenecks in Low-Carbon Energy Technologies.* English. OCLC: 903496534. Luxembourg: Publications Office, 2011. ISBN: 978-92-79-20698-6.

[2] D. S. Ginley, Hideo Hosono, and David C. Paine, eds. *Handbook of Transparent Conductors*. en. OCLC: ocn495781319. New York: Springer, 2010. ISBN: 978-1-4419-1637-2 978-1-4419-1638-9.

[3] C.G. Granqvist and A. Hultåker. "Transparent and Conducting ITO Films: New Developments and Applications". en. In: *Thin Solid Films* 411.1 (May 2002), pp. 1–5. DOI: 10.1016/S0040-6090(02)00163-3.

[4] G. Korotcenkov, V. Brinzari, and B. K. Cho. "In2O3 - and SnO2 - Based Thin Film Ozone Sensors: Fundamentals". en. In: *Journal of Sensors* 2016 (2016), pp. 1–31. DOI: 10.1155/2016/3816094.

[5] R. H. Ritchie. "Plasma Losses by Fast Electrons in Thin Films". en. In: *Physical Review* 106.5 (June 1957), pp. 874–881. DOI: 10.1103/PhysRev.106.874.

[6] David Bohm and David Pines. "A Collective Description of Electron Interactions: III. Coulomb Interactions in a Degenerate Electron Gas". en. In: *Physical Review* 92.3 (Nov. 1953), pp. 609–625. DOI: 10.1103/PhysRev.92.609.

[7] C. J. Powell and J. B. Swan. "Origin of the Characteristic Electron Energy Losses in Aluminum". en. In: *Physical Review* 115.4 (Aug. 1959), pp. 869–875. DOI: 10.1103/PhysRev.115.869.

[8] P.E. Batson. "Inelastic Scattering of Fast Electrons in Clusters of Small Spheres". en. In: *Surface Science* 156 (June 1985), pp. 720–734. DOI: 10.1016/0039-6028(85)90242-0.

[9] P. Dawson, F. de Fornel, and J-P. Goudonnet. "Imaging of Surface Plasmon Propagation and Edge Interaction Using a Photon Scanning Tunneling Microscope". en. In: *Physical Review Letters* 72.18 (May 1994), pp. 2927–2930. DOI: 10.1103/PhysRevLett.72.2927.

[10] Ian Freestone et al. "The Lycurgus Cup — A Roman Nanotechnology". en. In: *Gold Bulletin* 40.4 (Dec. 2007), pp. 270–277. DOI: 10.1007/BF03215599.

[11] V.J. Keast. "Ab Initio Calculations of Plasmons and Interband Transitions in the Low-Loss Electron Energy-Loss Spectrum". en. In: *Journal of Electron Spectroscopy and Related Phenomena* 143.2-3 (May 2005), pp. 97–104. DOI: 10.1016/j.elspec.2004.04.005.

[12] Charles Cherqui et al. "Characterizing Localized Surface Plasmons Using Electron Energy-Loss Spectroscopy". en. In: *Annual Review of Physical Chemistry* 67.1 (May 2016), pp. 331–357. DOI: 10.1146/annurev-physchem-040214-121612.

[13] Stefan A. Maier. *Plasmonics: Fundamentals and Applications*. New York: Springer, 2007. ISBN: 978-0-387-33150-8 978-0-387-37825-1.

[14] Shaista Babar and J. H. Weaver. "Optical Constants of Cu, Ag, and Au Revisited". en. In: *Applied Optics* 54.3 (Jan. 2015), p. 477. DOI: 10.1364/AO.54.000477.

[15] R. F. Egerton. *Electron Energy-Loss Spectroscopy in the Electron Microscope*. en. Third edition. The Language of Science. New York: Springer, 2011. ISBN: 978-1-4419-9582-7 978-1-4419-9583-4.

[16] Heinz Raether. *Surface Plasmons: On Smooth and Rough Surfaces and on Gratings*. Springer Tracts in Modern Physics 111. OCLC: 246680529. Berlin: Springer, 1988. ISBN: 978-3-540-17363-2 978-0-387-17363-4.

[17] E. N. Economou. "Surface Plasmons in Thin Films". en. In: *Physical Review* 182.2 (June 1969), pp. 539–554. DOI: 10.1103/PhysRev.182.539.

[18] J. J. Burke, G. I. Stegeman, and T. Tamir. "Surface-Polariton-like Waves Guided by Thin, Lossy Metal Films". en. In: *Physical Review B* 33.8 (Apr. 1986), pp. 5186–5201. DOI: 10.1103/PhysRevB.33.5186.

[19] Naomi J. Halas et al. "Plasmons in Strongly Coupled Metallic Nanostructures". en. In: *Chemical Reviews* 111.6 (June 2011), pp. 3913–3961. DOI: 10.1021/cr200061k.

[20] Gururaj V. Naik, Vladimir M. Shalaev, and Alexandra Boltasseva. "Alternative Plasmonic Materials: Beyond Gold and Silver". en. In: *Advanced Materials* 25.24 (June 2013), pp. 3264–3294. DOI: 10.1002/adma.201205076.

[21] Viktoriia E. Babicheva, Alexandra Boltasseva, and Andrei V. Lavrinenko. "Transparent Conducting Oxides for Electro-Optical Plasmonic Modulators". en. In: *Nanophotonics* 4.1 (Jan. 2015). DOI: 10.1515/nanoph-2015-0004.

[22] Jacob B. Khurgin and Alexandra Boltasseva. "Reflecting upon the Losses in Plasmonics and Metamaterials". en. In: *MRS Bulletin* 37.08 (Aug. 2012), pp. 768–779. DOI: 10.1557/mrs.2012.173.

[23] M. A. Noginov et al. "Demonstration of a Spaser-Based Nanolaser". en. In: *Nature* 460.7259 (Aug. 2009), pp. 1110–1112. DOI: 10.1038/nature08318.

[24] Gururaj V. Naik, Jongbum Kim, and Alexandra Boltasseva. "Oxides and Nitrides as Alternative Plasmonic Materials in the Optical Range [Invited]". en. In: *Optical Materials Express* 1.6 (Oct. 2011), p. 1090. DOI: 10.1364/OME.1.001090.

[25] Jean-Sebastien G. Bouillard et al. "Low-Temperature Plasmonics of Metallic Nanostructures". en. In: *Nano Letters* 12.3 (Mar. 2012), pp. 1561–1565. DOI: 10.1021/nl204420s.

[26] H.-D Liu et al. "Thickness Dependent Electrical Resistivity of Ultrathin (<40 Nm) Cu Films". en. In: *Thin Solid Films* 384.1 (Mar. 2001), pp. 151–156. DOI: 10.1016/S0040-6090(00)01818-6.

[27] G. Bemski. "Recombination Properties of Gold in Silicon". en. In: *Physical Review* 111.6 (Sept. 1958), pp. 1515–1518. DOI: 10.1103/PhysRev.111.1515.

[28] Ronald J. Gutmann et al. "Integration of Copper Multilevel Interconnects with Oxide and Polymer Interlevel Dielectrics". en. In: *Thin Solid Films* 270.1-2 (Dec. 1995), pp. 472–479. DOI: 10.1016/0040-6090(96)80080-0.

[29] P.R. West et al. "Searching for Better Plasmonic Materials". en. In: *Laser & Photonics Reviews* 4.6 (Nov. 2010), pp. 795–808. DOI: 10.1002/lpor.200900055.

[30] Qiushi Guo et al. "Infrared Nanophotonics Based on Graphene Plasmonics". en. In: *ACS Photonics* 4.12 (Dec. 2017), pp. 2989–2999. DOI: 10.1021/acsphotonics.7b00547.

[31] A. Boltasseva and H. A. Atwater. "Low-Loss Plasmonic Metamaterials". en. In: *Science* 331.6015 (Jan. 2011), pp. 290–291. DOI: 10.1126/science.1198258.

[32] Shi Qiang Li et al. “Infrared Plasmonics with Indium–Tin-Oxide Nanorod Arrays”. en. In: *ACS Nano* 5.11 (Nov. 2011), pp. 9161–9170. DOI: 10.1021/nn203406f.

[33] Peijun Guo et al. “Ultrafast Switching of Tunable Infrared Plasmons in Indium Tin Oxide Nanorod Arrays with Large Absolute Amplitude”. en. In: *Nature Photonics* 10.4 (Apr. 2016), pp. 267–273. DOI: 10.1038/nphoton.2016.14.

[34] Ting Wang and Pavle V. Radovanovic. “Free Electron Concentration in Colloidal Indium Tin Oxide Nanocrystals Determined by Their Size and Structure”. en. In: *The Journal of Physical Chemistry C* 115.2 (Jan. 2011), pp. 406–413. DOI: 10.1021/jp108926a.

[35] Robert W. Johns et al. “Direct Observation of Narrow Mid-Infrared Plasmon Linewidths of Single Metal Oxide Nanocrystals”. en. In: *Nature Communications* 7 (May 2016), p. 11583. DOI: 10.1038/ncomms11583.

[36] Misun Kang et al. “Near-Infrared Optical Extinction of Indium Tin Oxide Structures Prepared by Nanosphere Lithography”. en. In: *ACS Photonics* 3.10 (Oct. 2016), pp. 1993–1999. DOI: 10.1021/acsphotonics.6b00649.

[37] Guozhong Cao. *Nanostructures & Nanomaterials: Synthesis, Properties & Applications*. OCLC: ocn212610774. London ; Hackensack, NJ: Imperial College Press, 2004. ISBN: 978-1-86094-415-4 978-1-86094-480-2.

[38] D. Bruce Buchholz et al. “The Structure and Properties of Amorphous Indium Oxide”. en. In: *Chemistry of Materials* 26.18 (Sept. 2014), pp. 5401–5411. DOI: 10.1021/cm502689x.

[39] Daniel R. Hagleitner et al. “Bulk and Surface Characterization of In 2 O 3 (001) Single Crystals”. en. In: *Physical Review B* 85.11 (Mar. 2012). DOI: 10.1103/PhysRevB.85.115441.

[40] Erie H Morales et al. “Surface Structure of Sn-Doped In $_2$ O $_3$ (111) Thin Films by STM”. In: *New Journal of Physics* 10.12 (Dec. 2008), p. 125030. DOI: 10.1088/1367-2630/10/12/125030.

[41] Aron Walsh and C. Richard A. Catlow. “Structure, Stability and Work Functions of the Low Index Surfaces of Pure Indium Oxide and Sn-Doped Indium Oxide (ITO) from Density Functional Theory”. en. In: *Journal of Materials Chemistry* 20.46 (2010), p. 10438. DOI: 10.1039/c0jm01816c.

[42] Seung-Ik Jun et al. “A Statistical Parameter Study of Indium Tin Oxide Thin Films Deposited by Radio-Frequency Sputtering”. en. In: *Thin Solid Films* 476.1 (Apr. 2005), pp. 59–64. DOI: 10.1016/j.tsf.2004.09.011.

[43] Masayuki Kamei, Yuzo Shigesato, and Satoru Takaki. "Origin of Characteristic Grain-Subgrain Structure of Tin-Doped Indium Oxide Films". en. In: *Thin Solid Films* 259.1 (Apr. 1995), pp. 38–45. DOI: 10.1016/0040-6090(94)06390-7.

[44] Koichi Nakajima and Noriaki Sato. "Method of Manufacturing Ito Sputtering Target". Pat. US5094787A (Japan Energy Corp, Nippon Mining Co Ltd).

[45] F. Kurdesau et al. "Comparative Study of ITO Layers Deposited by DC and RF Magnetron Sputtering at Room Temperature". en. In: *Journal of Non-Crystalline Solids* 352.9-20 (June 2006), pp. 1466–1470. DOI: 10.1016/j.jnoncrysol.2005.11.088.

[46] X. W. Sun, H. C. Huang, and H. S. Kwok. "On the Initial Growth of Indium Tin Oxide on Glass". en. In: *Applied Physics Letters* 68.19 (May 1996), pp. 2663–2665. DOI: 10.1063/1.116274.

[47] Cleva W. Ow-Yang et al. "A Time-Resolved Reflectivity Study of the Amorphous-to-Crystalline Transformation Kinetics in Dc-Magnetron Sputtered Indium Tin Oxide". en. In: *Journal of Applied Physics* 83.1 (Jan. 1998), pp. 145–154. DOI: 10.1063/1.366731.

[48] David C. Paine et al. "A Study of Low Temperature Crystallization of Amorphous Thin Film Indium–Tin–Oxide". en. In: *Journal of Applied Physics* 85.12 (June 1999), pp. 8445–8450. DOI: 10.1063/1.370695.

[49] A.K Kulkarni et al. "Electrical, Optical and Structural Characteristics of Indium-Tin-Oxide Thin Films Deposited on Glass and Polymer Substrates". en. In: *Thin Solid Films* 308-309 (Oct. 1997), pp. 1–7. DOI: 10.1016/S0040-6090(97)00526-9.

[50] N. M. Khusayfan and M. M. El-Nahass. "Study of Structure and Electro-Optical Characteristics of Indium Tin Oxide Thin Films". en. In: *Advances in Condensed Matter Physics* 2013 (2013), pp. 1–8. DOI: 10.1155/2013/408182.

[51] A. De, P.K. Biswas, and J. Manara. "Study of Annealing Time on Sol–Gel Indium Tin Oxide Films on Glass". en. In: *Materials Characterization* 58.7 (July 2007), pp. 629–636. DOI: 10.1016/j.matchar.2006.07.011.

[52] L Kerkache et al. "Physical Properties of RF Sputtered ITO Thin Films and Annealing Effect". en. In: *Journal of Physics D: Applied Physics* 39.1 (Jan. 2006), pp. 184–189. DOI: 10.1088/0022-3727/39/1/027.

[53] T.C Gorjanc et al. "Room Temperature Deposition of ITO Using r.f. Magnetron Sputtering". en. In: *Thin Solid Films* 413.1-2 (June 2002), pp. 181–185. DOI: 10.1016/S0040-6090(02)00425-X.

[54] S. Muranaka, Y. Bando, and T. Takada. “Influence of Substrate Temperature and Film Thickness on the Structure of Reactively Evaporated In2O3 Films”. en. In: *Thin Solid Films* 151.3 (Aug. 1987), pp. 355–364. DOI: 10.1016/0040-6090(87)90134-9.

[55] G. Frank and H. Kostlin. “Electrical Properties and Defect Model of Tin-Doped Indium Oxide Layers”. en. In: *Applied Physics A Solids and Surfaces* 27.4 (Apr. 1982), pp. 197–206. DOI: 10.1007/BF00619080.

[56] Sebastien D. Lounis et al. “Defect Chemistry and Plasmon Physics of Colloidal Metal Oxide Nanocrystals”. en. In: *The Journal of Physical Chemistry Letters* 5.9 (May 2014), pp. 1564–1574. DOI: 10.1021/jz500440e.

[57] S. Lany et al. “Surface Origin of High Conductivities in Undoped In 2 O 3 Thin Films”. en. In: *Physical Review Letters* 108.1 (Jan. 2012). DOI: 10.1103/PhysRevLett.108.016802.

[58] Oliver Bierwagen. “Indium Oxide—a Transparent, Wide-Band Gap Semiconductor for (Opto)Electronic Applications”. en. In: *Semiconductor Science and Technology* 30.2 (Feb. 2015), p. 024001. DOI: 10.1088/0268-1242/30/2/024001.

[59] Furong Zhu et al. “Investigation of Annealing Effects on Indium Tin Oxide Thin Films by Electron Energy Loss Spectroscopy”. en. In: *Thin Solid Films* (2000), p. 7.

[60] M. Albrecht et al. “Coloration and Oxygen Vacancies in Wide Band Gap Oxide Semiconductors: Absorption at Metallic Nanoparticles Induced by Vacancy Clustering—A Case Study on Indium Oxide”. en. In: *Journal of Applied Physics* 115.5 (Feb. 2014), p. 053504. DOI: 10.1063/1.4863211.

[61] Sukit Limpijumnong et al. “Hydrogen Doping in Indium Oxide: An *Ab Initio* Study”. en. In: *Physical Review B* 80.19 (Nov. 2009). DOI: 10.1103/PhysRevB.80.193202.

[62] Ocal Tuna et al. “High Quality ITO Thin Films Grown by Dc and RF Sputtering without Oxygen”. en. In: *Journal of Physics D: Applied Physics* 43.5 (Feb. 2010), p. 055402. DOI: 10.1088/0022-3727/43/5/055402.

[63] J R Bellingham, W A Phillips, and C J Adkins. “Electrical and Optical Properties of Amorphous Indium Oxide”. en. In: *Journal of Physics: Condensed Matter* 2.28 (July 1990), pp. 6207–6221. DOI: 10.1088/0953-8984/2/28/011.

[64] Naoomi Yamada et al. “Donor Compensation and Carrier-Transport Mechanisms in Tin-Doped In $_2$ O $_3$ Films Studied by Means of Conversion Electron ^{119} Sn Mössbauer Spectroscopy and Hall Effect Measurements”. en. In: *Japanese Journal of Applied Physics* 39.Part 1, No. 7A (July 2000), pp. 4158–4163. DOI: 10.1143/JJAP.39.4158.

[65] H. Kim et al. “Effect of Film Thickness on the Properties of Indium Tin Oxide Thin Films”. en. In: *Journal of Applied Physics* 88.10 (Nov. 2000), pp. 6021–6025. DOI: 10.1063/1.1318368.

[66] Yuzo Shigesato and David C. Paine. “Study of the Effect of Sn Doping on the Electronic Transport Properties of Thin Film Indium Oxide”. en. In: *Applied Physics Letters* 62.11 (Mar. 1993), pp. 1268–1270. DOI: 10.1063/1.108703.

[67] Ho-Chul Lee and O Ok Park. “Electron Scattering Mechanisms in Indium-Tin-Oxide Thin Films: Grain Boundary and Ionized Impurity Scattering”. en. In: *Vacuum* 75.3 (July 2004), pp. 275–282. DOI: 10.1016/j.vacuum.2004.03.008.

[68] Justin W. Cleary et al. “Optical and Electrical Properties of Ultra-Thin Indium Tin Oxide Nanofilms on Silicon for Infrared Photonics”. en. In: *Optical Materials Express* 8.5 (May 2018), p. 1231. DOI: 10.1364/OME.8.001231.

[69] Ho-Chul Lee et al. “The Growth of Indium-Tin-Oxide Thin Films on Glass Substrates Using DC Reactive Magnetron Sputtering”. en. In: *Vacuum* 72.3 (Nov. 2003), pp. 269–276. DOI: 10.1016/j.vacuum.2003.08.001.

[70] I. Hamberg and C. G. Granqvist. “Evaporated Sn-doped In2O3 Films: Basic Optical Properties and Applications to Energy-efficient Windows”. en. In: *Journal of Applied Physics* 60.11 (Dec. 1986), R123–R160. DOI: 10.1063/1.337534.

[71] S. Zh. Karazhanov et al. “Phase Stability, Electronic Structure, and Optical Properties of Indium Oxide Polytypes”. en. In: *Physical Review B* 76.7 (Aug. 2007). DOI: 10.1103/PhysRevB.76.075129.

[72] O. Mryasov and A. Freeman. “Electronic Band Structure of Indium Tin Oxide and Criteria for Transparent Conducting Behavior”. en. In: *Physical Review B* 64.23 (Dec. 2001). DOI: 10.1103/PhysRevB.64.233111.

[73] R. L. Weiher and R. P. Ley. “Optical Properties of Indium Oxide”. en. In: *Journal of Applied Physics* 37.1 (Jan. 1966), pp. 299–302. DOI: 10.1063/1.1707830.

[74] A Raymond, J L Robert, and C Bernard. "The Electron Effective Mass in Heavily Doped GaAs". In: *Journal of Physics C: Solid State Physics* 12.12 (June 1979), pp. 2289–2293. DOI: 10.1088/0022-3719/12/12/014.

[75] Takumi Tomita et al. "The Origin of N-Type Conductivity in Undoped In2O3". en. In: *Applied Physics Letters* 87.5 (Aug. 2005), p. 051911. DOI: 10.1063/1.2001741.

[76] F. Fuchs and F. Bechstedt. "Indium-Oxide Polymorphs from First Principles: Quasiparticle Electronic States". en. In: *Physical Review B* 77.15 (Apr. 2008). DOI: 10.1103/PhysRevB.77.155107.

[77] P. D. C. King et al. "Surface Electron Accumulation and the Charge Neutrality Level in In 2 O 3". en. In: *Physical Review Letters* 101.11 (Sept. 2008). DOI: 10.1103/PhysRevLett.101.116808.

[78] David B. Williams and C. Barry Carter. *Transmission Electron Microscopy*. en. Boston, MA: Springer US, 2009. ISBN: 978-0-387-76500-6 978-0-387-76501-3. DOI: 10.1007/978-0-387-76501-3.

[79] Mathieu Kociak and Odile Stéphan. "Mapping Plasmons at the Nanometer Scale in an Electron Microscope". en. In: *Chemical Society Reviews* 43.11 (2014), p. 3865. DOI: 10.1039/c3cs60478k.

[80] P. E. Batson and J. Silcox. "Experimental Energy-Loss Function, Im [- 1 ε (q , ω)] , for Aluminum". en. In: *Physical Review B* 27.9 (May 1983), pp. 5224–5239. DOI: 10.1103/PhysRevB.27.5224.

[81] Jaysen Nelayah et al. "Mapping Surface Plasmons on a Single Metallic Nanoparticle". en. In: *Nature Physics* 3.5 (May 2007), pp. 348–353. DOI: 10.1038/nphys575.

[82] J. Nelayah et al. "Two-Dimensional Quasistatic Stationary Short Range Surface Plasmons in Flat Nanoprisms". en. In: *Nano Letters* 10.3 (Mar. 2010), pp. 902–907. DOI: 10.1021/nl903653x.

[83] Michel Bosman et al. "Mapping Surface Plasmons at the Nanometre Scale with an Electron Beam". In: *Nanotechnology* 18.16 (Apr. 2007), p. 165505. DOI: 10.1088/0957-4484/18/16/165505.

[84] D. Rossouw et al. "Multipolar Plasmonic Resonances in Silver Nanowire Antennas Imaged with a Subnanometer Electron Probe". en. In: *Nano Letters* 11.4 (Apr. 2011), pp. 1499–1504. DOI: 10.1021/nl200634w.

[85] Toon Coenen et al. “Directional Emission from Plasmonic Yagi–Uda Antennas Probed by Angle-Resolved Cathodoluminescence Spectroscopy”. en. In: *Nano Letters* 11.9 (Sept. 2011), pp. 3779–3784. DOI: 10.1021/nl201839g.

[86] F. J. García de Abajo. “Optical Excitations in Electron Microscopy”. en. In: *Reviews of Modern Physics* 82.1 (Feb. 2010), pp. 209–275. DOI: 10.1103/RevModPhys.82.209.

[87] H. Raether. “Surface Plasma Oscillations as a Tool for Surface Examinations”. en. In: *Surface Science* 8.1-2 (July 1967), pp. 233–246. DOI: 10.1016/0039-6028(67)90085-4.

[88] G. Höhler, ed. *Springer Tracts in Modern Physics, Volume 54*. Vol. 54. Springer Tracts in Modern Physics. Berlin, Heidelberg: Springer Berlin Heidelberg, 1970. ISBN: 978-3-540-05017-9 978-3-540-36325-5. DOI: 10.1007/BFb0045978.

[89] Ulrich Hohenester and Andreas Trügler. “MNPBEM – A Matlab Toolbox for the Simulation of Plasmonic Nanoparticles”. en. In: *Computer Physics Communications* 183.2 (Feb. 2012), pp. 370–381. DOI: 10.1016/j.cpc.2011.09.009.

[90] H. Morikawa, H. Kurata, and M. Fujita. “On the Grain Boundary Segregation of Sn in Indium-Tin-Oxide Thin Films”. en. In: *Journal of Electron Microscopy* 49.1 (Jan. 2000), pp. 67–72. DOI: 10.1093/oxfordjournals.jmicro.a023794.

[91] T.J. Kennett et al. “Bayesian Deconvolution III: Applications and Algorithm Implementation”. en. In: *Nuclear Instruments and Methods* 153.1 (July 1978), pp. 125–135. DOI: 10.1016/0029-554X(78)90628-6.

[92] Edson P. Bellido, David Rossouw, and Gianluigi A. Botton. “Toward 10 meV Electron Energy-Loss Spectroscopy Resolution for Plasmonics”. en. In: *Microscopy and Microanalysis* 20.03 (June 2014), pp. 767–778. DOI: 10.1017/S1431927614000609.

[93] William Hadley Richardson. “Bayesian-Based Iterative Method of Image Restoration*”. en. In: *Journal of the Optical Society of America* 62.1 (Jan. 1972), p. 55. DOI: 10.1364/JOSA.62.000055.

[94] Isobel Bicket. *SpectrumImagingAnalysisPy*. icbicket/DataAnalysis, 2017.

[95] P. F. Robusto and R. Braunstein. “Optical Measurements of the Surface Plasmon of Indium-Tin Oxide”. en. In: *physica status solidi (a)* 119.1 (May 1990), pp. 155–168. DOI: 10.1002/pssa.2211190118.

[96] A. Solieman and M.A. Aegerter. “Modeling of Optical and Electrical Properties of In2O3:Sn Coatings Made by Various Techniques”. en. In: *Thin Solid Films* 502.1-2 (Apr. 2006), pp. 205–211. DOI: 10.1016/j.tsf.2005.07.277.

[97] Scott H Brewer and Stefan Franzen. “Calculation of the Electronic and Optical Properties of Indium Tin Oxide by Density Functional Theory”. en. In: *Chemical Physics* 300.1-3 (May 2004), pp. 285–293. DOI: 10.1016/j.chemphys.2003.11.039.

[98] C. Rhodes et al. “Dependence of Plasmon Polaritons on the Thickness of Indium Tin Oxide Thin Films”. en. In: *Journal of Applied Physics* 103.9 (May 2008), p. 093108. DOI: 10.1063/1.2908862.

[99] Alfredo Campos et al. “Plasmonic Breathing and Edge Modes in Aluminum Nanotriangles”. en. In: *ACS Photonics* 4.5 (May 2017), pp. 1257–1263. DOI: 10.1021/acsphotonics.7b00204.

[100] V. J. Keast et al. “Higher Order Plasmonic Modes Excited in Ag Triangular Nanoplates by an Electron Beam”. en. In: *Plasmonics* 11.4 (Aug. 2016), pp. 1081–1086. DOI: 10.1007/s11468-015-0145-6.

[101] N. Wada et al. “Raman and IR Absorption Spectroscopic Studies on α, β, and Amorphous Si3N4”. en. In: *Journal of Non-Crystalline Solids* 43.1 (Jan. 1981), pp. 7–15. DOI: 10.1016/0022-3093(81)90169-1.

[102] Simon Ferré et al. “Comparative Study of SiO_2, Si_3N_4 and TiO_2 Thin Films as Passivation Layers for Quantum Cascade Lasers”. en. In: *Optics Express* 24.21 (Oct. 2016), p. 24032. DOI: 10.1364/OE.24.024032.

[103] Edson P. Bellido et al. “Plasmonic Coupling of Multipolar Edge Modes and the Formation of Gap Modes”. en. In: *ACS Photonics* 4.6 (June 2017), pp. 1558–1565. DOI: 10.1021/acsphotonics.7b00348.

[104] Alina M. Schimpf et al. “Redox Chemistries and Plasmon Energies of Photodoped In $_2$ O $_3$ and Sn-Doped In $_2$ O $_3$ (ITO) Nanocrystals”. en. In: *Journal of the American Chemical Society* 137.1 (Jan. 2015), pp. 518–524. DOI: 10.1021/ja5116953.

[105] Scott H. Brewer and Stefan Franzen. “Optical Properties of Indium Tin Oxide and Fluorine-Doped Tin Oxide Surfaces: Correlation of Reflectivity, Skin Depth, and Plasmon Frequency with Conductivity”. en. In: *Journal of Alloys and Compounds* 338.1-2 (May 2002), pp. 73–79. DOI: 10.1016/S0925-8388(02)00217-7.